

EXPERIMENTAL STUDIES OF LIRB: SPECTROSCOPY AND ULTRACOLD
MOLECULE FORMATION BY PHOTOASSOCIATION

A Dissertation

Submitted to the Faculty

of

Purdue University

by

Sourav Dutta

In Partial Fulfillment of the

Requirements for the Degree

of

Doctor of Philosophy

December 2013

Purdue University

West Lafayette, Indiana

To

Maa, Baba, Bunu, and Ishita

ACKNOWLEDGEMENTS

First, I would like to thank my advisor Prof. Yong P. Chen for his continued support and enthusiasm. I joined Purdue as a graduate student in 2007, the same year in which Yong joined as an assistant professor. I went to meet Yong and he said that he would work on condensed matter as well as atomic physics. I thought that this was interesting although at that time I had no idea of what an incredible feat this would be (now I do!). Although I had no prior experience with atomic physics, he encouraged me to work in the atomic physics part of the lab. I have learned the most during the first few years of my graduate school and I thank Yong for his patience during that time. I have been involved in many small projects which are not a part of my thesis and I thank him for those opportunities. Yong has an amazing capability of setting aside the details and looking at the underlying physics while still being rigorous, something that has led to many interesting and fruitful discussions. I hope to have imbibed some of that. I also thank him for allowing and encouraging independent student-driven research; chapter 5 of my thesis is mainly a result of that. I immensely appreciate the freedom that I had during my thesis research. I am also grateful for his suggestions on my papers and presentations and for always treating me as an equal. I will treasure the relationship with Yong in all the years to come.

I am fortunate to have worked on a project which involved collaborating closely with Prof. Daniel S. Elliott who is also my co-advisor. My thesis research was carried out in

Dan's lab where the apparatus is physically located. Dan has always been patient, available and supportive. He has an infinite bank of technical knowledge on lasers and electronics which has helped our experiment immensely. I have benefitted a lot from our discussions on molecular spectroscopy and light-matter interaction. I am also thankful for the opportunity to design the vacuum chamber for the parity violation experiment in atomic Cesium. I also thank Dan for carefully reading all my papers and for his feedback on my papers and thesis.

I thank Prof. David D. Nolte and Prof. Sabre Kais for taking the time to serve on my graduate committee. I would also like to thank Dr. Jesús Pérez-Ríos, Prof. Chris H. Greene, Prof. Olivier Dulieu, Prof. Paul S. Julienne, Prof. William C. Stwalley, Prof. Robin Côté, Dr. Marko Gacesa, Dr. Michael Bellos and Dr. Xuan Li for their interest in our work and for helpful discussions.

I have benefitted a great deal from Adeel Altaf and John Lorenz, the two other graduate students working on the LiRb project. John wrote most of the labview codes and Adeel set up many of the optics used in the experiment. Without their contribution, the experiment would not be in the state it is today. More importantly, I thank them for tolerating me and for always being helpful and cooperative. I also thank Dionysios Antypas who worked on the parity violation experiment next door. We have discussed many physics and non-physics problems and, thanks to our common interest in making better lasers, we developed a simple recipe for making stable external cavity diode lasers using off-the-shelf components.

I would like to thank Abraham Olson and Robert Niffenegger of the BEC lab for discussions and for their help with the BEC machine for some experiments not included

in this thesis. I learned a great deal from the discussions in the BEC subgroup meetings. I also thank the new members of the BEC lab, Chuan-Hsun Li and David Blasing, for the enthusiasm they bring. I would also like to thank folks in the nano-lab, particularly Luis Jauregui, Nirajan Mandal, Helin Cao, Jack Chung, Tai-Lung Wu, Jiuning Hu and Jifa Tian. Discussions with them kept my interest in nanoscience and condensed matter physics alive. Long chats with Luis and Suprem about many different things were a great way to refresh and reset the mind. I have spent a lot of time with the mill and the lathe in the machine shop. I thank James Corwin of the Physics machine shop for training me on the machines. I would also like to thank Sandy Formica for her help and support, and for the m&m's.

I take this opportunity to thank my teachers in school and college. Mrs. Basundhara Mukherjee, my Bengali-teacher at school, taught me to look beyond grades and to be aware of one's milieu. During my B.Sc. at Presidency College, I thoroughly enjoyed physical optics and quantum physics taught by Prof. Dipanjan Rai Chaudhuri and statistical physics by Prof. Debopriyo Shyam. This is where I first learned to plan and execute experiments, and decided to pursue physics further. During my M.Sc. at S. N. Bose National Centre for Basic Sciences, I was fortunate to have teachers and mentors like Prof. Jayanta K. Bhattacharjee and Prof. Binayak Dutta-Roy. They made physics look really easy. I thank all my teachers for their contributions.

Lastly, I thank my family for their support, encouragement and love. My parents encouraged me to pursue a career in science in a society where the most sought-after career options are engineering and medicine. I thank them for their encouragement and for their trust in me. The long distance phone conversations with my mother kept me

rooted and close to home over all these years. I thank my sister for being so proud of me. Finally, I would like to thank Ishita for her love and for the joy she brings to my life. I could not have found a more wonderful person to share my life with. Words cannot describe the contributions of these people and it is to them that this thesis is dedicated.

TABLE OF CONTENTS

	Page
LIST OF TABLES	ix
LIST OF FIGURES	xii
ABSTRACT	xxi
CHAPTER 1. INTRODUCTION	1
1.1 The rising interest in cold molecules	1
1.2 Creating ultracold molecules from ultracold atoms.....	3
1.3 Quantum computing with ultracold polar molecules.....	7
CHAPTER 2. SPECTROSCOPY OF HOT LIRB MOLECULES.....	13
2.1 Spectroscopy of LiRb in a heat-pipe oven.....	14
2.2 Analysis of molecular spectra.....	16
2.3 Molecular constants of $^7\text{Li}^{85}\text{Rb}$	19
2.4 Perturbations in the molecular spectra.....	24
2.5 Implications and predictions.....	26
2.6 Work in progress.....	27
CHAPTER 3. THE APPARATUS FOR PRODUCING COLD MOLECULES	28
3.1 Light sources for the MOT	29
3.2 The vacuum chamber.....	32
3.3 Two-species magneto-optical trap	39
3.4 Measurement and analysis of collision induced losses.....	40
3.5 Reduction of collision induced losses in a dark Rb MOT	52
3.6 Alternate method for the measurements of collision induced losses.....	53
CHAPTER 4. PHOTOASSOCIATION OF LIRB MOLECULES	55
4.1 Experimental setup	55

	Page
4.2 Molecular potentials	57
4.3 Photoassociation below the Li ($2s^2S_{1/2}$) + Rb ($5p^2P_{1/2}$) asymptote.....	59
4.3.1 Assignment of spectra below the Li ($2s^2S_{1/2}$) + Rb ($5p^2P_{1/2}$) asymptote	61
4.3.2 C_6 coefficients for the Li ($2s^2S_{1/2}$) + Rb ($5p^2P_{1/2}$) asymptote	63
4.4 Photoassociation below the Li ($2s^2S_{1/2}$) + Rb ($5p^2P_{3/2}$) asymptote.....	65
4.4.1 Assignment of spectra below the Li ($2s^2S_{1/2}$) + Rb ($5p^2P_{3/2}$) asymptote	66
4.4.2 C_6 coefficients for the Li ($2s^2S_{1/2}$) + Rb ($5p^2P_{3/2}$) asymptote	69
4.5 Strength of photoassociation transitions	71
4.6 Measurement of photoassociation rate in LiRb	73
4.7 Prediction of ground state molecule formation	77
CHAPTER 5. TWO-PHOTON PHOTOASSOCIATION.....	84
5.1 Two-photon photoassociation scheme.....	84
5.2 Experiments and Results.....	86
CHAPTER 6. FUTURE DIRECTIONS	93
6.1 Production and detection of LiRb molecules in the electronic ground state	93
6.2 Alternate schemes for producing ground state LiRb molecules.....	94
6.3 First set of experiments on coherent control.....	97
LIST OF REFERENCES.....	100
APPENDICES	
Appendix A List of observed transitions using FES.....	109
Appendix B External cavity diode lasers.....	119
VITA	119
PUBLICATIONS.....	Error! Bookmark not defined.

LIST OF TABLES

Table	Page
Table 1.1. Until 2011, LiRb was the only bi-alkali molecule for which no experimental study was available.....	6
Table 2.1 Molecular constants (in cm^{-1}) of the $X^1\Sigma^+$ state and f -parity levels of the $B^1\Pi$ state. All values of T_v are referenced to $T_{v''=0} = 0$. The value of $D_{v''}$ is held fixed at $1.06 \times 10^{-6} \text{ cm}^{-1}$. These constants reproduce the observed transition frequencies with an accuracy of 0.02cm^{-1}	23
Table 2.2. The rotationless energy $T_{\Sigma}^0(v_{\Sigma})$ (referenced to $T_{v''=0} = 0$), rotational constant $B_{\Sigma}(v_{\Sigma})$ and the perturbation matrix element $\eta(v_{\Pi}, v_{\Sigma})$ of the $C^1\Sigma^+$ state.	25
Table 3.1. Values of loss rate coefficients (in cm^3/s) measured for conventional bright MOTs. Parameters involving ^6Li are from Ladouceur <i>et al.</i> ⁹² while those involving ^7Li are measured in our experiment. There are no reported measurements for $^7\text{Li} - ^{87}\text{Rb}$. The dependence of loss rate coefficients on the isotopes could be attributable to the binding energy of the highest energy vibrational state within the electronic potential well, or possibly differences in the hyperfine structures of different isotopes ⁷⁷ . In the final row, we present the ratios $\beta_{Li,Rb} / \beta_{Rb,Li}$ for these different isotopic systems.	49
Table 4.1. Correlation between potentials at short and long range.....	57

Table	Page
Table 4.2. The values of $-\Delta_{PA}$ (in GHz) for which PA resonances are observed below the Li ($2s\ ^2S_{1/2}$) + Rb ($5p\ ^2P_{1/2}$) asymptote. Also included is the assignment of the electronic states and the vibrational quantum numbers ν (measured from dissociation limit). For vibrational levels with multiple internal structures, the frequency of line closest to the center of the spectrum is reported. We did not observe the next more deeply bound vibrational state probably due to weak Franck-Condon overlap with the scattering state. The least bound states (bound by less than 8 GHz) could not be observed because the PA laser, with frequency close to D_1 transition, strongly perturbed the operation of the Rb MOT.	63
Table 4.3. The values of C_6 coefficients (in atomic units = Hartree/ $a_0^6 \approx 0.957342 \times 10^{-79} \text{ Jm}^6$) for the Li ($2s\ ^2S_{1/2}$) + Rb ($5p\ ^2P_{1/2}$) asymptote measured experimentally in this work, and a comparison with three different theoretical predictions. The superscripts and subscripts on the experimental values indicate the uncertainties that arise when J is changed by ± 1 . The experimentally determined values of ν_D are also included.	65
Table 4.4. The values of $-\Delta_{PA}$ (in GHz) for which PA lines are observed below the Li ($2s\ ^2S_{1/2}$) + Rb ($5p\ ^2P_{3/2}$) asymptote. Also included are the assignments of the electronic states and the vibrational quantum numbers ν (measured from dissociation limit).	69
Table 4.5. The values of C_6 coefficients (in atomic units) for the Li ($2s\ ^2S_{1/2}$) + Rb ($5p\ ^2P_{3/2}$) asymptote measured experimentally in this work, and a comparison with three different theoretical predictions. The superscripts and subscripts on the experimental values indicate the uncertainties that arise when J is changed by ± 1 . The experimentally determined values of ν_D are also included.	70

Table	Page
Table 5.1. List of the 2-photon PA resonances observed and the values of $\Delta\nu$. The left most column contains the PA level that was used for the Raman-type 2-photon PA scheme while the observed resonances are in the subsequent columns. The frequencies are in GHz.	90

LIST OF FIGURES

Figure	Page
Figure 1.1. Two-color Raman scheme for creating rotational superposition of $J'' = 0$ and $J'' = 1$ levels in the $X^1\Sigma^+$ state.....	10
Figure 2.1. Theoretical potential energy curves for LiRb ⁵⁹	14
Figure 2.2. Experimental setup: LiRb molecules formed at the center of the heat-pipe-oven are excited with a laser, the LIF is collected in the forward direction and sent to a monochromator for detection.....	15
Figure 2.3. LIF spectra originating from $v' = 0, 1, 2$ and 3 levels of the $B^1\Pi$ state and terminating in different v'' levels of the $X^1\Sigma^+$ state. The intensity distribution clearly reflects the node structure of the radial wave functions of the $B^1\Pi$ state. The occurrence of P - R doublets facilitates assignment of J . The dotted lines serve to guide the eye only.....	17
Figure 2.4. LIF after exciting the transition ($v'' = 2, J'' = 6$) \rightarrow ($v' = 20, J' = 6$) with the laser frequency at 18016.42 cm^{-1} . The LIF progression can be followed up to $v'' = 45$. The features due to self absorption of Rubidium vapor are also seen. Inset: Zoomed in view showing the highest observed v'' levels of the $X^1\Sigma^+$ state along with two suspected triplet transitions (indicated by \blacktriangledown).	18

Figure	Page
Figure 2.5. (A) Detection scheme for FES: The monochromator is fixed to detect fluorescence at a frequency $\sim 193 \text{ cm}^{-1}$ less than that of the excitation, and the laser frequency is scanned. (B) A fragment of the Fluorescence Excitation Spectrum near the $(v'' = 0, v' = 2)$ band head. The rotational quantum numbers J' of the P , Q , and R branches are assigned, as indicated on the top. At our resolution, levels $R(1)$, $R(2)$ and $R(3)$ overlap with $R(6)$, $R(5)$ and $R(4)$ respectively.	18
Figure 2.6. (A) A plot (open circles \circ) of $\Delta_2 F_{v''}(J'')$, in cm^{-1} , for the $v'' = 0$ level of the $X^1\Sigma^+$ state. The solid line (red) is a fit to equation (2.6) and the filled circles (\bullet) are the fit residuals. $B_{v''}$ and $D_{v''}$ for the $v'' = 0$ level are obtained from this plot. The excited state involved was the $v' = 2$ level of the $B^1\Pi$ state. (B) A plot (open circles \circ) of $Q(J)$, in cm^{-1} , for transitions from $v'' = 2$ to $v' = 13$. We obtain the values of $B_{v'=13}$, $D_{v'=13}$ and $(T_{v'=13} - T_{v''=2})$ from this plot. Similar plots are made for the Q -lines of other (v'', v') transitions and the respective $B_{v'}$, $D_{v'}$ and $(T_{v'} - T_{v''})$ are obtained.	21
Figure 2.7. The difference between observed and calculated transition frequencies in the $(v''=0, v'=1)$, $(v''=0, v'=2)$ and $(v''=0, v'=3)$ bands of the $X^1\Sigma^+ \rightarrow B^1\Pi$ system. Open circles (\circ) correspond to f parity levels and filled circles (\bullet) correspond to e parity levels. The f parity levels are not perturbed while rotational perturbations are maximum near specific J' values for the e parity levels of the $B^1\Pi$ state.	24
Figure 3.1. Energy level diagram for ^7Li and ^{85}Rb . Lower panels: The saturated absorption signal (red line) and the error signal (black line). The laser frequencies decrease on moving from left to right. The arrows indicate the peaks to which the respective lasers are locked.	28

Figure	Page
Figure 3.2. Schematics of the laser system for our ${}^7\text{Li}$ - ${}^{85}\text{Rb}$ dual species magneto-optical trap (MOT). For the AOMs in double pass configuration, right angled prisms are used to vertically displace the beams. The beams coming out of the two slave lasers are combined on an N-PBS instead of a PBS because the tapered amplifier can amplify light of only one polarization. Note that the cooling and repumping beams for both ${}^7\text{Li}$ and ${}^{85}\text{Rb}$ MOTs are combined and sent to the experiment through the same optical fiber.	29
Figure 3.3. Schematic representation of the vacuum chamber (top) along with a photograph (bottom). The picture was taken before the MOT optics was mounted. The red dot at the center of the UHV chamber represents the MOT. The green lines denote the electric field plates (picture in right inset) which accelerate the ions produced during REMPI towards the MCP, denoted in purple. The trajectory of ions is indicated by the blue lines. The MOT coils are denoted in orange. Left inset: Photograph of the ${}^7\text{Li}$ MOT (indicated by the arrow).	33
Figure 3.4. (A) Photograph of the lithium oven chamber showing the oven, the nozzle and the rotation mount on which the hollow cylindrical beam shutter is mounted (see text for details). (B) Photograph of the nozzle before integration into the vacuum chamber. The stacked hypodermic needles in the central aperture are also visible. (C) Photograph of the atomic beam shutter mounted on a rotation mount. The atom beam is blocked or transmitted depending on the orientation of the aperture. (D) Magnetic field profile of the Zeeman Slower (ZS) solenoid (squares), MOT coils (circles) and their combined magnetic field (solid line).....	34

Figure	Page
Figure 3.5. False color fluorescence images of the MOTs taken with one of the CCD cameras. (A) Rb MOT in absence of Li MOT, (B) Li MOT in the absence of the Rb MOT, and (C) Li MOT in the presence of the Rb MOT (a filter is used to block most of the Rb fluorescence). The reduction in the number of trapped Li atoms due to the presence of the Rb MOT is clearly visible.	40
Figure 3.6. Li and Rb MOT fluorescence signal. The loading sequence is described in the text.	41
Figure 3.7. The dependence of the loss rate coefficients on the detuning (δ_{Li}) of the Li cooling laser. The Li repump detuning is fixed at -18 MHz, the Rb cooling laser detuning is fixed at -24 MHz and the Rb repump is resonant. The filled squares and open circles are the values of $\beta_{Li,Rb}$ and $\beta_{Rb,Li}$ respectively.	45
Figure 3.8. Simultaneous loading of a Li MOT (red, left axis) and dark Rb MOT (black, right axis). The Li MOT starts loading at $t = 10$ s and is allowed to reach steady state. At $t = 50$ s, the Rb dark MOT starts loading and a very small reduction in the Li MOT atom number is seen. At $t = 75$ s the Li MOT is blocked and a very small increase in the dark Rb MOT atom number is seen. The interspecies collision induced losses are greatly reduced when a dark Rb MOT is used.	52

Figure	Page
Figure 3.9. The decay of Li MOT atom number when the Li atomic beam is suddenly blocked at $t = 0$ s. The ratio $N_{Li}/N_{Li,Max}$ in linear scale (A) and log scale (B) as a function of time after the atomic beam is blocked. In absence of the Rb MOT, the Li atoms number decreases slowly with a lifetime ~ 7.5 s. In the presence of the bright Rb MOT, the Li atoms number decreases much more quickly with a lifetime ~ 1.7 s. In the presence of the dark Rb MOT, the Li atoms number decreases slowly with a lifetime ~ 6.5 s. This suppression of collision induced losses with a dark Rb MOT indicates that the Li losses are mainly due to collision of Li with excited state Rb atoms.	54
Figure 4.1. a) Theoretical potential energy curves of LiRb for small internuclear separations ⁶⁰ . (b) Theoretical potential energy curves at large internuclear separations determined solely by the C_6 coefficients ⁸⁸ . Only these curves are relevant to the presented PA measurements.	57
Figure 4.2. PA spectrum of LiRb* below the Li ($2s^2S_{1/2}$) + Rb ($5p^2P_{1/2}$) asymptote measured using trap loss spectroscopy. (a) Compilation of all strong PA lines. (b-j) Zoom-in view showing the internal structures of the PA lines. The electronic states and vibrational levels (measured from the dissociation limit) are also indicated.	60
Figure 4.3. The fit of experimentally observed PA frequencies to the LRB formula as described in the text. Note that the data points for the 2(0) and 2(1) states lie almost on top of each other. Also note that the slopes of all the curves are similar indicating that the C_6 coefficients for all three electronic states are similar.	65

Figure	Page
Figure 4.4. PA spectra of LiRb below the Li ($2s\ ^2S_{1/2}$) + Rb ($5p\ ^2P_{3/2}$) asymptote obtained using trap loss spectroscopy. The filled circles, open circles, open rhombus and filled rhombus indicate lines belonging to the 4(1), 3(0^+), α and β states, respectively, while the numbers indicate the vibrational level ν measured from the dissociation limit (see text for details).....	66
Figure 4.5. The PA spectra of all the 4(1) states observed in this thesis. The vibrational number ν (measured from dissociation) is also labeled.	67
Figure 4.6. PA spectra for the 3(0^+) state (open circles), the α state (open rhombus) and β state (filled rhombus). In panel (a), the weaker peak \sim 800 MHz to right of the main peak arises from collision along the the Li ($2s\ ^2S_{1/2}, F = 1$) + Rb ($5s\ ^2S_{1/2}, F = 2$) channel due to imperfect hyperfine repumping in the Li MOT.	68
Figure 4.7. The fit to the LRB formula that is used to extract the C_6 coefficients from the experimentally measured PA line positions. The data points and fits for the states α , β and 4(1) lie almost on top of each other.	70
Figure 4.8. Schematic representation of the initial low-energy scattering radial wave function and the final bound vibrational wave function.	71
Figure 4.9. The relative values of Franck-Condon factors for heteronuclear photoassociation transitions at long range calculated based on reflection approximation. These calculations deviate significantly from experimental observations for LiRb. The figure is adapted from ref. 100.....	72
Figure 4.10. Rescaled PA rates (when atoms collide along the $X\ ^1\Sigma^+$ potential) for (a) Cs compounds and (b) Rb compounds, for the $X\ ^1\Sigma^+ \rightarrow 0^+$ ($A\ ^1\Sigma^+$) transition as a function of the detuning of the PA laser below the Li ($2s\ ^2S_{1/2}$) + Rb ($5p\ ^2P_{1/2}$) or analogous asymptotes. Single channel calculations and coupled channel calculations (with spin-orbit coupling included) resulted in similar PA rates. The figure is adapted from ref. 101.....	73

Figure	Page
Figure 4.11. (a) The evolution of the atom number N_{Li} in the Li MOT when the on resonance PA light ($\nu_{PA} = 384217.07$ GHz, for the $\nu = 3$ level of the $3(0^+)$ state) is turned on at $t = 0$. The LiRb* production rate (P_{LiRb}) is estimated from the slope near $t = 0$. The saturation of P_{LiRb} is clearly visible for intensities (I) beyond 60 W/cm^2 . (b) The PA rate coefficient (K_{PA}) as a function of the average PA laser intensity. The rate starts to saturate beyond 60 W/cm^2 . The dotted line is a linear fit of K_{PA} in the low-intensity regime with a slope $2 \times 10^{-12} (\text{cm}^3/\text{s})/(\text{W/cm}^2)$. The solid line is a fit of K_{PA} to the equation ¹⁰² $K_{PA} = 4K_{PA,\text{max}} / (1 + I_{\text{sat}} / I)$ with $K_{PA,\text{max}} = 1.6(\pm 0.5) \times 10^{-10} \text{ cm}^3/\text{s}$ and $I_{\text{sat}} = 300 \pm 100 \text{ W/cm}^2$. (c) Comparison of PA rate coefficient K_{PA} of different polar molecules. The left (dark color, exp) bars denote the maximum experimentally observed values of K_{PA} while the right (light color, th) bars denote the theoretical values at the unitarity limit at the temperatures indicated. Even at a relatively high temperature, the K_{PA} for LiRb is the highest and is close to the theoretical prediction of the unitarity limit.	76
Figure 4.12. Top panel: The wave function of the scattering state. The red line is for scattering along the $X^1\Sigma^+$ potential and the black line is for scattering along the $a^3\Sigma^+$ potential. Bottom panel: The wave function for different vibrational levels (ν') of the $B^1\Pi$ state. All level shown in this figure, except $\nu' = 20$, have been observed experimentally using PA. Calculation and figure courtesy: Jesús Pérez-Ríos.	79

Figure	Page
Figure 4.13. (a) The free-bound FC overlap between the scattering state (scattering along the $X^1\Sigma^+$ and the $a^3\Sigma^+$ potentials) and the different vibrational levels (v') of the $B^1\Pi$ state. (b) Bound-bound FC overlap between different vibrational levels (v') of the $B^1\Pi$ state and the different vibrational levels (v'') of the $X^1\Sigma^+$ state (plotted along the abscissa). We note that the calculation is in qualitative agreement with our LIF data for $v' = 20$. (c) The plot of molecule production efficiency η in different vibrational levels (v'') of the $X^1\Sigma^+$ state for PA to a few different vibrational levels (v') of the $B^1\Pi$ state, assuming that atoms collide along the $X^1\Sigma^+$ potential. Calculation and figure courtesy: Jesús Pérez-Ríos.	80
Figure 4.14. The schemes that can be used to transfer LiRb molecules to the $X^1\Sigma^+$ ($v'' = 0$) state. (a) Scheme involving PA followed by spontaneous emission (SE) only. (b) Scheme involving PA followed by SE, followed by STIRAP. See text for details.	82
Figure 5.1. Scheme used for Raman-type 2-photon PA. The frequency ν_{PA} of the PA laser is held fixed at a free-bound PA transition which induces atom losses. The frequency ν_R of the Raman laser is scanned across a bound-bound transition. When the frequency ν_R is resonant with a bound-bound transition, the PA-induced atom losses are suppressed and an increase in MOT fluorescence is seen.	85
Figure 5.2. (a) 1-photon PA spectrum below the Li ($2s^2S_{1/2}$) + Rb ($5p^2P_{1/2}$) asymptote (this figure is the same as figure 4.2g). The frequency of the ECDL is locked to the PA resonance indicated by the arrow. (b) 2-photon PA spectra when the frequency of the Raman laser is scanned, with the ECDL locked to the PA line indicated by the arrow in (a).	87
Figure 5.3. Schematic representation of the hyperfine manifolds in the scattering state and in the loosely bound levels of the $X^1\Sigma^+$ and the $a^3\Sigma^+$ states (see text for details).	91

Figure	Page
Figure 6.1. (a) The REMPI scheme used to detect ultracold LiRb molecules produced in the electronic ground state. (b) An oscilloscope trace of the TOF spectrum. The spectrum is obtained with ~ 100 individual REMPI pulses. The Rb^+ ions arrive at the detector (MCP) earlier than the LiRb^+ ions. The arrival windows of the Rb^+ and LiRb^+ ions are well separated and hence Rb^+ and LiRb^+ ions can be easily distinguished.	94
Figure 6.2. Two-color Raman scheme for creating rotational superposition of $J'' = 0$ and $J'' = 1$ levels in the $X^1\Sigma^+$ ($v'' = 51$) state.....	98
Appendix Figure	
Figure A 1 The transition frequencies of all Q branch transitions observed in this study plotted against $J(J + 1)$. For clarity, even and odd v' levels are denoted by open circles (\circ) and filled circles (\bullet) respectively.....	105

ABSTRACT

Dutta, Sourav Ph.D., Purdue University, December 2013. Experimental Studies of LiRb: Spectroscopy and Ultracold Molecule Formation by Photoassociation. Major Professor: Yong P. Chen.

Heteronuclear polar molecules have recently attracted enormous attention owing to their ground state having a large electric dipole moment. The long range anisotropic dipole-dipole interaction in such systems is the basis for a variety of applications including quantum computing, precision measurements, ultracold chemistry and quantum simulations. Heteronuclear bi-alkali molecules, only a small subset of polar molecules, have received special attention mainly because the constituent alkali atoms are easy to laser cool and can be relatively easily associated to form molecules at ultracold temperatures. Our choice, the LiRb molecule, is motivated by the relatively high dipole moment (4.1 Debye) of the LiRb molecule in its rovibronic ground state. In this thesis, we study the LiRb molecule using laser spectroscopy and report, for the first time, the production of ultracold LiRb molecules by photoassociation (PA).

The LiRb molecule is the least studied among all bi-alkali molecules and the first spectroscopic measurements on hot vapor phase LiRb molecules were reported only in 2011. We describe these measurements and their significance in chapter 2, after a brief introduction to the field of ultracold polar molecules in chapter 1. In chapter 3, we discuss our apparatus for simultaneous cooling and trapping of Li and Rb atoms in a

dual-species magneto-optical trap (MOT) and report the measurement of interspecies collision-induced losses. In chapter 4, we describe the production of ultracold LiRb molecules in excited electronic states by photoassociation (PA). We report the measurements of the C_6 coefficients for the Li ($2s\ ^2S_{1/2}$) + Rb ($5p\ ^2P_{1/2}$) and the Li ($2s\ ^2S_{1/2}$) + Rb ($5p\ ^2P_{3/2}$) asymptotes. We find a molecule formation rate (P_{LiRb}) as high as $3.5 \times 10^7\ \text{s}^{-1}$ and a PA rate coefficient (K_{PA}) as high as $1.3 \times 10^{-10}\ \text{cm}^3/\text{s}$, the highest among heteronuclear bi-alkali molecules. In chapter 5, we discuss results on two-photon PA and we conclude, in chapter 6, with a road roadmap of future experiments for the production and detection of ultracold LiRb molecules in their rovibronic ground state.

CHAPTER 1. INTRODUCTION

1.1 The rising interest in cold molecules

The field of laser cooling and trapping has a long and exciting history dating back to 1975 when the idea was first proposed independently by Hänsch and Schawlow and by Wineland and Dehmelt. Experimental efforts soon followed and Wineland *et al.* reported the first experiment on laser cooling of Mg ions in 1978¹. The possibility of reaching ultracold (sub- μ K) temperatures, where the system's properties are defined by the underlying quantum statistics, attracted researchers from all over the world and a race to absolute zero began. With the rapid development of the techniques, it was not long before the first experiments on laser cooling and trapping of atoms were realized circa 1985. The wonderful effort was recognized with the 1997 Nobel Prize in Physics (See, for example, the Nobel Lectures by William D. Phillips, Steven Chu and Claude Cohen-Tannoudji for beautifully written accounts of the journey). This was just one milestone with many others to follow, one of which was the realization of Bose Einstein Condensation (BEC) of neutral alkali atoms in 1995, for which Eric A. Cornell, Carl E. Wieman and Wolfgang Ketterle were awarded the 2001 Nobel Prize in Physics. Today, there are more than one hundred groups working on laser cooling and trapping of atoms, among whom some groups (like ours) are also interested in molecules. While precise knowledge and control of the numerous physical phenomena in ultracold atoms are extremely promising and

rewarding in their own rights, extending such knowledge and control over ultracold polar molecules can open exciting new research directions^{2,3,4}. The large number of electronic, vibrational and rotational degrees of freedom available in molecules makes them attractive systems for many applications^{2,3,4,5,6,7,8,9,10,11,12,13,14,15}. The relatively strong dipole-dipole interaction, which is also long range and anisotropic, makes ultracold polar molecules interesting systems for studying dipolar collisions⁹, quantum state controlled chemical reactions^{10,11}, novel quantum phases^{12,13} and quantum information^{14,15}. Our research on ultracold molecules is primarily motivated by our interest in quantum computing, specifically in coherent control^{16,17,18,19,20} of molecular states.

The plethora of internal structure makes molecular systems very rich but also makes them extremely challenging to cool and trap. Due to numerous vibrational and rotational degrees of freedom, the usual methods of cooling and trapping of atoms do not work for molecules. Alkali metal atoms, for example, can be cooled to below mK temperatures in a magneto-optical-trap (MOT) using two lasers called the cooling and the repumping lasers²¹. This is possible because of the presence of closed cycling transitions in atoms which allows them to undergo $\sim 10^4$ absorption and emission cycles before they fall out of the cycling transition. When the atom does eventually fall out of the cycling transition, only one repumping laser is sufficient to bring it back to the cycling transition. This simple method does not work in molecules because molecules do not have closed cycling transitions. While there are selection rules governing rotational and electronic transitions in molecules, there is no strict selection rule governing the vibrational transitions in molecules. As a result, molecules in an excited state can fluoresce back to many vibrational levels of the ground state, the branching ratio determined by the so called

Franck-Condon overlap²². This implies that numerous repumping lasers would be required for cooling and trapping of molecules unless the molecule under investigation has a highly diagonal Franck-Condon (FC) factor like CaH, SrF, TiO, AlH⁺ etc.^{23,24,25}. In particular, SrF was recently laser cooled to a few mK temperature using only three lasers^{24,25}. In the absence of such diagonal Franck-Condon factors, molecules have been cooled to ~ 10-100 mK using various techniques including buffer gas cooling, Stark deceleration, magnetic and optical deceleration, velocity filtering and kinematic collisions^{26,27,28,29,30,31,32,33,34,35}. There are also some proposals on cooling molecules using high-finesse optical cavities as well as free space laser cooling^{36,37,38,39}. Cold molecules obtained using these techniques have been trapped using electric or magnetic fields^{40,41,35}. To produce molecules at even lower temperatures, the most widely used techniques are photo-association (PA) of atoms^{42,43,44} or magneto-association (MA) of atoms followed by Stimulated Raman Adiabatic Passage (STIRAP)⁸. The second technique, although elegant, works only for species with favorable Feshbach resonances, while the first technique (i.e. PA) is more general and can be used to produce ultracold ground-state molecules with PA followed by spontaneous emission⁴⁴. In the chapters that follow, I will describe the complete scheme based on PA that we wish to implement for the production and detection of ultracold LiRb molecules. Here I provide a summary and the overall goal of the project.

1.2 Creating ultracold molecules from ultracold atoms

Our molecule of choice is LiRb, a heteronuclear bi-alkali diatomic molecule predicted to have a relatively large electric dipole moment of 4.1 Debye⁴⁵ (exceeded only by LiCs

and NaCs). It is also interesting to note that Rb has two bosonic isotopes (^{85}Rb and ^{87}Rb) and Li has two isotopes, one of which (^6Li) is a fermion while the other (^7Li) is a boson. A LiRb molecule formed can be a fermion or a boson depending on the Li isotope chosen, broadening the range of physics that can be studied. An important consideration while choosing the heteronuclear molecule (XY, where X and Y are two different alkali atom species) to be studied is its collisional properties in its rovibrational ground state. Particularly detrimental are reactive collisions. The two reactions that need to be considered are (i) $\text{XY} + \text{XY} \rightarrow \text{X}_2 + \text{Y}_2$ and (ii) $\text{XY} + \text{XY} \rightarrow \text{X} + \text{XY}_2$ or $\text{X}_2\text{Y} + \text{Y}$. It was theoretically shown⁴⁶ that the latter trimer formation reaction is energetically forbidden for all heteronuclear molecules but the former atom exchange reaction is energetically allowed for all heteronuclear Li dimers and KRb. Although the atom exchange reaction poses a serious concern for LiRb, it was recently experimentally demonstrated that such reactive collisions can be significantly suppressed by trapping the molecules in an optical lattice^{11,47} and lifetimes of 25 seconds have been achieved in a three dimensional optical lattice⁴⁷.

In order to create ultracold LiRb molecules, we start with ultracold samples of Li and Rb atoms produced using the standard techniques of laser cooling and trapping alkali metal atoms in a MOT. We want to create molecules at ultralow temperatures using a technique called photoassociation (PA). PA is a process in which two atoms interact with a laser to form a molecule in an excited electronic state. The excited state molecule quickly decays, by emitting a photon, either into two free atoms or into a bound state molecule in the electronic ground state. The second outcome gives a possible route for the creation of molecules in their electronic ground state. The temperature of the

molecules produced using PA is comparable to the temperature of the atoms from which they were produced. The strength of the PA transition depends, among other things, on the Frank-Condon (FC) overlap between the wave function of the excited electronic state and the initial scattering state. This overlap is good for high vibrational levels of the excited electronic state implying higher PA strengths. The molecules in high vibrational levels of the excited electronic state generally decay to high vibrational levels of the ground electronic state owing to the better FC overlap between these states. Thus, although the molecules produced by PA are cold, they are generally created in high vibrational levels of the ground state. This obviously is not the most desirable outcome because molecules in high vibrational levels eventually decay to lower vibrational levels making the molecules in high vibrational levels unsuited for many applications. A major challenge is to overcome this limitation and create molecules in their lowest rotational, vibrational and electronic state. One of the goals of my thesis is to propose efficient PA pathways for the production of ultracold ground state LiRb molecules, and their detection via state selective ionization³. In order to create and detect ultracold LiRb molecules, it is critical to precisely know the electronic, vibrational and rotational energy levels of the ground and excited states of the molecule. This information, somewhat surprisingly, was missing because of lack of spectroscopic investigation of LiRb (see Table 1.1). To quote my advisor Yong: “*LiRb is the so-called last alkali dimer*”.

I will describe, in chapter 2, our work on spectroscopy of ${}^7\text{Li}{}^{85}\text{Rb}$ molecules in hot (800 K) vapor phase from which we derive the electronic, vibrational and rotational energy levels of the ground $X\ ^1\Sigma^+$ state and the excited $B\ ^1\Pi$ state. I will also discuss the importance of this work in predicting efficient pathways for the production and detection

Table 1.1. Until 2011, LiRb was the only bi-alkali molecule for which no experimental study was available.

	Li	Na	K	Rb	Cs
Li	HM: (a) PA: (b) FA: (ab)	HM: (c) PA: – FA: (d)	HM: (e) PA: (f) FA: (ac)	HM: This work (aj) & Tiemann's work (ak) PA: This work FA: (al)	HM: (g) PA: (h) FA: (ad)
Na		HM: (i) PA: (j) FA: (ae)	HM: (k) PA: – FA: (l)	HM: (m) PA: – FA: (n)	HM: (o) PA: (p) FA: –
K			HM: (q) PA: (r) FA: (af)	HM: (s) PA: (t) FA: (t)	HM: (u) PA: – FA: –
Rb				HM:(v) PA: (w) FA: (ag)	HM: (x) PA: (y) FA: (ah)
Cs					HM: (z) PA: (aa) FA: (ai)

HM: Hot molecule, PA: Photoassociation, FA: Feshbach association. The references are not necessarily the first experimental reports.

- (a) J. A. Coxon & T. C. Melville, *J. Mol. Spectrosc.* 235, 235 (2006).
 (b) E. R. I. Abraham et al. *J. Chem. Phys.* 103, 7773 (1995). [Group of R. G. Hulet]
 (c) F. Engelke, G. Ennen & K. H. Meiwes, *Chem. Phys.* 66, 391 (1982).
 (d) M. Heo et al., *Phys. Rev. A* 86, 021602(R) (2012). [Group of W. Ketterle]
 (e) V. Bednarska et al., *J. Chem. Phys.* 106, 6332 (1997). [Group of P. Kowalczyk & W. Jastrzębski]
 (f) A. Ridinger et al., *Europhysics Letters* 96, 33001 (2011). [Group of C. Salomon & F. Chevy]
 (g) P. Staunum et al., *Phys. Rev. A* 75, 042513 (2007). [Group of E. Tiemann]
 (h) J. Deiglmayr et al., *Phys. Rev. Lett.* 101, 133004 (2008). [Group of M. Weidemüller]
 (i) R. F. Barrow, J. Verges, C. Effantin, K. Hussein, J. Dincan, *Chem. Phys. Lett.* 104, 179 (1984).
 (j) P. D. Lett, K. Helmerson, W. D. Phillips, L. P. Ratliff, S. L. Rolston, & M. E. Wagshul, *Phys. Rev. Lett.* 71, 2200 (1993).
 (k) E. J. Breford & F. Engelke, *J. Chem. Phys.* 71, 1994 (1979).
 (l) C. Wu et al., *Phys. Rev. Lett.* 109, 085301 (2012). [Group of M. W. Zwierlein]
 (m) N. Takahashi & H. Katô, *J. Chem. Phys.* 75, 4350 (1981).
 (n) F. Wang et al., *Phys. Rev. A* 87, 050702(R) (2013). [Group of Dajun Wang]
 (o) O. Docenko et al., *Eur. Phys. J. D* 31, 205 (2004). [Group of E. Tiemann]
 (p) P. Zabawa et al., *Phys. Rev. A* 84, 061401(R) (2011). [Group of N. P. Bigelow]
 (q) W. J. Tango, J. K. Link & R. N. Zare, *J. Chem. Phys.* 49, 4264 (1968).
 (r) W. C. Stwalley & H. Wang, *J. Mol. Spectrosc.* 195, 194 (1999).
 (s) A. Pashov et al., *Phys. Rev. A* 76, 022511 (2007). [Group of E. Tiemann]
 (t) D. Wang et al., *Phys. Rev. Lett.* 93, 243005 (2004), [Group of P. L. Gould, E. E. Eyler & W. C. Stwalley]
 K. K. Ni et al., *Science* 322, 231 (2008). [Group of D. S. Jin & J. Ye]
 (u) R. Ferber... E. Tiemann & A. Pashov, *J. Chem. Phys.* 128, 244316 (2008).
 (v) C. Amiot, *J. Chem. Phys.* 93, 8591 (1990).
 (w) J. D. Miller, R. A. Cline & D. J. Heinzen, *Phys. Rev. Lett.* 71, 2204 (1993).
 (x) H. Katô & H. Kobayashi, *J. Chem. Phys.* 79, 123 (1983).
 (y) A. J. Kerman et al., *Phys. Rev. Lett.* 92, 033004 (2004). [Group of D. DeMille]
 (z) C. Amiot & O. Dulieu, *J. Chem. Phys.* 117, 5155 (2002).
 (aa) A. Fioretti et al., *Phys. Rev. Lett.* 80, 4402 (1998). [Group of P. Pillet]
 (ab) K. E. Strecker et al., *Nature* 417, 150 (2002). [Group of R. G. Hulet]
 (ac) E. Wille et al., *Phys. Rev. Lett.* 100, 053201 (2008). [Group of R. Grimm]
 (ad) M. Repp et al., *Phys. Rev. A* 87, 010701(R) (2013). [Group of M. Weidemüller]
 (ae) S. Inouye et al., *Nature* 392, 151 (1998). [Group of W. Ketterle]
 (af) C. A. Regal, M. Greiner & D. S. Jin, *Phys. Rev. Lett.* 92, 040403 (2004). [Group of D. S. Jin]
 (ag) N. R. Claussen et al., *Phys. Rev. A* 67, 060701(R) (2003). [Group of C. E. Wieman]
 (ah) T. Takekoshi et al., *Phys. Rev. A* 85, 032506 (2012). [Group of R. Grimm]
 (ai) C. Chin et al., *Phys. Rev. A* 70, 032701 (2004). [Group of S. Chu]
 (aj) Sourav Dutta et al., *Chem. Phys. Lett.* 511, 7 (2011). [Group of D. S. Elliott & Yong P. Chen]
 (ak) M. Ivanova et al., *J. Chem. Phys.* 134 024321 (2011), *J. Chem. Phys.* 138, 094315 (2013). [Group of E. Tiemann]
 (al) Z. Li et al., *Phys. Rev. A* 78, 022710 (2008); B. Deh et al., *ibid* 82, 020701 (2010). [Group of K. Madison]
 B. Deh et al., *ibid* 77, 010701 (2008); C. Marzok et al., *ibid* 79, 012717 (2009), [Group of C. Zimmerman & P. Courteille]

of ground-state LiRb molecules. In chapter 3, I will describe our apparatus for simultaneous cooling and trapping of Li and Rb atoms in a dual-species magneto-optical trap (MOT) and discuss the measurement and mitigation of interspecies collision-induced losses.

In chapter 4, I will describe the production of ultracold LiRb molecules in excited electronic states by photoassociation (PA) and derive of the C_6 coefficients for the Li ($2s\ ^2S_{1/2}$) + Rb ($5p\ ^2P_{1/2}$) and the Li ($2s\ ^2S_{1/2}$) + Rb ($5p\ ^2P_{3/2}$) asymptotes. I will also discuss the measurement of PA rates. For the strongest PA transition observed, we report a molecule formation rate (P_{LiRb}) of $3.5 \times 10^7\ \text{s}^{-1}$ and a PA rate coefficient (K_{PA}) of $1.3 \times 10^{-10}\ \text{cm}^3/\text{s}$, the highest among heteronuclear bi-alkali molecules. In chapter 5, I will discuss some results on two-photon PA and I will conclude, in chapter 6, with a roadmap of future experiments for the production of ultracold LiRb molecules in their rovibronic ground state and some future experiments on coherent control. In the remainder of the chapter, I discuss how the idea of all optical coherent control can be used to manipulate qubits, which in our case are rotational states of the ultracold polar LiRb molecules.

1.3 Quantum computing with ultracold polar molecules

The individual unit of classical computers is the bit which can be in two states represented by 0 and 1. The corresponding unit of quantum computers is the quantum bit or qubit which can be in two states denoted as $|0\rangle$ and $|1\rangle$. A single bit or qubit can represent at most two numbers, but qubits can be put into infinitely many other states by superposition:

$$|\psi\rangle = \alpha|0\rangle + \beta|1\rangle$$

where α and β are complex numbers with $|\alpha|^2 + |\beta|^2 = 1$. In a superposition state, a quantum register consisting of N qubits can store 2^N bits of information simultaneously, whereas only N bits of information are stored in a classical register. This quantum parallelism makes quantum computers much faster because they can process quantum superposition of many numbers in one computational step, each computational step being a unitary transformation of the quantum register^{48,49,50}. These unitary transformations are called quantum logic gates and quantum computers consist of quantum circuits of quantum logic gates. It is now known that all sets of universal gates must include a local operation on a single qubit and a two-qubit non-local operation giving rise to entangled states. Any two-level system (e.g. spin-1/2 systems, two level atoms) can be used for physical realization of a qubit with the two levels acting as the two qubit states. A single qubit operation, as the name suggests, is an operation (Hamiltonian) that affects the quantum state of only the qubit under consideration, leaving all other qubits unchanged. An example of a single qubit operation is Bloch rotation which is simply the time evolution of the quantum state of a qubit under the operation of some Hamiltonian. A two-qubit operation involves two qubits and an example of such an operation in the controlled not (CNOT) gate. In this operation, the state of the target qubit B is flipped (i.e. $|0\rangle_B \leftrightarrow |1\rangle_B$) if the control qubit A is in the state $|1\rangle_A$; else qubit B is left unaffected. The combination of a CNOT gate and a single-qubit gate is sufficient to perform any arbitrary quantum computation. In many ways, a CNOT gate is similar to a NAND gate which is a universal gate in classical computation.

It is difficult to envision the most efficient physical system for implementation of a quantum computer and many systems are being studied. At present, some of the promising directions are: cold trapped ions, neutral atoms in optical lattices, nuclear magnetic resonance, topological quantum computing, Rydberg blockade, cold polar molecules etc. What make a quantum computer somewhat elusive are the two requirements which are difficult to satisfy simultaneously: weak coupling to the environment to avoid decoherence, but also strong coupling to some external field which allows manipulation of qubits. The two requirements can peacefully coexist in a system with ultracold polar molecules and the idea of using polar molecules as qubits was first proposed by DeMille in 2002¹⁴. The properties required of polar molecules for realistic implementation of quantum gates have been succinctly expressed in chapter 17 of Ref. 3. Qubits should interact strongly with each other to enable fast one and two qubit operations. This can be achieved by putting qubits (dipoles) as close as possible and by using molecules with large dipole moments. The states in which qubits are stored, $|0\rangle$ and $|1\rangle$, should have long lifetimes. All these requirements are fulfilled by rovibrational ground state molecules. To reduce decoherence, the information should be stored in qubits which interact minimally with the environment i.e. qubits that have negligible dipole moment should be used for information storage. Schemes involving switching strong dipoles on and off at the appropriate times have been proposed to eliminate decoherence¹⁵.

In a given rotational state, even a polar molecule has no permanent electric dipole moment although there is separation of charges and dipole moment in the body-fixed

frame of the molecule (see chapter 2 of Ref. 3). A permanent electric dipole is created when two rotational states of opposite parity, say $J = 0$ and $J = 1$, are mixed. This mixing can be achieved by applying an external electric field as proposed by DeMille. The molecules which are primarily in $\tilde{J} = 0$ ($\tilde{J} = 1$) with a small $J = 1$ ($J = 0$) admixture align along (against) the external electric field. The tilde on \tilde{J} indicates that J is no longer a good quantum number. From here on, the molecular dipoles (qubits) in $\tilde{J} = 0$ and $\tilde{J} = 1$ states will be denoted by $|0\rangle$ and $|1\rangle$ respectively. Another technique to create mixed states, which we envision exploring, is to use a two-color Raman scheme to couple the pure $J'' = 0$ and $J'' = 1$ levels of the of the $X^1\Sigma^+$ ($v'' = 0$) state. This idea of creating a coherent superposition between the $J'' = 0$ and $J'' = 1$ states is illustrated in Figure 1.1.

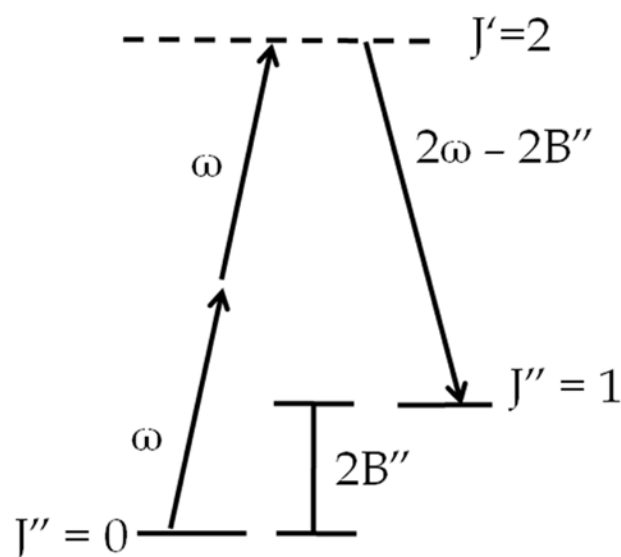


Figure 1.1. Two-color Raman scheme for creating rotational superposition of $J'' = 0$ and $J'' = 1$ levels in the $X^1\Sigma^+$ state

The upward leg of the Raman transition is a two photon transition ($\lambda \sim 1070$ nm) coupling the $X^1\Sigma^+$ ($v'' = 0$, $J'' = 0$) state to a high lying vibrational level of the $B^1\Pi$ state

with $J' = 2$. The downward leg of the Raman transition is a one photon transition ($\lambda \sim 535$ nm) which couples the excited $B^1\Pi$ state to the $X^1\Sigma^+$ ($v'' = 0, J'' = 1$). To maintain coherence, the light for the one photon transition ($\lambda \sim 535$ nm) is obtained by frequency doubling the ($\lambda \sim 1070$ nm) light and phase modulated at a frequency of $2B''$ (≈ 12.94 GHz) using a resonant electro-optic-modulator (EOM). The lower frequency sideband drives the downward leg of the Raman transition. (Note: The higher frequency sideband is not resonant with any electronic transition but the carrier frequency is resonant with the upwards leg of the Raman transition. This is not a problem because one-photon transitions with $\Delta J = 2$ are not allowed). The Raman scheme for creating superposition can of course be realized with any pair of wavelengths, different from the 1070 nm – 535 nm pair suggested above, as long as they are resonant with some electronic transition. However, there are two advantages of using the pair mentioned: (i) high power fiber lasers and amplifiers are available near 1070 nm which is required for the weak two-photon transition, and (ii) the wavelength of the laser we will use to create an optical dipole trap (and an optical lattice) is around 1070 nm and this itself could serve as one of the Raman lasers.

Once the dipoles and hence the qubits are created, the scheme that DeMille proposed can be used to implement gate operations. In his scheme, the dipoles, each with dipole moment \vec{d} , are arranged in a 1D array formed using an optical lattice, where a spatially dependent electric field $\vec{E}_{ext}(x)$ also coexists. The energy $\vec{d} \cdot \vec{E}_{ext}$ and hence the transition frequency of each dipole is different allowing individual addressing of single qubits for single-qubit gate operations. Large dipole moments and large external electric fields are

desirable because the frequency resolution required to address adjacent qubits decrease as $\vec{d} \cdot \vec{E}_{ext}$ increases. The dipole-dipole interaction

$$U_{int} = \frac{\vec{d}_1 \cdot \vec{d}_2 - 3(\hat{r} \cdot \vec{d}_1)(\hat{r} \cdot \vec{d}_2)}{4\pi\epsilon_0 |\vec{r}|^3}$$

allows the two-qubit CNOT gate operation to be performed. The fringing fields from dipole A adds or subtracts from the external field $\vec{E}_{ext}(x)$, at the location of dipole B depending on how the dipole A is oriented with respect to dipole B. This in turn implies that the energy required to flip dipole B depends on the state of dipole A, thus producing entanglement. By tuning the drive frequency appropriately, it is then possible to flip qubit B if and only if qubit A is in state $|1\rangle$, thus realizing a CNOT gate. The key to fast and reliable CNOT gate operation is the large dipole-dipole interaction. The energy shift U_{int} between two adjacent dipoles determines the time required for a CNOT gate: $\tau \approx (U_{int} / \hbar)^{-1}$. In addition, the frequency resolution required to address adjacent qubits for two-qubit operations also decreases as U_{int} increases. Instead of using a set of frequencies as an instruction set, it is possible to use the phase of a laser to address individual qubit. The phase within a laser beam can be conveniently controlled using a spatial light modulator and such optical phase based coherent control schemes allow individual and parallel addressing of qubits. While these ideas will continue to be developed and improved, the goal of my thesis is to produce ultracold LiRb molecules by PA and predict pathways for the production of LiRb molecule in its absolute ground state.

CHAPTER 2. SPECTROSCOPY OF HOT LiRb MOLECULES

Part of this chapter was published as: S. Dutta, A. Altaf, D. S. Elliott, and Y. P. Chen, *Chemical Physics Letters* 511, 7-11 (2011).

The spectroscopy of heteronuclear diatomic bi-alkali molecules provides critical information for the rapidly developing field of ultracold molecules. Although two groups reported observation of Feshbach resonances in an ultracold mixture of Li and Rb atoms^{51,52,53,54}, until the very recent work of Ivanova *et al.*^{55,56} and our work⁵⁷, the LiRb molecule was the only bi-alkali molecule for which no detailed spectroscopic investigation had been reported. In ref. 55, the ground $X^1\Sigma^+$ state was studied using Fourier transform spectroscopy and the potential energy curve was constructed. There were no reports on experimental studies of the excited electronic states of this molecule and we studied the excited $B^1\Pi$ state of LiRb using laser spectroscopy (after our report⁵⁷ there was another report⁵⁶ on excited states of LiRb). The first theoretical calculation of the potential energy curves for LiRb was carried out by Igel-Mann *et al.*⁵⁸ in 1986. More recently, Korek *et al.*^{59,60} calculated the *ab initio* potential energy curves for LiRb – some of which are shown in Figure 2.1. The excited $B^1\Pi$ state of LiRb is a promising intermediate state for the formation of ultracold LiRb molecules by photoassociation^{61,62}, and also for their detection via state selective ionization. In this chapter, we discuss a

high resolution spectroscopic study of the $B^1\Pi$ state using Fluorescence Excitation Spectroscopy (FES). In addition, we also briefly report an independent study of the $X^1\Sigma^+$ state.

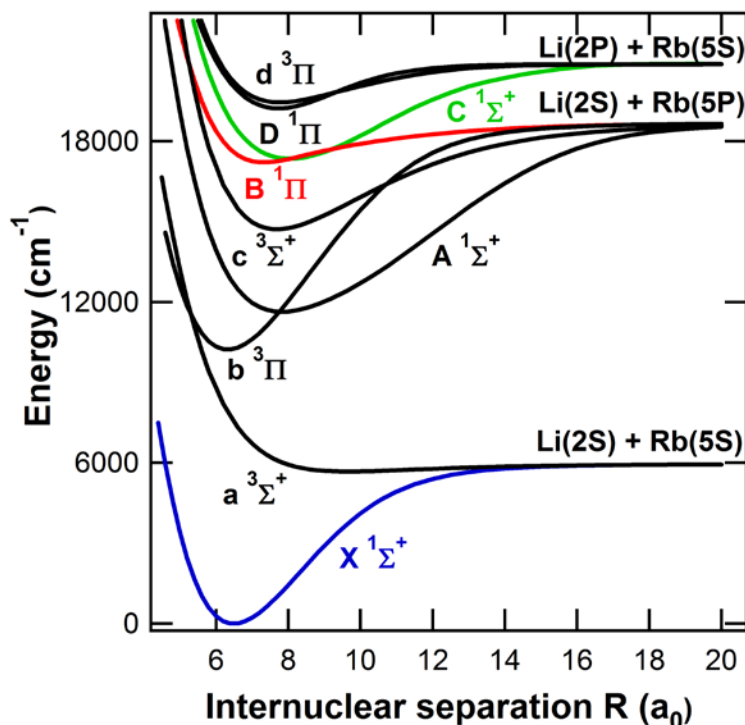


Figure 2.1. Theoretical potential energy curves for LiRb⁵⁹.

2.1 Spectroscopy of LiRb in a heat-pipe oven

We performed spectroscopic measurements on LiRb molecules produced in a 80 cm long three-section heat-pipe oven similar to the one described by Bednarska *et al.*⁶³. This heat-pipe oven, schematically shown in Figure 2.2, allows us to produce Li and Rb vapors at similar densities, despite the large vapor pressure difference of these metals at a common temperature. We loaded 10 g of Li (natural isotopic abundance) in the central section (~15 cm long) of the heat pipe oven, which was heated to 550 °C. The two outer sections (each ~10 cm long), each containing 5 g of Rb (natural isotopic abundance),

were maintained at a lower temperature of 300 °C. We used Argon as a buffer gas at a pressure of approximately 4–5 Torr and water cooled the two ends of the heat-pipe oven to protect the optical windows from deposition of metal. Under these conditions, LiRb molecules formed in the central section of the heat-pipe oven (along with Li₂ and Rb₂ molecules). We operated the heat-pipe oven for more than 800 hours over a period of 14 months without refilling.

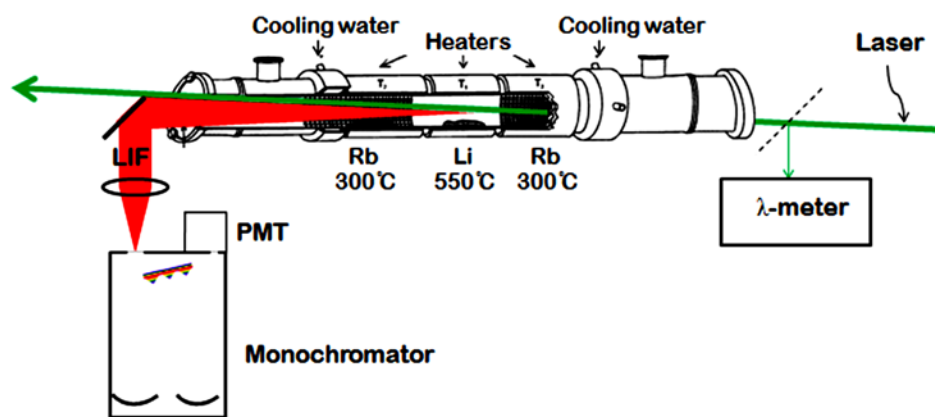


Figure 2.2. Experimental setup: LiRb molecules formed at the center of the heat-pipe-oven are excited with a laser, the LIF is collected in the forward direction and sent to a monochromator for detection.

The LiRb molecules formed in the heat pipe are distributed among different vibrational and rotational levels of the ground electronic state ($X^1\Sigma^+$ state). We excite these $X^1\Sigma^+$ state molecules to the $B^1\Pi$ state with the single mode output of a cw, frequency stabilized, ring dye laser. The ring dye laser (with Rhodamine 6G dye) is pumped with a 6 W Verdi laser (532 nm) and operates at frequencies in the range 16300–18025 cm^{-1} . As shown in Figure 2.2, we collected the laser induced fluorescence (LIF) from one end of the heat pipe oven and directed it toward a 0.75 m focal length Czerny-Turner monochromator (SPEX 1702) with a typical resolution of 3 cm^{-1} . The light is

detected at the exit slit with a photomultiplier tube module (Hamamatsu H9306-03). We have observed transitions in ${}^7\text{Li}^{85}\text{Rb}$ and ${}^7\text{Li}^{87}\text{Rb}$, but only ${}^7\text{Li}^{85}\text{Rb}$ will be considered in this thesis. We did not attempt to record transitions from ${}^6\text{Li}^{85}\text{Rb}$ and ${}^6\text{Li}^{87}\text{Rb}$ and did not observe any lines originating from Rb_2 or Li_2 in this frequency range.

We performed two types of measurements: Laser Induced Fluorescence (LIF) spectroscopy and Fluorescence Excitation Spectroscopy (FES). In the traditional LIF measurements, we kept the laser frequency fixed while scanning the monochromator and recorded the rotationally-resolved LIF spectrum (Figures 2.3 and 2.4). The LIF spectrum directly gives an estimate of the vibrational spacing for $X\ ^1\Sigma^+$ state of ${}^7\text{Li}^{85}\text{Rb}$ ($\sim 193\text{ cm}^{-1}$). For the FES measurements, we use the scheme shown in Figure 2.5 (A). We fix the monochromator to detect fluorescence at a frequency $\sim 193\text{ cm}^{-1}$ less than that of the excitation frequency, and scan the dye laser frequency to record a spectrum such as the one shown in Figure 2.5 (B). Peaks in these spectra correspond to excitation of specific ro-vibrational levels of the $B\ ^1\Pi$ state. The average accuracy of the line positions in FES is 0.02 cm^{-1} , limited by the accuracy of the wavelength-meter used for measuring the laser wavelength. We used the higher resolution FES measurements for determination of the molecular constants of both the $X\ ^1\Sigma^+$ and $B\ ^1\Pi$ states. In the following, we briefly discuss the measurements performed with LIF spectroscopy, followed by a more detailed account of the higher resolution FES measurements.

2.2 Analysis of molecular spectra

We used the LIF spectra to extract useful information about the vibrational and rotational structure of the $X\ ^1\Sigma^+$ state. We have used our LIF measurements to determine the

molecular constants of the $X^1\Sigma^+$ state, and find excellent agreement with the Fourier transform spectroscopy measurements of Ivanova *et al.*⁵⁵. As shown in Figure 2.4, we were able to record LIF up to $v'' = 45$ of the $X^1\Sigma^+$ state (covering more than 98% of the potential well depth). We observed a few weak lines near $v'' = 45$ that do not fit the LIF progression of the $X^1\Sigma^+$ state. Comparison with *ab initio* calculations indicate that these lines might be LIF to the $a^3\Sigma^+$ state, although more work is needed to confirm this. The intensity variations in the LIF spectra provide a good picture of the nodal structure in the radial wave function of the excited state, and we use these to assign the vibrational number v' of the excited $B^1\Pi$ state. In Figure 2.3 we show the LIF spectra obtained upon excitation of four different vibrational levels of the $B^1\Pi$ state. As expected from the Franck-Condon principle, the intensity distribution of LIF from $v' = 0$ has no nodes, $v' = 1$ has one node, $v' = 2$ has two nodes and so on.

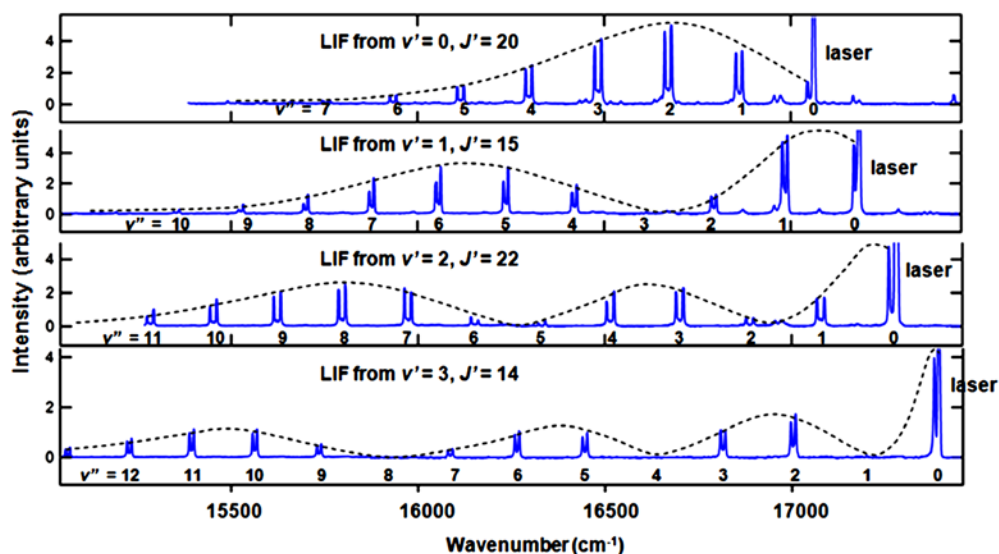


Figure 2.3. LIF spectra originating from $v' = 0, 1, 2$ and 3 levels of the $B^1\Pi$ state and terminating in different v'' levels of the $X^1\Sigma^+$ state. The intensity distribution clearly reflects the node structure of the radial wave functions of the $B^1\Pi$ state. The occurrence of P - R doublets facilitates assignment of J . The dotted lines serve to guide the eye only.

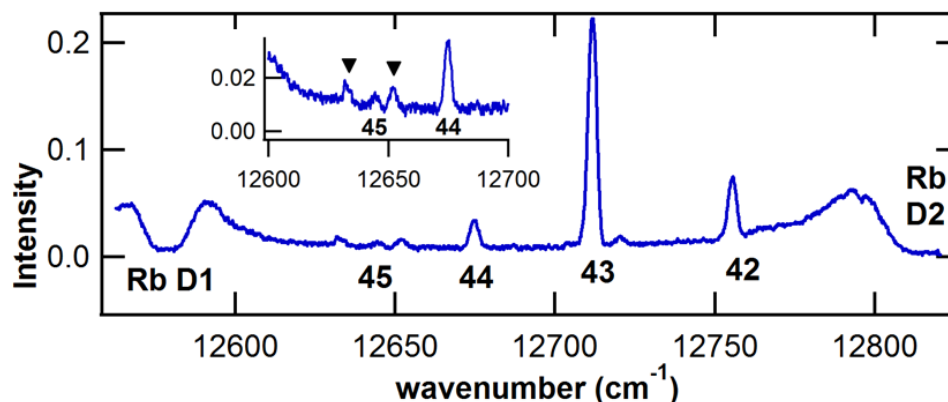


Figure 2.4. LIF after exciting the transition ($v'' = 2, J'' = 6$) \rightarrow ($v' = 20, J' = 6$) with the laser frequency at 18016.42 cm^{-1} . The LIF progression can be followed up to $v'' = 45$. The features due to self absorption of Rubidium vapor are also seen. Inset: Zoomed in view showing the highest observed v'' levels of the $X \ ^1\Sigma^+$ state along with two suspected triplet transitions (indicated by \blacktriangledown).

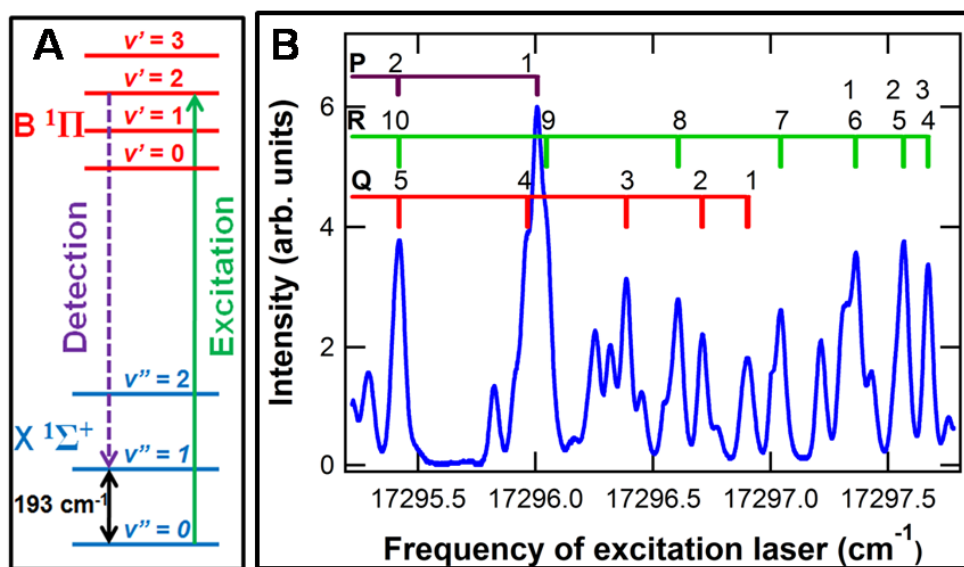


Figure 2.5. (A) Detection scheme for FES: The monochromator is fixed to detect fluorescence at a frequency $\sim 193 \text{ cm}^{-1}$ less than that of the excitation, and the laser frequency is scanned. (B) A fragment of the Fluorescence Excitation Spectrum near the ($v'' = 0, v' = 2$) band head. The rotational quantum numbers J' of the P , Q , and R branches are assigned, as indicated on the top. At our resolution, levels $R(1)$, $R(2)$ and $R(3)$ overlap with $R(6)$, $R(5)$ and $R(4)$ respectively.

Once the vibrational assignments ν' are made, we turn to FES for higher resolution measurements of the $B^1\Pi$ state. We used two modes for recording these measurements: complete spectra while tuning the laser frequency continuously in an approximately linear scan; or tuning the laser manually and recording the wavelengths and intensities of the peaks. In either case, we determine the wavelength of the laser output using a wavelength-meter (Burleigh WA-1000). In Figure 2.5B we show an example of the Fluorescence Excitation Spectra around the head of the ($\nu''=0$, $\nu'=2$) band, obtained by patching together several frequency scans (~ 13 GHz each). Assignments of several rotational lines belonging to the P , Q and R branches are indicated. We recorded similar high resolution FES for 27 different (ν'' , ν') bands of the $X^1\Sigma^+ \rightarrow B^1\Pi$ transition, where ν'' ranged from 0–2 and ν' ranged from 0–20. For each of these vibrational bands we observed the Q branch rotational levels and assigned lines up to $J \sim 20$. We did not attempt to study the higher J levels because our ultimate goal is to study the formation of ultracold molecules via photoassociation, where only $J < 4$ levels are generally observed. We assigned the P and R branches (e parity levels⁶⁴) only up to $\nu' = 3$. We show plots of all observed Q branch transition frequencies, against $J(J+1)$ in Figure A1 of Appendix A. A list of all observed transitions is also available in Table A1 of Appendix A. The analysis which follows is based on these high resolution FES measurements.

2.3 Molecular constants of $^7\text{Li}^{85}\text{Rb}$

We determine the molecular constants in a level-by-level manner rather than using a global fit. The total energy $E_{\nu,J}$ of a given (ν , J) level is expressed in the form²²:

$$E_{\nu,J} = T_{\nu} + F_{\nu}(J) \quad (2.1)$$

$F_v(J)$ is the rotational energy and T_v is the rotation-less energy for the vibrational state v ,

$$T_v = T_e + G_v \quad (2.2)$$

where T_e is the minimum of the corresponding electronic potential energy curve, and G_v is the vibrational energy. As is commonly done²², we approximate the value of the vibrational energy G_v as an anharmonic oscillator and rotational energy $F_v(J)$ as a vibrating rotor:

$$G_v = \omega_e(v + 1/2) - \omega_e x_e(v + 1/2)^2 + \omega_e y_e(v + 1/2)^3 + \dots \quad (2.3)$$

$$F_v(J) = B_v[J(J+1) - \Lambda^2] - D_v[J(J+1) - \Lambda^2]^2 \quad (2.4)$$

where Λ^2 is 0 for the $X^1\Sigma^+$ state and 1 for the $B^1\Pi$ state, B_v is the rotational constant, D_v is the centrifugal distortion constant, ω_e is the harmonic constant while $\omega_e x_e$, $\omega_e y_e$ etc. are the anharmonic constants. Also, to a first approximation, the rotational constant B_v is given by

$$B_v = B_e - \alpha_e(v + 1/2) \quad (2.5)$$

For each vibrational level v'' from 0 to 2 of the $X^1\Sigma^+$ state, we measure the difference in energy of the P and R lines using FES:

$$E_{v'',J''+1} - E_{v'',J''-1} \equiv \Delta_2 F_{v''}(J'') = (4J''+2)B_{v''} - 2(4J''+2)D_{v''} \quad (2.6)$$

We determine the constants $B_{v''}$ and $D_{v''}$ from a least squares fit of $\Delta_2 F_{v''}(J'')$ vs. J'' (Figure 2.6 (A)) and list the values of $B_{v''}$ in Table 2.1. We obtain $B_{e''} = 0.21661(7)$ and $\alpha_{e''} = 0.001575(4)$, from a fit of the data to equation (2.5); these values are in good agreement with the higher precision results of Ivanova *et al.*⁵⁵. The uncertainties in the values of $B_{v''}$ obtained from the fit of $\Delta_2 F_{v''}(J'')$ vs. J'' are $<0.025\%$. The relative uncertainties of the values of $D_{v''}$ is much larger, $\sim 25\%$, due in part to the focus of our measurements on

low- J states. In light of this uncertainty, we neglect the variation of $D_{v''}$ with v'' , and we report only an average value $D_{e''} = 1.26(10) \times 10^{-6} \text{ cm}^{-1}$. This value is also in reasonable agreement with $D_{e''} = 1.062 \times 10^{-6} \text{ cm}^{-1}$ reported in ref. 55, as well as the Kratzer relation for the Morse potential approximation: $D_{e''} = 4B_{e''}^3/\omega_{e''}^2 = 1.065 \times 10^{-6} \text{ cm}^{-1}$, using $B_{e''}$ and $\omega_{e''}$ from ref. 55. For determination of all the other constants for the $X^1\Sigma^+$ and $B^1\Pi$ states, we restrict our analysis to the Q branch transitions only.

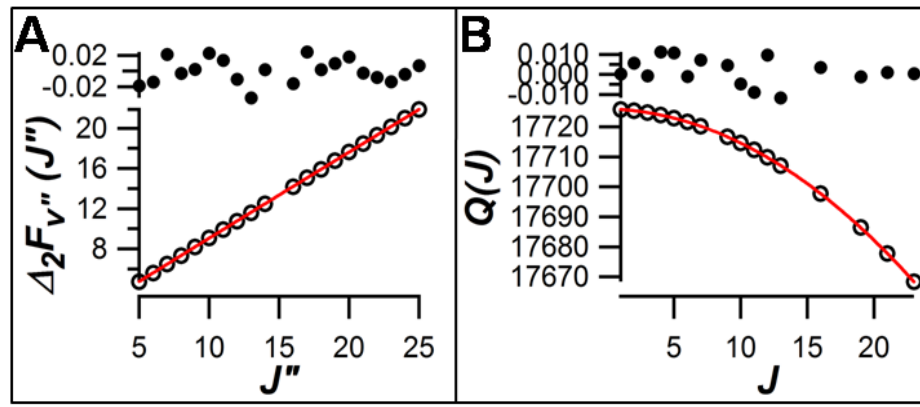


Figure 2.6. (A) A plot (open circles \circ) of $\Delta_2 F_{v''}(J'')$, in cm^{-1} , for the $v'' = 0$ level of the $X^1\Sigma^+$ state. The solid line (red) is a fit to equation (2.6) and the filled circles (\bullet) are the fit residuals. $B_{v''}$ and $D_{v''}$ for the $v'' = 0$ level are obtained from this plot. The excited state involved was the $v' = 2$ level of the $B^1\Pi$ state. (B) A plot (open circles \circ) of $Q(J)$, in cm^{-1} , for transitions from $v'' = 2$ to $v' = 13$. We obtain the values of $B_{v'=13}$, $D_{v'=13}$ and $(T_{v'=13} - T_{v'=2})$ from this plot. Similar plots are made for the Q -lines of other (v'', v') transitions and the respective $B_{v'}$, $D_{v'}$ and $(T_{v'} - T_{v''})$ are obtained.

The energy $Q(J)$ of an absorption line corresponding to a $X^1\Sigma^+(v'', J) \rightarrow B^1\Pi(v', J)$ transition is

$$Q(J) = E_{v', J} - E_{v'', J} \\ = (T_{v'} - T_{v''}) + B_{v'}[J(J+1) - 1] - D_{v'}[J(J+1) - 1]^2 - B_{v''}J(J+1) + D_{v''}J^2(J+1)^2 \quad (2.7)$$

With the values of $B_{v''}$ held fixed at the values reported in Table 2.1 and $D_{v''}$ held fixed at $1.06 \times 10^{-6} \text{ cm}^{-1}$, we obtain the values of $B_{v'}$, $D_{v'}$ and $(T_{v'} - T_{v''})$ from a least squares fit of

$Q(J)$ vs. J (Figure 2.6. (B)). We obtain $T_{v''=1} - T_{v''=0}$ from the difference in frequencies between the following rotation-less transitions: $X^1\Sigma^+ (v''=1, J=0) \rightarrow B^1\Pi (v', J=0)$ and $X^1\Sigma^+ (v''=0, J=0) \rightarrow B^1\Pi (v', J=0)$. $T_{v''=2} - T_{v''=0}$ is calculated in a similar manner. $T_{v'}$ is then evaluated from the $(T_{v'} - T_{v''})$ values obtained above. In Table 2.1, we report the values of T_v , B_v and D_v for both $X^1\Sigma^+$ and $B^1\Pi$ states.

The energy differences $T_{v''=1} - T_{v''=0}$ and $T_{v''=2} - T_{v''=1}$ that we measure are in excellent agreement with those derived using the spectroscopic constants reported by Ivanova *et al.*⁵⁵. From a fit of $T_{v'}$ to equations (2.2–2.3), we extract: $T_{e'}(B^1\Pi) = 17110.0(5) \text{ cm}^{-1}$ and $\omega_{e'} = 122.3(3) \text{ cm}^{-1}$ in agreement with experimental values reported in ref. 56. Corresponding theoretical values from Korek *et al.*⁵⁹ are $T_{e'}(B^1\Pi) = 17205 \text{ cm}^{-1}$ and $\omega_{e'} = 140.5 \text{ cm}^{-1}$. We do not make explicit comparisons to ref. 60 calculations, which included spin-orbit effects, because these results are expected to be more precise only for larger internuclear spacings.

We calculate the dissociation energy $D_e(B^1\Pi)$ of the $B^1\Pi$ state using the standard relation:

$$D_e(B^1\Pi) = D_e(X^1\Sigma^+) + \Delta E[Rb(5^2P_{3/2}) - Rb(5^2S_{1/2})] - T_{e'}(B^1\Pi)$$

where $D_e(X^1\Sigma^+) = 5927.9(40) \text{ cm}^{-1}$ is the dissociation energy of the $X^1\Sigma^+$ state as reported in ref. 55, $\Delta E[Rb(5^2P_{3/2}) - Rb(5^2S_{1/2})] = 12816.6 \text{ cm}^{-1}$ is known very precisely from standard databases and $T_{e'}(B^1\Pi) = 17110.0(5) \text{ cm}^{-1}$. Using these values we obtain the value of $D_e(B^1\Pi)$ to be $1634.5(45) \text{ cm}^{-1}$, where the major source of error arises from the uncertainty in the value of $D_e(X^1\Sigma^+)$.

Table 2.1 Molecular constants (in cm^{-1}) of the $X \ ^1\Sigma^+$ state and f -parity levels of the $B \ ^1\Pi$ state. All values of T_v are referenced to $T_{v''=0} = 0$. The value of $D_{v''}$ is held fixed at $1.06 \times 10^{-6} \text{ cm}^{-1}$. These constants reproduce the observed transition frequencies with an accuracy of 0.02 cm^{-1} .

v	$T_v - T_{v''=0}$	B_v	$D_v \times 10^6$
X $^1\Sigma^+$ state			
0	0	0.21580 (3)	(fixed at
1	192.96	0.21430 (5)	1.06)
2	383.70	0.21265 (5)	
B $^1\Pi$ state, f -levels			
0	17073.07	0.17146(4)	1.6(1)
1	17188.52	0.16703(4)	1.2(1)
2	17297.15	0.16261(2)	1.78(5)
3	17398.94	0.15768(4)	2.00(8)
4	17493.91	0.15226(6)	1.7(2)
5	17582.27	0.14717(2)	2.17(5)
6	17664.54	0.14194(3)	2.42(6)
7	17741.20	0.13696(8)	3.4(4)
8	17812.80	0.13135(4)	2.07(7)
9	17879.80	0.12660(8)	2.2(2)
10	17942.64	0.12191(5)	2.2(1)
11	18001.73	0.11743(3)	2.29(6)
12	18057.37	0.11301(6)	2.2(2)
13	18109.83	0.10907(2)	2.61(5)
14	18159.37	0.10488(4)	2.35(9)
15	18206.18	0.10113(6)	2.7(1)
16	18250.29	0.09738(10)	1.7(4)
17	18292.46	0.09364(13)	1.9(5)
18	18332.24	0.09026(1)	2.09(3)
19	18369.95	0.08696(3)	2.33(4)
20	18405.63	0.08349(3)	2.31(6)

2.4 Perturbations in the molecular spectra

In our FES measurements, we also observed rotational perturbations in the e parity levels of the $B^1\Pi$ state. For transitions to $v' = 1, 2$ and 3 , the perturbations manifested through irregularities in transition frequencies for both P and R branches. The perturbations must be in the $B^1\Pi$ state because the $X^1\Sigma^+$, being far from any other electronic potential, is expected to be unperturbed. This was verified using the energy splitting $\Delta_2 F_{v''}(J'')$ of the $X^1\Sigma^+$ state, which did not have any irregularities (Figure 2.6 (A)). We did not observe any such irregularity in the $v' = 0$ level. Figure 2.7 shows, for the ($v''=0, v'=1$), ($v''=0, v'=2$) and ($v''=0, v'=3$) bands, the difference between observed and calculated line positions (calculated using $B_{v'}$ and $D_{v'}$ values obtained above from f parity levels, i.e. Q branch, only). The maximum perturbation occurs at $J' \sim 8$ for $v' = 1$, at $J' \sim 16$ for $v' = 2$ and at $J' \sim 30$ for $v' = 2$. Since the f parity levels (Q branch) are not perturbed, it can be concluded that the perturbing state is a $^1\Sigma^+$ state and not a $^1\Pi$ state^{22,65}. From the *ab initio* calculations of potential energy curves, we expect that $C^1\Sigma^+$ state is the perturbing state.

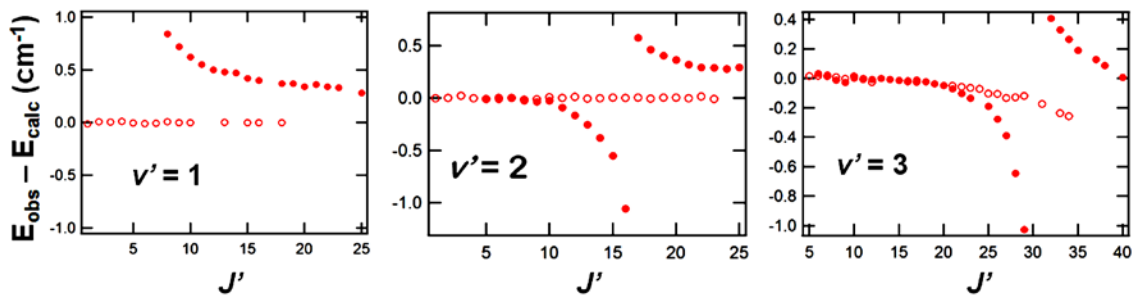


Figure 2.7. The difference between observed and calculated transition frequencies in the ($v''=0, v'=1$), ($v''=0, v'=2$) and ($v''=0, v'=3$) bands of the $X^1\Sigma^+ \rightarrow B^1\Pi$ system. Open circles (\circ) correspond to f parity levels and filled circles (\bullet) correspond to e parity levels. The f parity levels are not perturbed while rotational perturbations are maximum near specific J' values for the e parity levels of the $B^1\Pi$ state.

The perturbation matrix element can be written as⁶⁵:

$$H_{\Pi\Sigma}(v_{\Pi}, v_{\Sigma}, J) = \eta(v_{\Pi}, v_{\Sigma}) \sqrt{J(J+1)} \quad (2.8)$$

where $\eta(v_{\Pi}, v_{\Sigma})$ is a constant that depends on vibrational levels of the $B^1\Pi$ and $C^1\Sigma^+$ state. The (observed) perturbed energy levels $E_{\Pi}(v_{\Pi}, J)$ of the $B^1\Pi$ state is related to the unperturbed energy levels $E_{\Pi}^0(v_{\Pi}, J)$ and $E_{\Sigma}^0(v_{\Sigma}, J)$ of the $B^1\Pi$ and $C^1\Sigma^+$ states through⁶⁵:

$$E_{\Pi}(v_{\Pi}, J) = \frac{E_{\Pi}^0(v_{\Pi}, J) + E_{\Sigma}^0(v_{\Sigma}, J)}{2} \pm \sqrt{\frac{[E_{\Pi}^0(v_{\Pi}, J) + E_{\Sigma}^0(v_{\Sigma}, J)]^2}{4} + H_{\Pi\Sigma}(v_{\Pi}, v_{\Sigma}, J)^2} \quad (2.9)$$

where the + and – signs refer to J levels above and below the perturbation center. $E_{\Pi}^0(v_{\Pi}, J)$ is calculated using the Q branch data and $E_{\Sigma}^0(v_{\Sigma}, J) = T_{\Sigma}^0(v_{\Sigma}) + B_{\Sigma}(v_{\Sigma})[J(J+1)]$, where $T_{\Sigma}^0(v_{\Sigma})$ and $B_{\Sigma}(v_{\Sigma})$ respectively are the rotationless energy and rotational constant of the v_{Σ} vibrational level of the $C^1\Sigma^+$ state. The values of $T_{\Sigma}^0(v_{\Sigma})$, $B_{\Sigma}(v_{\Sigma})$ and $\eta(v_{\Pi}, v_{\Sigma})$ are extracted from a fit to equation (2.9) and are reported in Table 2.2. We also derive $T_e(C^1\Sigma^+) = 17231(2) \text{ cm}^{-1}$ and $\omega_e(C^1\Sigma^+) = 112.5(5) \text{ cm}^{-1}$ in reasonable agreement with a more recent report⁵⁶. The theoretical potential energy curves also allow us to determine that the $v_{\Pi} = 1, 2$ and 3 levels of the $B^1\Pi$ state are perturbed by the $v_{\Sigma} = 0, 1$ and 2 levels of the $C^1\Sigma^+$ state, respectively. In chapter 6, we discuss a PA scheme based on the $C^1\Sigma^+$ state.

Table 2.2. The rotationless energy $T_{\Sigma}^0(v_{\Sigma})$ (referenced to $T_{v''=0} = 0$), rotational constant $B_{\Sigma}(v_{\Sigma})$ and the perturbation matrix element $\eta(v_{\Pi}, v_{\Sigma})$ of the $C^1\Sigma^+$ state.

v_{Σ}	$T_{\Sigma}^0(v_{\Sigma})$ in cm^{-1}	$B_{\Sigma}(v_{\Sigma})$ in cm^{-1}	$\eta(v_{\Pi}, v_{\Sigma})$ in cm^{-1}
0	17190.13(05)	0.1469(11)	$\eta(1,0) = 0.0761(27)$
1	17302.58(69)	0.1396(22)	$\eta(2,1) = 0.0455(41)$
2	17406.47(64)	0.1463(07)	$\eta(3,2) = 0.0135(14)$

2.5 Implications and predictions

To conclude the chapter, I will discuss the implications of our measurements in finding efficient photoassociation pathways for the production of ultracold ground state LiRb molecules, and their detection via state selective ionization. We first look back at the relative intensity of the LIF lines in Figure 2.3. The line originating from $v' = 2$ or $v' = 3$ and terminating in $v'' = 0$ has much higher intensity than those terminating in $v'' > 0$. This implies that the Franck Condon factor is very high for the $X^1\Sigma^+(v'' = 0) \leftarrow B^1\Pi(v' = 2)$ and $X^1\Sigma^+(v'' = 0) \leftarrow B^1\Pi(v' = 3)$ transitions. A rough estimate based on the relative intensity of the LIF peaks shows that approximately 22% of the molecules in the $v' = 2$ decay back to $v'' = 0$ and approximately 25% of the molecules in $v' = 3$ states decay back to $v'' = 0$. The estimate based on calculation of Franck-Condon factors from an RKR potential predicts approximately 22% of the molecules in $v' = 2$ and $v' = 3$ levels decay back to $v'' = 0$, in agreement with the experiment. This is encouraging for formation of ultracold ground state molecules via photoassociation into the $B^1\Pi(v' = 2)$ or $B^1\Pi(v' = 3)$ state followed by spontaneous emission to the ground $X^1\Sigma^+(v'' = 0)$ state. A similar scheme was used for producing ultracold LiCs molecules^{61,62}. In particular, $B^1\Pi(v' = 2)$ could be an excellent state for such a scheme, especially if there is a significant increase in the photoassociation efficiency due to wave function overlap between the $X^1\Sigma^+$ and $a^3\Sigma^+$ states near the inner turning point of the $a^3\Sigma^+$ state. In the absence of such overlap, the recently proposed scheme based on photoassociation near a Feshbach resonance^{66,67} could be used to form ultracold LiRb molecules in the ground $X^1\Sigma^+(v'' = 0)$ state. It is also clear that the $B^1\Pi(v' = 2)$ or $B^1\Pi(v' = 3)$ state would be a good intermediate state

for state selective detection of ultracold ground state LiRb molecules through Resonance Enhanced Multi Photon Ionization (REMPI).

2.6 Work in progress

LiRb is a molecule for which very little spectroscopic data is available. It is thus important not to discard any information and to analyze the data in every possible way. In deriving the molecular constants we have mostly relied on the transition frequencies and not on the transition strengths. We want to carefully examine the information encoded in the intensity of lines in Laser Induced Fluorescence (LIF) spectroscopy. Frequency resolved LIF spectroscopy is generally used to determine the potential of electronic ground state of molecules to which the molecules decay upon excitation with a laser and the analysis is based on transition frequencies (not intensities). The potential of the electronic excited state is seldom determined from LIF spectroscopy. We plan to use the information encoded in the intensities of the fluorescence lines in addition to their frequencies, thus making the experiment two dimensional, to extract the excited and ground electronic states of the LiRb molecule. We are collaborating with Dr. Xuan Li and Prof. Moshe Shapiro from the University of British Columbia, who have developed a theoretical technique which can accurately determine potential energy curves from 2D-LIF spectroscopy. Using their method, the transition dipole moment as a function of inter-nuclear displacement can also be extracted^{68,69}.

CHAPTER 3. THE APPARATUS FOR PRODUCING COLD MOLECULES

In this chapter I will describe the apparatus⁷⁰ used to produce ultracold LiRb molecules. The apparatus consists of a dual-species magneto-optical trap (MOT) for simultaneous cooling and trapping of ^7Li and ^{85}Rb . I will describe the laser system for the MOT and the vacuum chamber which includes a Zeeman slower for ^7Li and a Time of Flight (TOF) Mass Spectrometer (MS).

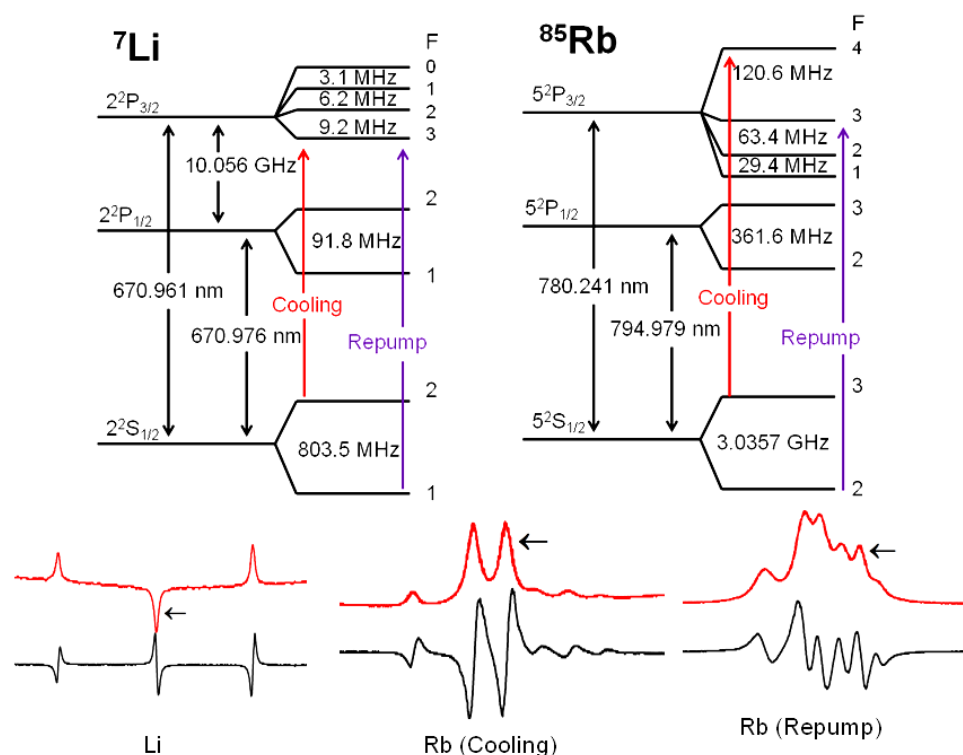


Figure 3.1. Energy level diagram for ^7Li and ^{85}Rb . Lower panels: The saturated absorption signal (red line) and the error signal (black line). The laser frequencies decrease on moving from left to right. The arrows indicate the peaks to which the respective lasers are locked.

3.1 Light sources for the MOT

The energy level diagram relevant for cooling and trapping of ${}^7\text{Li}$ and ${}^{85}\text{Rb}$ is shown in Figure 3.1 and a schematic representation of the laser system is shown in Figure 3.2.

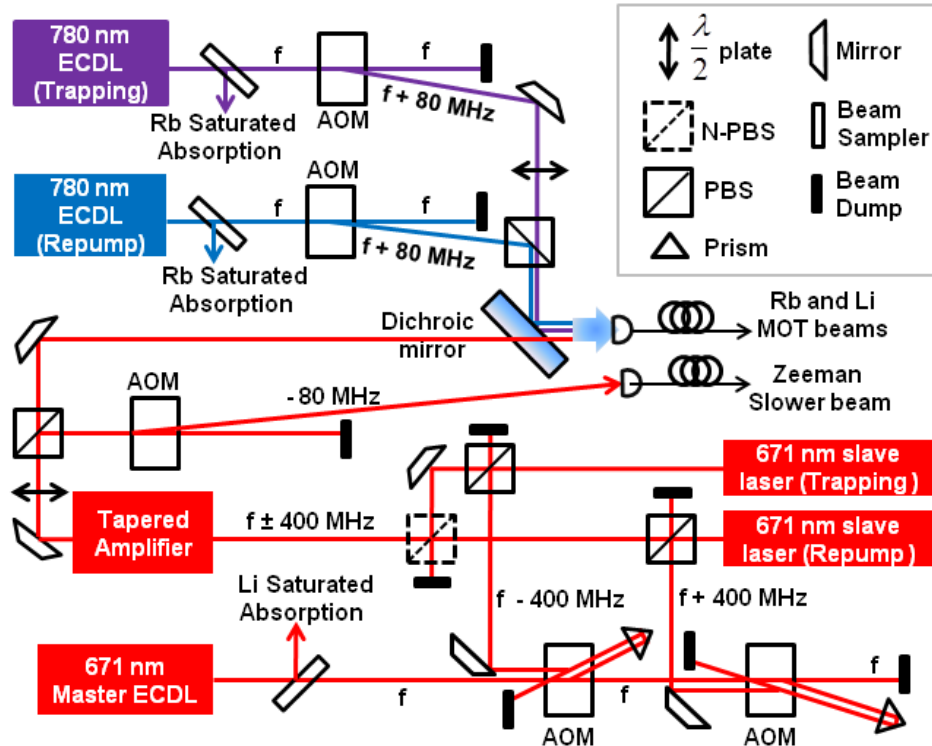


Figure 3.2. Schematics of the laser system for our ${}^7\text{Li}$ - ${}^{85}\text{Rb}$ dual species magneto-optical trap (MOT). For the AOMs in double pass configuration, right angled prisms are used to vertically displace the beams. The beams coming out of the two slave lasers are combined on an N-PBS instead of a PBS because the tapered amplifier can amplify light of only one polarization. Note that the cooling and repumping beams for both ${}^7\text{Li}$ and ${}^{85}\text{Rb}$ MOTs are combined and sent to the experiment through the same optical fiber.

To drive transitions between the $5s\ {}^2S_{1/2}$ and $5p\ {}^2P_{3/2}$ states, the ${}^{85}\text{Rb}$ MOT requires two lasers with wavelength near 780 nm: a cooling laser and a repumping laser, differing in frequency by the ground state hyperfine splitting (~ 3.036 GHz). The cooling laser is a commercial high power ($\sim 1\text{W}$) external cavity diode laser (ECDL) from Sacher

Lasertechnik. The repumping laser is a homebuilt ECDL in a Littrow configuration with an output power of around 50 mW⁷¹. Frequency stabilization of both lasers is obtained by locking the laser frequency using the standard saturated absorption spectroscopy technique. The cooling laser is locked to the $F = 3 \rightarrow F' = 2-4$ crossover resonance. The frequency is then up-shifted by 68 MHz using an acousto-optic modulator (AOM) in a single pass configuration, which makes the cooling laser frequency detuned by $\delta_{\text{Rb}} = -24$ MHz from the $F = 3 \rightarrow F' = 4$ cycling transition. The homebuilt repumping laser is locked to $F = 2 \rightarrow F' = 1-2$ crossover resonance. The frequency is then up-shifted by 78 MHz using another AOM in a single pass configuration, which makes the repumping laser resonant with the $F = 2 \rightarrow F' = 3$ transition. The repumping light is combined with the cooling light on a polarizing beam splitter (PBS). Both beams are then sent to a dichroic mirror where they are combined with the 671 nm light for the ${}^7\text{Li}$ MOT.

To drive transitions between the $2s \ {}^2S_{1/2}$ and $2p \ {}^2P_{3/2}$ states, the ${}^7\text{Li}$ MOT also requires light at two frequencies, for the cooling and repumping transitions, separated by the ${}^7\text{Li}$ ground state hyperfine splitting of ~ 803.5 MHz. The Lithium laser system is based on a master-slave injection scheme. We use a commercial ECDL (Toptica DLPro) as our master laser with ~ 20 mW output power at 670.96 nm. The master laser is locked to the $F = 1-2 \rightarrow F'$ crossover resonance in the saturated absorption spectra of ${}^7\text{Li}$ (note that the hyperfine levels in the $2p \ {}^2P_{3/2}$ state of ${}^7\text{Li}$ are not well resolved). To generate the frequency at the cooling (repumping) $F = 2 \rightarrow F' = 3$ ($F = 1 \rightarrow F' = 2$) transition, a part of the light from the master laser is down-shifted (up-shifted) in frequency by ~ 400 MHz using a 200 MHz AOM in a double pass configuration. The down-shifted and up-shifted beams are used to injection lock two free running laser diodes, each producing ~ 20 mW

of light at the frequency of the respective transitions. We control the detuning of the cooling and repumping beams using their respective AOMs. The outputs from the two injection locked lasers are combined on a non-polarizing beam splitter (N-PBS). The ratio of power between the cooling and repumping light is controlled by suitably placed half-wave plates and polarizing beam splitters (PBS) before the beams are combined on the N-PBS. The combined light, containing both cooling and repumping frequencies, is injected into a commercial tapered amplifier (Toptica BoosTA), which produces up to 270 mW of light. The spectral content of the tapered amplifier output is checked with a scanning Fabry-Perot interferometer with free spectral range of 2 GHz. We adjust the injected power such that the height of the transmission peak at the cooling frequency is twice that at the repumping frequency. This determines the ratio, 2:1, between the powers in the cooling and repumping frequencies with the ratio fixed for the experiments reported here. The light from the tapered amplifier is divided into two parts. The major part (~180 mW) is sent to a dichroic mirror where it is combined with the 780 nm light. The beams for the two MOTs are coupled into the same polarization maintaining optical fiber, which greatly simplifies the optical set up near the vacuum chamber. We typically get around 50% coupling efficiency for both the 671 nm and 780 nm beams, yielding up to 90 mW of light at 671 nm and up to 300 mW of light at 780 nm. The other part of the 671 nm light from the tapered amplifier, comprised of both cooling and repumping frequencies, is down-shifted in frequency by 80 MHz using an AOM to provide the light for the Li Zeeman slower. After coupling into a polarization maintaining optical fiber, the maximum power available for the Zeeman slower beam is ~ 30 mW. Note that this total

power in the Zeeman slower beam is also distributed between two frequencies. In the rest of the article we often drop the superscripts and denote ${}^7\text{Li}$ with Li and ${}^{85}\text{Rb}$ with Rb.

We later replaced the master-slave injection locking scheme with a simpler scheme based on an electro-optic modulator (EOM). The light from the master laser is directly injected into the tapered amplifier producing ~ 300 mW of light at 670.96 nm. A small fraction of this light is picked off, up-shifted by ~ 400 MHz with an AOM and is used to lock to the $F = 1-2 \rightarrow F'$ crossover resonance in the saturated absorption spectra of ${}^7\text{Li}$. The rest of the light is passed through an EOM to put ~ 800 MHz frequency sidebands, the power in each sideband being half that of the carrier. The exact AOM and EOM frequencies are chosen such that carrier and the upper sidebands have the right frequencies for the cooling and repumping transitions respectively. The experiments reported in chapter 4 onwards are done with this new set up.

3.2 The vacuum chamber

We show a schematic diagram of the entire vacuum chamber in Figure 3.3. The vacuum chamber consists of three main sections: the Lithium oven, the Zeeman slower for Li atoms and the ultra high vacuum (UHV) experimental chamber.

The lithium (Li) oven chamber (Figure 3.4A) produces a collimated beam of Li atoms travelling toward the UHV chamber via the Zeeman slower section. It consists of a Li oven containing approximately 10g of lithium (natural abundance, $\sim 92\%$ ${}^7\text{Li}$) which is heated to $\sim 400^\circ\text{C}$ resulting in a lithium vapor pressure of 10^{-4} Torr. The hot vapor escapes the oven through a nozzle (diameter = 8 mm), which is kept at a slightly higher temperature of $\sim 415^\circ\text{C}$ to avoid condensation of Li. As shown in Figure 3.4B, the nozzle

consists of a stack of approximately 60 hypodermic needles, each with an inner diameter of 0.8 mm and length of 10 mm. The hypodermic needles improve the collimation of the atomic beam by reducing the emission angle to $\sim 4.5^\circ$.

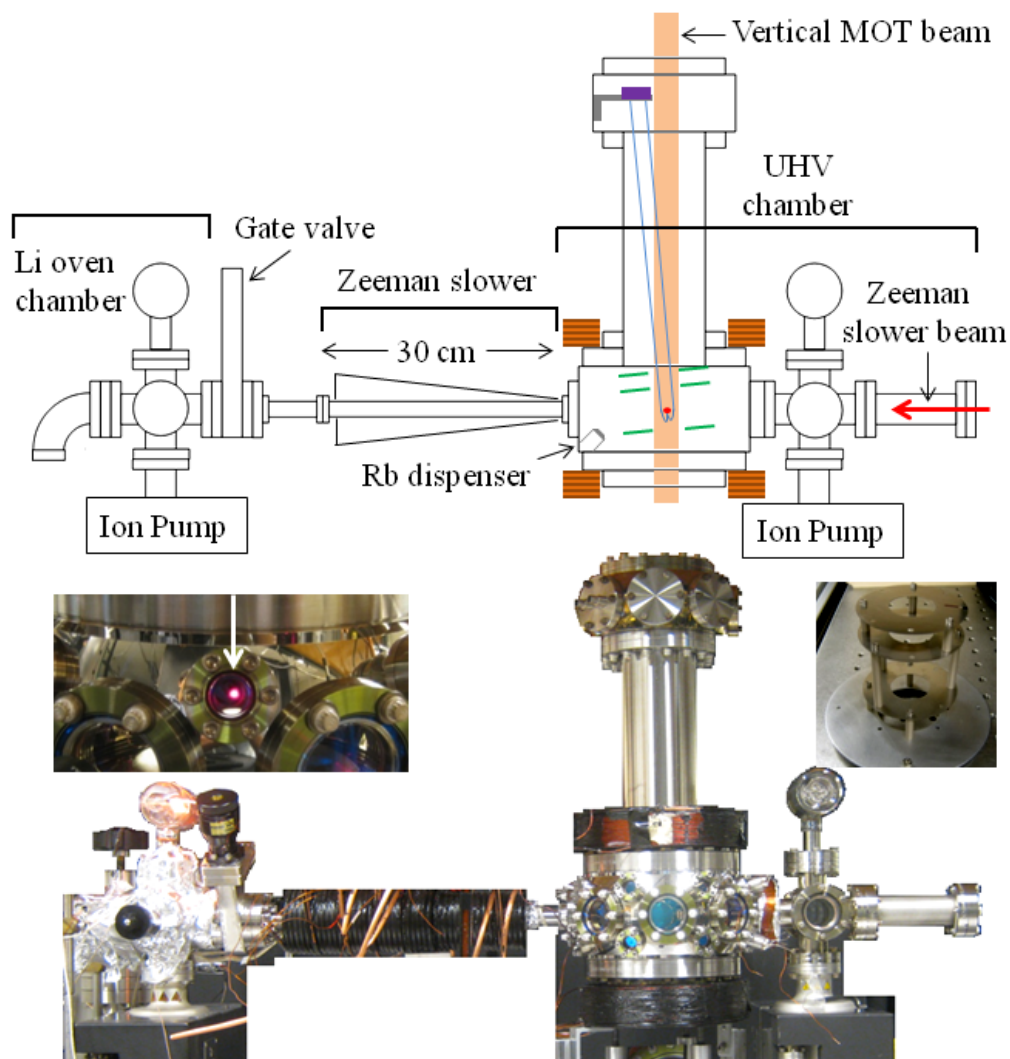


Figure 3.3. Schematic representation of the vacuum chamber (top) along with a photograph (bottom). The picture was taken before the MOT optics was mounted. The red dot at the center of the UHV chamber represents the MOT. The green lines denote the electric field plates (picture in right inset) which accelerate the ions produced during REMPI towards the MCP, denoted in purple. The trajectory of ions is indicated by the blue lines. The MOT coils are denoted in orange. Left inset: Photograph of the ^7Li MOT (indicated by the arrow).

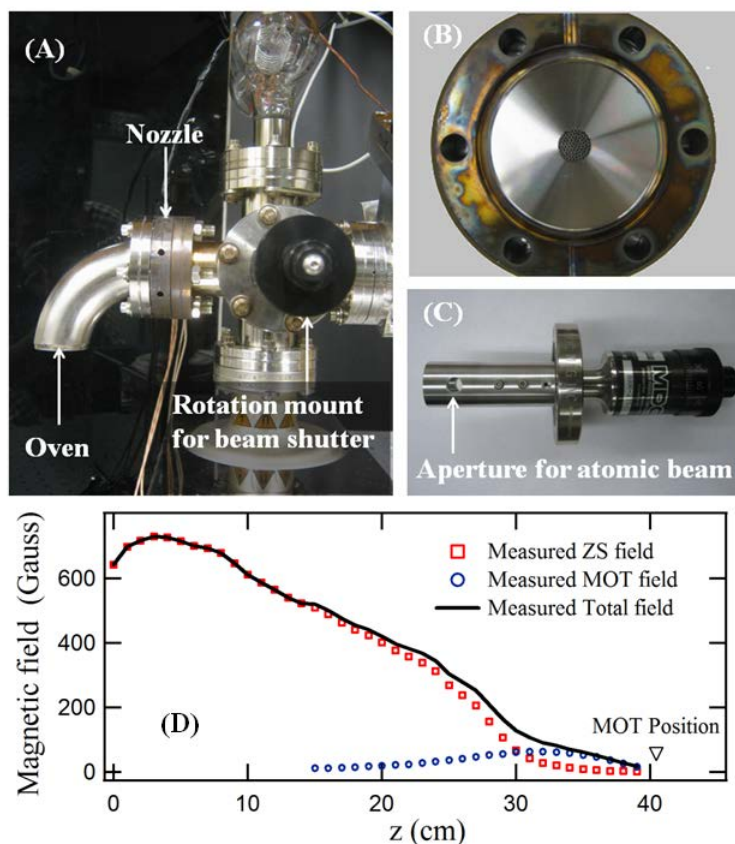


Figure 3.4. (A) Photograph of the lithium oven chamber showing the oven, the nozzle and the rotation mount on which the hollow cylindrical beam shutter is mounted (see text for details). (B) Photograph of the nozzle before integration into the vacuum chamber. The stacked hypodermic needles in the central aperture are also visible. (C) Photograph of the atomic beam shutter mounted on a rotation mount. The atom beam is blocked or transmitted depending on the orientation of the aperture. (D) Magnetic field profile of the Zeeman Slower (ZS) solenoid (squares), MOT coils (circles) and their combined magnetic field (solid line).

The atomic beam is further collimated by an aperture of 8 mm diameter placed approximately 80 mm downstream from the nozzle. As shown in Figure 3.4C, the aperture is formed by two holes on a hollow cylinder mounted on a vacuum rotation feedthrough. In addition to its role in improving the beam collimation (when the aperture

faces the atomic beam), it serves as a beam shutter, completely blocking the atomic beam when the aperture is perpendicular to the atomic beam. In addition, it can also control (reduce) the atomic flux by appropriate rotation of the hollow cylinder. The collimated Li beam then enters the Zeeman slower section after passing through a gate valve. The oven chamber is pumped by a Varian Starcell Ion pump with a pumping speed of 40 l/s. To protect the gate valve from direct contact with lithium atoms, the copper gasket forming the vacuum seal is slightly unconventional. Instead of the standard copper gaskets, a blank copper gasket is modified to include a small through hole of 8 mm diameter at the center. This hole also provides additional collimation to the lithium beam and reduces the conductance between the oven chamber and the Zeeman slower section. The thermal lithium atoms emanating from the oven chamber are slowed by the Zeeman slower.

The design of our Zeeman slower is similar to that of Selim Jochim's group at University of Heidelberg⁷². The net magnetic field is the sum of the magnetic field produced by the 8-section Zeeman slower solenoid with variable number of turns and by the MOT coils. The Zeeman slower is in a decreasing field configuration with maximum magnetic field near the Li oven and decreasing to zero near the MOT. We show the magnetic field of the Zeeman slower along its axis in Figure 3.4D when a current of 7 A is passed through the coils (However, we typically operate the coils at 4.5 A in order to avoid overheating of the coils. This is enough to trap 2×10^8 Li atoms). The 12" long tube of the Zeeman slower has an inner diameter of only 0.75" resulting in a low conductance between the oven chamber and the UHV experimental chamber. We estimate that the low conductance helps maintain the UHV chamber at a pressure 50 times lower than the oven chamber.

The UHV experimental chamber (Figure 3.3) is the heart of the experiment and is designed to produce and detect ultracold atoms and molecules. The pressure in the UHV experimental chamber is less than the lowest pressure, 4×10^{-10} Torr, measurable by the ion gauge. As shown in Figure 3.3, the UHV chamber consists of an extended 8" spherical octagon (Kimball Physics MCF800-ExtOct-G2C8A16), a 10.6" long CF 6" nipple and a 6" spherical octagon (Kimball Physics MCF600-SphOct-F2C8) on the top. The extended 8" spherical octagon has two CF 8" viewports, eight CF 2.75" viewports and sixteen CF 1.33" viewports. This allows for excellent optical access. The two CF 8" viewports are used for the vertical MOT beams. Four of the CF 2.75" viewports are used for the horizontal MOT beams, two are used for fluorescence imaging, one connects to the Zeeman slower section and the last connects to a six-way cross. The arms of the six-way cross are connected to a Varian Starcell Ion pump, an ion gauge and a sapphire window through which the laser beam for the Zeeman slower enters. All other viewports are standard Kodial glass viewports (Kurt J. Lesker) which were broadband anti-reflection coated for the 650-1100 nm region by Abrisa Technologies. Ten out of the sixteen CF 1.33" viewports have optical viewports, two have electrical feedthroughs while the rest are blanked off. The Rb MOT is loaded from a Rb dispenser (SAES Getters) located approximately 6 cm from the MOT. The Rb dispenser is typically operated by running a current of 3.3 A. The pressure of the UHV chamber increases to $\sim 3 \times 10^{-9}$ Torr when the Rb dispenser is in operation (with a second bake-out performed after a year of operation, the pressure dropped and stayed below 5×10^{-10} Torr even when the Rb dispensers were in operation).

The apparatus is designed to produce ultracold LiRb molecules in their ro-vibrational ground state. The LiRb molecules formed in our experiments will be detected using Resonance Enhanced Multi Photon Ionization (REMPI). Details of REMPI will be discussed in the theses of Adeel Altaf and John Lorenz, and similar schemes have also been discussed elsewhere⁷³. However, to complete the description of the apparatus we describe the Time of Flight (TOF) Mass Spectrometer^{74,75} installed inside the UHV chamber which will be used to detect and image the ions formed during REMPI. A relatively new feature of our apparatus is the ability to detect the orientation of the LiRb molecules. This will be achieved using the technique of Velocity Mass Imaging (VMI)⁷⁶. We integrate the TOF MS and VMI into one compact set-up. The spectrometer consists of three regions: acceleration, TOF and detection. The acceleration region consists of three stainless steel electric field plates. The electric field plates are 250 μm thick, have an outer diameter of 75 mm and a central hole of 32 mm. The central holes allow the vertical MOT beams to pass through. The lower (repeller) plate and the middle (extractor) plate are spaced by 47 mm, with the MOT located at the center. The middle (extractor) and the upper (ground) plates are 20 mm apart. PEEK rods are used as spacers as and where needed.

Ions are created by ionizing the atoms or molecules in the MOT region by a Nd:YAG pumped pulsed dye laser with a pulse width of ~ 10 ns and a repetition rate of 10 Hz. The ions of different species (Li^+ , Rb^+ , LiRb^+ etc.) travel approximately along the axis of the spectrometer under field free conditions for ~ 32 cm in the TOF region and are differentiated based on their time of flight. The axis of the spectrometer is tilted at an angle of 5.5° with respect to the vertical MOT beams. The tilt allows the axis of the

spectrometer to be laterally displaced by ~35 mm from the center of the vertical MOT beam at the detection region. In order to improve the ion detection efficiency we use permanent magnets placed at appropriate locations outside the vacuum chamber to steer the ions into the detector. The detection region has a Chevron type matched pair of micro-channel plates (MCP) and a P43 phosphor screen assembly from Tectra GmbH. The detector has an effective diameter of 25 mm. The phosphor screen is aluminized and hence can be used as an anode too. A grounded stainless steel mesh with high transmission is placed in front of the MCP to stop the background ions from entering the MCP. For TOF spectrometry, the front end of the first MCP is held at -1.9 kV, the back of the second MCP is held at -100 V while the phosphor screen (anode) is connected to a fast oscilloscope to record the time of flight trace. We are easily able to differentiate between Rb^+ and LiRb^+ ions based on their time of flights (see chapter 6).

For VMI, which we have not performed yet, the front end of the first MCP will be held at -7 kV, the back of the second MCP will be held at -5 kV while the phosphor screen will be grounded. The ions hitting the MCP will produce electrons which will then be accelerated and amplified, and hit the phosphor screen resulting in emission of light where the electrons hit. A camera will record the image formed on the phosphor screen. Since the divergence of electrons travelling in the high electric field of the MCP can be neglected, the position where the electrons hit the phosphor screen is a direct manifestation of where the ions hit the MCP. The image formed on the phosphor screen is related to the orientation of the LiRb molecules prior to ionization and also to ionization process itself.

3.3 Two-species magneto-optical trap

As discussed in section 3.1, the light for the ^7Li and ^{85}Rb MOTs is coupled into a single optical fiber and brought to the table on which the experiments are performed. This ensures good overlap between the 671 nm and 780 nm beams in addition to a pure Gaussian beam profile. The MOTs are formed by three retro-reflected pairs of mutually perpendicular laser beams intersecting at the center of the UHV chamber. The beams have a $1/e^2$ diameter of ~ 22 mm. The appropriate circular polarizations⁷⁷ of the laser beams are obtained using achromatic quarter wave-plates. The MOTs are operated at an axial (i.e. vertical) magnetic field gradient of ~ 11 Gauss/cm provided by a pair of current carrying coils. It may be noted here that these coils are not exactly in an anti-Helmholtz configuration, resulting in a horizontal magnetic field gradient less than that expected for anti-Helmholtz coils. However, the axial magnetic field gradient still varies linearly with the distance from the center, and the gradient is related to the current by a constant factor of 2.82 (Gauss/cm)/A. We fine tune the overlap of the two MOTs by minor adjustments of the quarter wave-plates. The numbers of trapped atoms change only slightly on adjustment of the quarter wave-plates. When the maximum available laser powers [100 mW (30 mW) in each of the six beams for Rb (Li) MOT] are used, we are able to trap $\geq 2 \times 10^8$ Rb atoms and $\geq 5 \times 10^8$ Li atoms with typical densities of $\sim 4 \times 10^9 \text{ cm}^{-3}$ and $\sim 2 \times 10^{10} \text{ cm}^{-3}$ respectively. Upon reduction of the cooling beam power, we can control (reduce) the MOT size and atom number, facilitating the measurements of the collision rates described in the following section.

The numbers of atoms in the MOTs are monitored by fluorescence detection⁷⁸. The fluorescence from both MOTs is collected using a pair of lenses. The Li and Rb

fluorescence are separated using a dichroic mirror and detected with two separate large-area photodiodes. Around 3.5% (1.5%) of the Li (Rb) fluorescence leaks into the Rb (Li) detection channel. The spurious signal is subtracted from the recorded signal resulting in negligible cross-talk between the Li and Rb detection channels. In addition to the photodiodes, two CCD cameras are used to record the images of both MOTs from two orthogonal directions. The CCD camera images are used to measure the sizes of the two MOTs (used to infer the atom densities) and to monitor their spatial overlap (see Figure 3.5). Typical sizes of the MOTs are ~ 3 mm, and the Li and Rb MOTs are very well overlapped.

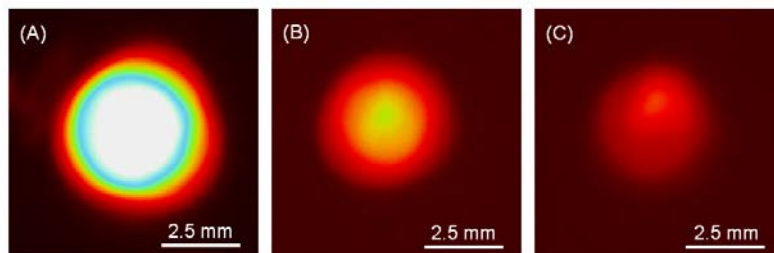


Figure 3.5. False color fluorescence images of the MOTs taken with one of the CCD cameras. (A) Rb MOT in absence of Li MOT, (B) Li MOT in the absence of the Rb MOT, and (C) Li MOT in the presence of the Rb MOT (a filter is used to block most of the Rb fluorescence). The reduction in the number of trapped Li atoms due to the presence of the Rb MOT is clearly visible.

3.4 Measurement and analysis of collision induced losses

Collisions between Li and Rb atoms in the dual-species MOT lead to loss of atoms from the MOT. As a result, the steady state atom number in one MOT is reduced when the MOT of the other species is present. Figure 3.6 shows an example of the Li and Rb MOT fluorescence signals corresponding to the following loading sequence. Initially the Li light (both cooling & repump) and the Rb repumping light are blocked and none of the

MOTs are loaded (the Rb cooling light is always on). At $t = 10$ s, the Li light is unblocked allowing the Li MOT to load. After the Li MOT reaches its steady state, the Rb repumping light is unblocked at $t = 40$ s allowing the Rb MOT to load in presence of the Li MOT. The number of atoms in the Li MOT is now reduced in the presence of the Rb MOT and reaches a new steady state. At $t = 70$ s, the Li light is blocked to remove the Li MOT resulting in an increase of the atom number in the Rb MOT. At $t = 90$ s, both the Li and Rb beams are blocked. The loading sequence is then reversed.

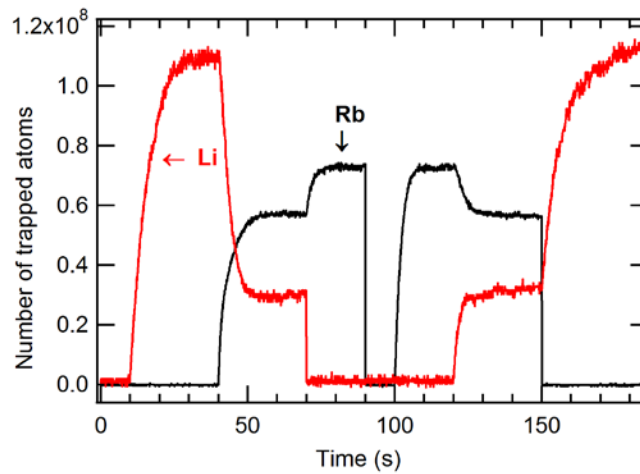


Figure 3.6. Li and Rb MOT fluorescence signal. The loading sequence is described in the text.

The loading of a MOT of species A in the presence of species B can be modeled by the rate equation ⁷⁹:

$$\frac{dN_A}{dt} = L_A - \gamma_A N_A - \beta_A \int n_A^2 d^3r - \beta_{A,B} \int n_A n_B d^3r \quad (3.1)$$

where N_A is the number of atoms in the species A MOT, n_A and n_B are densities of MOTs of species A and B respectively and L_A is the loading rate for species A . γ_A is the 1-body loss rate coefficient accounting for the losses due to collisions with the background gases,

β_A is the 2-body loss rate coefficient accounting for the losses of species A due to collisions between atoms of species A , and $\beta_{A,B}$ is the 2-body loss rate coefficient accounting for the losses of species A due to collisions with species B . The order of indices in $\beta_{A,B}$ is relevant with the first index standing for the species being lost due to the presence of the species indicated by the second index. The analysis of loss rates using the above equation is simplified by the following two conditions which are valid for our experiments: (i) the MOTs operate in the constant density regime, generally true for MOTs with 10^5 or more atoms^{80,81}, where the density of the MOT remains approximately constant during the loading of the MOT while the volume increases, allowing the simplification: $\beta_A \int n_A^2 d^3r = \beta_A n_A N_A$, and (ii) one of the MOTs (A) is smaller than the other MOT (B) allowing the simplification: $\beta_{A,B} \int n_A n_B d^3r = \beta_{A,B} n_B N_A$.

To obtain the value of $\beta_{Li,Rb}$, a small Li MOT is loaded in the presence of a bigger Rb MOT. A smaller Li MOT is obtained either by turning the Zeeman slower magnetic field off or by reducing the power of the Li cooling laser or both. Under these conditions, equation (3.1) can be written as:

$$\frac{dN_{Li}}{dt} = L_{Li} - (\gamma_{Li} + \beta_{Li} n_{Li}) N_{Li} - \beta_{Li,Rb} n_{Rb} N_{Li} \quad (3.2)$$

To obtain the value of $\beta_{Rb,Li}$, a small Rb MOT is loaded in the presence of a bigger, Zeeman slower-loaded Li MOT. A smaller Rb MOT is loaded by reducing the power of the Rb cooling laser. Under this condition, equation (3.1) can be written as:

$$\frac{dN_{Rb}}{dt} = L_{Rb} - (\gamma_{Rb} + \beta_{Rb} n_{Rb}) N_{Rb} - \beta_{Rb,Li} n_{Li} N_{Rb} \quad (3.3)$$

These equations, (3.2) and (3.3), can also be used to describe the loading of a single species MOT by setting the last term to zero, leading to equations of the type:

$$\frac{dN_A}{dt} = L_A - \kappa_A N_A \quad (3.4)$$

where $\kappa_A = (\gamma_A + \beta_A n_A)$. The solution to this equation is:

$$N_A(t) = N_A^\infty (1 - e^{-\kappa_A t}) \quad (3.5)$$

where $N_A^\infty = L_A / \kappa_A$ is the number of atoms in the steady state MOT of species A in the absence of MOT of species B . The values of κ_{Li} , κ_{Rb} , L_{Li} and L_{Rb} are obtained from a fit of equation (3.5) to the experimental loading data for single species MOT. The values depend on the detuning of the respective MOT lasers. For $\delta_{Li} = -9 - -39$ MHz, typical values are: $\kappa_{Li} \sim 0.2-0.1 \text{ s}^{-1}$ and $L_{Li} \sim 2-7 \times 10^7 \text{ s}^{-1}$. For $\delta_{Rb} = -12 - -24$ MHz, typical values are: $\kappa_{Rb} \sim 0.3-0.6 \text{ s}^{-1}$ and $L_{Rb} \sim 1-5 \times 10^7 \text{ s}^{-1}$. We assume that these values measured from single species operation remain unchanged for two species operation.

To obtain the values of $\beta_{Li,Rb}$ and $\beta_{Rb,Li}$, both MOTs are allowed to load simultaneously. When a steady state is reached, (dN_A / dt) of equations (3.2) and (3.3) can be set to zero leading to:

$$\beta_{Li,Rb} = (L_{Li} - \kappa_{Li} \bar{N}_{Li}^\infty) / (\bar{n}_{Rb} \bar{N}_{Li}^\infty)$$

$$\beta_{Rb,Li} = (L_{Rb} - \kappa_{Rb} \bar{N}_{Rb}^\infty) / (\bar{n}_{Li} \bar{N}_{Rb}^\infty)$$

where, the “ $\bar{}$ ” is used to denote the steady-state number of atoms or density of MOTs when both species are simultaneously present.

The loss rate coefficients generally depend on the MOT parameters such as laser intensities and detuning^{79,82,83}. We can use these dependences to understand the nature of the inelastic collisions that lead to trap loss, as has been done previously with losses for other species^{79,82}. Several possible mechanisms have been identified, including radiative escape (RE), fine-structure changing collisions, hyperfine changing collisions, and molecule formation. In RE, atoms *A* (in an excited electronic state, designated *A**) and *B* (in its ground state) approach one another along an attractive potential energy curve. As their potential energy decreases, their kinetic energy (and velocity) increases. Spontaneous emission during the collision will then generate a scattered photon at a lower energy than that of the photon originally absorbed by *A*, with the difference in energy found as kinetic energy of the ground state atoms *A* and *B*. If this energy is greater than the trapping potential for either *A* or *B*, then one or both of these atoms can escape from the trap, contributing to the trap losses. In the Li-Rb system, Rb*-Li collisions (where the asterisk indicates the Rb is in the $5p\ ^2P_{3/2}$ state) can result in RE, but the potential curves for Li*-Rb collisions (in which Li* designates Li in the $2p\ ^2P_{3/2}$ state), are repulsive, and RE is precluded. The spontaneous emission event can also leave atom *A* or *B* in the untrapped hyperfine ground state, also leading to trap loss, depending on the recovery rate of atoms in this state by the repump laser and the MOT trap depth. In the present work, the repump beams are relatively intense (leading to rapid recovery of these atoms) and the MOT trap depths are relatively high; hence, we expect that losses due to these hyperfine state changing processes are not significant. Collisions can also cause transitions between fine-structure states (of the excited state, since the ground state of an alkali metal atom has no fine structure) or hyperfine states (of the ground or excited

states, although trap loss is more likely when changing hyperfine states in the ground state atoms due to the larger hyperfine energy in the ground state than in the excited state). The energy difference between the fine-structure states or hyperfine states is transferred to kinetic energy of A and B , which can result in their loss from the MOT. However, as discussed above, we do not expect hyperfine changing collisions to be important in our system since the MOT trap depths (> 1 K) are significantly higher than the energy associated with the hyperfine structures (maximum energy is 3.04 GHz, i.e. ~ 0.14 K, corresponding to the ground state hyperfine splitting of ^{85}Rb). It is difficult to differentiate between fine structure changing collisions and RE on the basis of our measurements, and they are together referred to as losses due to Li-Rb* collisions. Finally, formation of a molecule AB by the colliding atoms results in loss of both species from the traps.

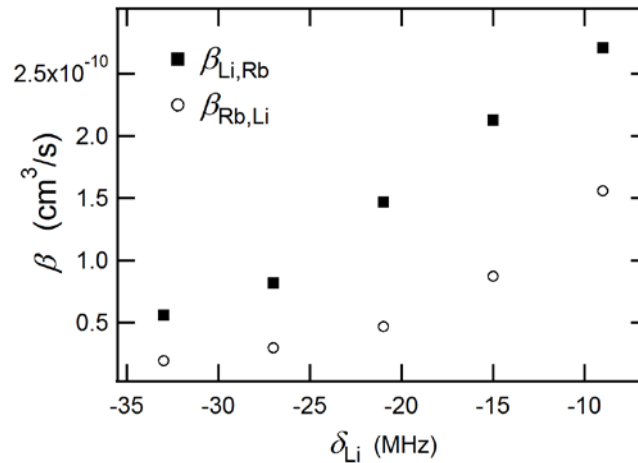


Figure 3.7. The dependence of the loss rate coefficients on the detuning (δ_{Li}) of the Li cooling laser. The Li repump detuning is fixed at -18 MHz, the Rb cooling laser detuning is fixed at -24 MHz and the Rb repump is resonant. The filled squares and open circles are the values of $\beta_{\text{Li,Rb}}$ and $\beta_{\text{Rb,Li}}$ respectively.

In Figure 3.7, we show the dependence of $\beta_{Li,Rb}$ on the detuning δ_{Li} of the Li cooling beam from the $F = 2 \rightarrow F' = 3$ transition, with the detuning (δ_{Rb}) of the Rb cooling beam held fixed at $\delta_{Rb} = -24$ MHz. It is seen that the value of $\beta_{Li,Rb}$, characterizing the Rb-induced Li loss, decreases from $\sim 2.7 \times 10^{-10}$ cm³/s at $\delta_{Li} = -9$ MHz to $\sim 5.6 \times 10^{-11}$ cm³/s at $\delta_{Li} = -33$ MHz.

The detuning δ_{Li} affects three primary MOT characteristics^{84,85,86}, which in turn can affect the collisional loss rates. With increasing detuning $|\delta_{Li}|$, the trap depth increases, the temperature of the Li MOT increases and the population in the excited $2p \ ^2P_{3/2}$ state decreases. (The increasing trap depth and increasing temperature of the Li MOT with increasing $|\delta_{Li}|$ is uncommon among trapped atomic species. In most traps, such as Rb, the trap depth and temperature *decrease* with increasing detuning of the trapping laser.) The dependence of $\beta_{Li,Rb}$ on δ_{Li} shown in Figure 3.7 is consistent with the variation of trap depth, but counter to the variation in temperature. As we increase $|\delta_{Li}|$, the increasing trap depth makes it more difficult for Li atoms to escape the trap, as reflected in the decreased loss rate coefficient $\beta_{Li,Rb}$. Conversely, we expect that the increasing temperature of the Li MOT with increasing $|\delta_{Li}|$ would manifest itself as an *increasing* $\beta_{Li,Rb}$. (An increase in the temperature implies an increase in the (average) velocity v_{Li} of Li atoms. But v_{Li} is nearly equal to the relative velocity of the colliding Li and Rb atoms, since the average velocity v_{Rb} of the Rb atoms is expected to be much less than v_{Li} . This is because the typical temperature of the Rb MOT (few hundred μ K) is much lower than the typical temperature (few mK) of the Li MOT, and the Rb atomic mass m_{Rb} is much greater than the Li atomic mass m_{Li} .) In inelastic collisions, energy and momentum

conservation during collisions require that a fraction $m_{Rb}/(m_{Li} + m_{Rb}) \approx 92\%$ of any released energy be deposited in the lighter Li atom after a Li-Rb collision. The gain in kinetic energy of Li atoms is much greater than that of Rb atoms and it is thus much more likely for a Li atom to leave the trap (typical Li MOT trap depth $\sim 1\text{K}$ ⁸⁴) than a Rb atom (typical Rb MOT trap depth $\sim 10\text{K}$ ^{77,87}). Another possible factor, the population of the Li excited $2p\ ^2P_{3/2}$ state, can also be ruled out because the interaction between an excited ($2p\ ^2P_{3/2}$) Li atom and a ground state ($5s\ ^2S_{1/2}$) Rb atom is repulsive^{88,89,90} preventing the Li and Rb atoms from getting close enough where inelastic loss-inducing collisions can occur. Our observation that $\beta_{Li,Rb}$ increases with decreasing detuning $|\delta_{Li}|$, therefore, leads us to conclude that the variation in the trap depth is more important than that of the temperature of the Li atoms.

Figure 3.7 also shows the dependence of $\beta_{Rb,Li}$, characterizing Li-induced Rb losses, on the detuning δ_{Li} of the Li cooling beam, with the detuning of the Rb cooling beam held fixed at $\delta_{Rb} = -24\text{ MHz}$. The trend is similar to that of $\beta_{Li,Rb}$, with $\beta_{Rb,Li}$ being a factor of ~ 3 lower than $\beta_{Li,Rb}$. The trend cannot be attributed to an increase in Li MOT trap depth with increasing detuning since the Li MOT trap depth cannot play a role in determining the Rb losses. The dependence can also not be attributed to the increase in Li MOT temperature with increasing detuning, since that would imply an increase in $\beta_{Rb,Li}$ with increasing detuning, contrary to the experimental observation. In addition, as mentioned above, the population of the excited ($2p\ ^2P_{3/2}$) state Li atoms should play no role in determining $\beta_{Rb,Li}$ or $\beta_{Li,Rb}$. We speculate that this could be indicative of molecule formation, to be discussed in the following paragraph, but at this moment, we

are unable to provide a convincing explanation for the observed trend. We also note that the trend is actually reverse of that observed for $\beta_{Cs,Li}$ ⁸³, where the increase in $\beta_{Cs,Li}$ with increasing $|\delta_{Li}|$ was attributed to the increase in the Li MOT temperature.

In order to study the dependence of $\beta_{Li,Rb}$ and $\beta_{Rb,Li}$ on the detuning δ_{Rb} of the Rb cooling beam, the above measurements were repeated at a lower detuning of $\delta_{Rb} = -18$ MHz and $\delta_{Rb} = -12$ MHz. Within our experimental uncertainty, the values of $\beta_{Li,Rb}$ and $\beta_{Rb,Li}$ were comparable for all three values of δ_{Rb} . The dependence of the trap depth and temperature of the Rb MOT on $|\delta_{Rb}|$, both of which decrease with increasing $|\delta_{Rb}|$, is opposite that of the Li MOT; while population in the excited $5p\ ^2P_{3/2}$ state decreases with increasing $|\delta_{Rb}|$ ^{77,91}. We expect that the temperature of the Rb MOT, however, has little affect on the loss rate coefficients because the relative velocity of collisions is determined solely by the temperature of the much hotter Li MOT, as already mentioned. The interaction between ground state Li atoms and Rb atoms in the excited $5p\ ^2P_{3/2}$ state (denoted by Rb*) is attractive in nature and can aid in bringing the Li and Rb atoms close enough for loss inducing collisions to occur. The population of Rb in the excited $5p\ ^2P_{3/2}$ state decreases with increasing detuning $|\delta_{Rb}|$, which should reduce Rb-induced Li losses. We are unable to observe this effect in our collision induced loss measurements but this could be due to the relatively small range over which δ_{Rb} is varied. However, our observations, detailed below, while using a dark MOT for Rb clearly indicate that collisions between ground state Li and excited Rb* atoms account for majority of the atom losses observed.

The values of $\beta_{Li,Rb}$ and $\beta_{Rb,Li}$ for 7Li and ^{85}Rb are being reported here for the first time. It is interesting to compare these with the values of other isotopes of Li and Rb (Table 3.1). The loss rate coefficients for 6Li and ^{85}Rb have been reported to be $\beta_{^6Li,^{85}Rb} = 4 \times 10^{-10} \text{ cm}^3/\text{s}$ and $\beta_{^{85}Rb,^6Li} = 5 \times 10^{-11} \text{ cm}^3/\text{s}$ ⁹². These values were measured for $\delta_{Rb} = -11 \text{ MHz}$ and $\delta_{Li} = -34 \text{ MHz}$. At similar detuning, we find the loss rate coefficients for 7Li and ^{85}Rb to be $\beta_{^7Li,^{85}Rb} = 5.6 \times 10^{-11} \text{ cm}^3/\text{s}$ and $\beta_{^{85}Rb,^7Li} = 2.0 \times 10^{-11} \text{ cm}^3/\text{s}$. Thus the values of $\beta_{Rb,Li}$ are similar for the two cases but the value of $\beta_{Li,Rb}$ is significantly different.

Table 3.1. Values of loss rate coefficients (in cm^3/s) measured for conventional bright MOTs. Parameters involving 6Li are from Ladouceur *et al.*⁹² while those involving 7Li are measured in our experiment. There are no reported measurements for $^7Li - ^{87}Rb$. The dependence of loss rate coefficients on the isotopes could be attributable to the binding energy of the highest energy vibrational state within the electronic potential well, or possibly differences in the hyperfine structures of different isotopes⁷⁷. In the final row, we present the ratios $\beta_{Li,Rb} / \beta_{Rb,Li}$ for these different isotopic systems.

	$^7Li - ^{85}Rb$	$^6Li - ^{85}Rb$	$^6Li - ^{87}Rb$
$\beta_{Li,Rb}$	5.6×10^{-11}	4×10^{-10}	2.5×10^{-10}
$\beta_{Rb,Li}$	2.0×10^{-11}	5×10^{-11}	1.7×10^{-11}
$\beta_{Li,Rb} / \beta_{Rb,Li}$	2.8	8	15

In contrast to the observation of Ladouceur *et al.*⁹², where $\beta_{^6Li,^{85}Rb}$ is an order of magnitude higher than $\beta_{^{85}Rb,^6Li}$, we observe that the values of $\beta_{^7Li,^{85}Rb}$ and $\beta_{^{85}Rb,^7Li}$ differ by only a factor of ~ 3 . (Direct comparison of loss rate coefficients, $\beta_{Li,Rb}$ or $\beta_{Rb,Li}$, with those determined for other isotopic systems by other research groups, can

be difficult due to uncertainties in the absolute determination of atomic densities or numbers, as well as subtle differences in laser powers or detunings. We therefore compare ratios $\beta_{Li,Rb} / \beta_{Rb,Li}$ for the different isotopic species, which we expect to be more reliable.) We speculate that the similarity in the values of $\beta_{Li,^{85}Rb}$ and $\beta_{^{85}Rb,^7Li}$ can be explained by the formation of LiRb molecules in the electronic ground state. LiRb molecules in the electronic ground state can be formed in the two-species MOT by spontaneous emission of excited state LiRb* molecules formed by collisions of Li and Rb* atoms. The molecules, being transparent to the MOT beams, cannot be trapped and both atoms are lost from the MOT. Since $\beta_{Li,Rb}$ and $\beta_{Rb,Li}$ are similar, but not identical ($\beta_{Li,Rb} / \beta_{Rb,Li} \sim 3$), this could indicate that about 30% of the collisions lead to molecule formation, resulting in the loss of a Li and Rb atom from the trap, while the majority of collisions lead to the loss of a Li atom alone. Subtle differences between the vibrational energies of excited potentials for different isotopic species could allow for differences in molecule formation rates. For example, isotopic changes in the vibrational energy spacing can change the binding energy of the highest bound vibrational level substantially, affecting the collision process. A difficulty with this explanation lies with dependence of this rate on δ_{Li} and δ_{Rb} . The molecule formation rate should depend only on the Rb detuning (and not on Li detuning) because the Li-Rb* interaction is attractive while Li*-Rb is repulsive. In Figure 3.7, only the Li* population is being changed, yet we see variation of both loss coefficients. If molecule formation is the only loss mechanism, then both $\beta_{Li,Rb}$ and $\beta_{Rb,Li}$ should have been individually constant as the Li detuning was changed. This is obviously not the case. The other way to think about it is that the

molecules, if formed, are always lost from the trap, irrespective of the MOT trap depth/detuning. If molecule formation by the MOT beams is indeed active, this mechanism would provide a simple method for the production of ultracold LiRb molecules in the electronic ground state. However, more work, for example using REMPI to detect the LiRb molecules formed in the MOT, is needed to confirm this conjecture.

A few words about possible sources of errors in the measurement of $\beta_{Li,Rb}$ and $\beta_{Rb,Li}$ are warranted here. Random errors in the values of $\beta_{Li,Rb}$ and $\beta_{Rb,Li}$ are minimal and the trends seen in Figure 3.7 are reproducible. The primary sources of error are the systematic errors arising from the uncertainties in the measurement of the number of atoms in and the sizes of the MOTs. The calculation of atom number requires the knowledge of the photon scattering rate which in turn depends on the intensity, polarization and detuning of the MOT cooling beams. The detuning is quite well determined in our experiments as is the intensity, but the polarization may not be perfect, and it varies through the MOT region due to interference effects between the six trapping beams. Other errors arise from the uncertainty in the solid angle subtended by the MOT at the collection lens and on the photon collection efficiency of the imaging system. Collectively these lead to an estimated systematic error of $\sim 25\%$ in the measurement of number of atoms trapped in the MOTs. The sizes (diameters) of the MOTs are estimated to be accurate within 15%. Together, these lead to an uncertainty of $\sim 50\%$ in the determination of $\beta_{Li,^{85}Rb}$ and $\beta_{^{85}Rb,^7Li}$. However, as noted earlier, these are systematic errors appearing in every measurement and hence the trends seen in Figure 3.7 should not change significantly. Such uncertainties are typical in the measurement of loss rates⁸³.

3.5 Reduction of collision induced losses in a dark Rb MOT

As discussed earlier, the population of Rb atoms in the excited $5p\ ^2P_{3/2}$ state can cause the loss of Li atoms from the MOT. The importance of the role of Rb*-Li collisions is further supported by our measurements of interspecies collision-induced losses with a dark MOT, also known as the dark spontaneous-force optical trap^{93,94}. In a dark MOT for Rb, the population in the excited $5p\ ^2P_{3/2}$ state is reduced, and the trapped atoms primarily occupy the $5s\ ^2S_{1/2}\ F = 2$ state. We obtain a dark Rb MOT by blocking the center of the Rb repumping beam with an opaque circular disc 6 mm in diameter. In addition, we detune the Rb repumping beam by +12 MHz from the $F = 2 \rightarrow F' = 3$ transition. We found that the use of an additional depumping beam, tuned to the $F = 3 \rightarrow F' = 2$ transition, was not required to reduce the Rb-induced Li losses.

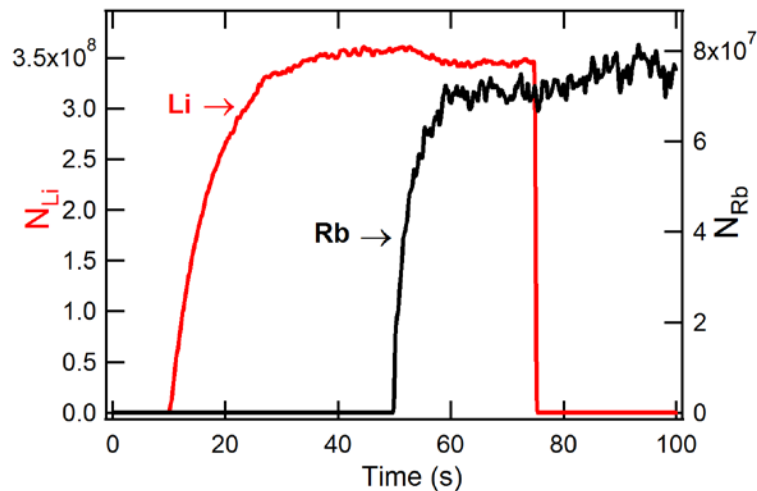


Figure 3.8. Simultaneous loading of a Li MOT (red, left axis) and dark Rb MOT (black, right axis). The Li MOT starts loading at $t = 10$ s and is allowed to reach steady state. At $t = 50$ s, the Rb dark MOT starts loading and a very small reduction in the Li MOT atom number is seen. At $t = 75$ s the Li MOT is blocked and a very small increase in the dark Rb MOT atom number is seen. The interspecies collision induced losses are greatly reduced when a dark Rb MOT is used.

Figure 3.8 shows the MOT loading curves when a Li MOT and a dark Rb MOT are simultaneously loaded where the losses are substantially reduced (also see Figure 3.9). It is seen that the number of trapped atoms of one species is affected only slightly by the presence of the other species, thus preserving the densities also. With the dark Rb MOT we are able to simultaneously trap $\geq 5 \times 10^8$ Li atoms and $\geq 2 \times 10^8$ Rb atoms. The result also clearly indicates that collisions of Li atoms with Rb atoms in the excited $5p \ ^2P_{3/2}$ state lead to the severe loss of Li atoms from the Li MOT, as speculated earlier. The reduction in collision induced losses is crucial for the experiments discussed in the following chapters.

3.6 Alternate method for the measurements of collision induced losses

The Li loss rate coefficient $\beta_{Li,Rb}$ can be measured using a different method. The Li MOT is first allowed to load and reach a steady state ($N_{Li,Max}$) in the absence of the Rb MOT. The Li atomic beam is then suddenly blocked which suddenly changes the loading rate L_{Li} to zero. The decrease in the Li MOT atom number (N_{Li}) is shown in Figure 3.9A. The evolution of N_{Li} can be described by equation 3.4 with L_{Li} set to zero, and, the solution to the equation is $N_{Li} = N_{Li,Max} e^{-\kappa_{Li} t}$. In Figure 3.9B we plot $\ln(N_{Li}/N_{Li,Max})$ vs. t and extract κ_{Li} ($\sim 1/7.5 \text{ s}^{-1}$) from the slope of the red curve. Next, the Li MOT is allowed to load in presence of the Rb MOT and it reaches a new steady state. The Li atomic beam is then blocked and the evolution of N_{Li} can be described by equation 3.3 with L_{Li} set to zero. The solution to the equation is $N_{Li} = N_{Li,Max} e^{-\kappa_{Li,Rb} t}$, where $\kappa_{Li,Rb} = \kappa_{Li} + \beta_{Li,Rb} n_{Rb}$. In Figure 3.9B we plot $\ln(N_{Li}/N_{Li,Max})$ vs. t and extract $\kappa_{Li,Rb}$

($\sim 1/1.7 \text{ s}^{-1}$) from the slope of the blue curve. We then calculate $\beta_{Li,Rb}$ from the relation:

$$\beta_{Li,Rb} = (\kappa_{Li,Rb} - \kappa_{Li}) / n_{Rb} \quad (\sim 1.5 \times 10^{-10} \text{ cm}^3/\text{s}).$$

The value $\beta_{Li,Rb}$ obtained using this method is consistent with the value obtained using the previous method. Note that this method is relatively immune to small errors in the measurement of Li atom number and density. For completeness, we also plot the evolution of N_{Li} in the presence of a dark Rb MOT and find that using a dark Rb MOT significantly reduces the Li losses and $\beta_{Li,Rb}$.

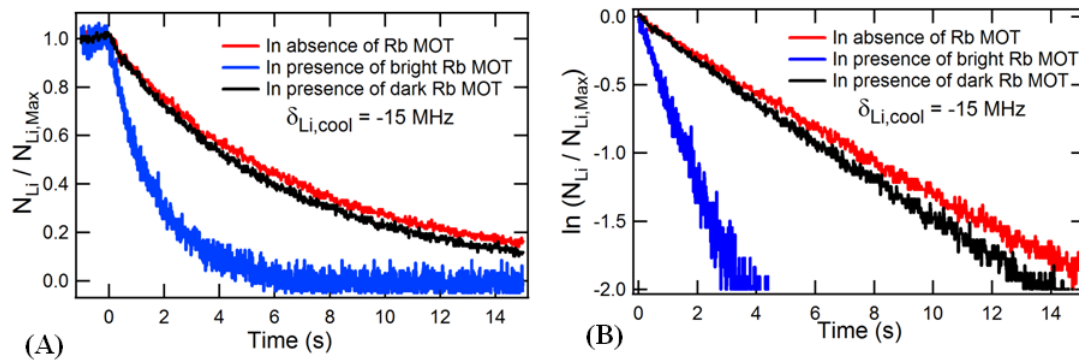


Figure 3.9. The decay of Li MOT atom number when the Li atomic beam is suddenly blocked at $t = 0 \text{ s}$. The ratio $N_{Li} / N_{Li,Max}$ in linear scale (A) and log scale (B) as a function of time after the atomic beam is blocked. In absence of the Rb MOT, the Li atoms number decreases slowly with a lifetime $\sim 7.5 \text{ s}$. In the presence of the bright Rb MOT, the Li atoms number decreases much more quickly with a lifetime $\sim 1.7 \text{ s}$. In the presence of the dark Rb MOT, the Li atoms number decreases slowly with a lifetime $\sim 6.5 \text{ s}$. This suppression of collision induced losses with a dark Rb MOT indicates that the Li losses are mainly due to collision of Li with excited state Rb atoms.

CHAPTER 4. PHOTOASSOCIATION OF LIRB MOLECULES

In this chapter, I will discuss the production of ultracold ${}^7\text{Li}{}^{85}\text{Rb}$ molecule in excited electronic states by photoassociation (PA) of ultracold ${}^7\text{Li}$ and ${}^{85}\text{Rb}$ atoms. PA is performed in the dual-species ${}^7\text{Li}$ - ${}^{85}\text{Rb}$ MOT described in the previous chapter and the PA resonances are detected using trap loss spectroscopy. We identify several strong PA resonances below the Li ($2s\ {}^2\text{S}_{1/2}$) + Rb ($5p\ {}^2\text{P}_{1/2}$) and the Li ($2s\ {}^2\text{S}_{1/2}$) + Rb ($5p\ {}^2\text{P}_{3/2}$) asymptotes, and experimentally determine the long range C_6 dispersion coefficients. For the strongest PA line observed, we find an excited state LiRb* molecule formation rate (P_{LiRb}) of $3.5 \times 10^7\ \text{s}^{-1}$ and a PA rate coefficient (K_{PA}) of $1.3 \times 10^{-10}\ \text{cm}^3/\text{s}$, the highest among heteronuclear bi-alkali molecules. We also observe the saturation of the PA rate coefficient (K_{PA}) close to the theoretical value at the unitarity limit. These results are very promising and provide the first concrete step towards the production of ultracold LiRb molecules in their rovibronic ground state.

4.1 Experimental setup

For the PA experiments, we use the dual-species MOT described in the previous chapter i.e. a conventional MOT for ${}^7\text{Li}$ and a dark MOT for ${}^{85}\text{Rb}$. The typical number (N_{Li}) of trapped ${}^7\text{Li}$ atoms is around 5×10^7 at a density (n_{Li}) around $5 \times 10^9\ \text{cm}^{-3}$. The majority of the trapped ${}^7\text{Li}$ atoms are in the upper ($F = 2$) hyperfine level of the $2s\ {}^2\text{S}_{1/2}$ state. The typical number (N_{Rb}) of trapped ${}^{85}\text{Rb}$ atoms is around 1×10^8 at a density (n_{Rb}) around

$4 \times 10^9 \text{ cm}^{-3}$. The majority of the ^{85}Rb atoms are in the lower ($F = 2$) hyperfine level of the $5s \ ^2\text{S}_{1/2}$ state. The trapped atoms collide mainly along the $^7\text{Li} (2s \ ^2\text{S}_{1/2}, F = 2) + ^{85}\text{Rb} (5s \ ^2\text{S}_{1/2}, F = 2)$ channel. Good spatial overlap of the two MOTs is monitored using a pair of cameras placed orthogonal to each other. The fluorescence from both MOTs is collected using a pair of lenses, separated using a dichroic mirror and recorded on two separate photodiodes.

We use a Ti:Sapphire laser for PA. The laser has a linewidth less than 1 MHz, maximum output power of 450 mW and maximum mode-hop-free scan of around 20 GHz. The PA laser beam is collimated to a $1/e^2$ diameter of 0.85 mm, leading to a maximum available peak intensity of about 150 W/cm^2 . The wavelength of the laser is tuned near 795 nm or 780 nm in order to record the PA spectrum below the $\text{Li} (2s \ ^2\text{S}_{1/2}) + \text{Rb} (5p \ ^2\text{P}_{1/2})$ and the $\text{Li} (2s \ ^2\text{S}_{1/2}) + \text{Rb} (5p \ ^2\text{P}_{3/2})$ asymptotes, respectively. PA resonances lead to the formation of LiRb^* molecules in excited electronic states, which either spontaneously decay to electronic ground state LiRb molecules or to free Li and Rb atoms with high kinetic energies. Both mechanisms result in loss of Li and Rb atoms from the MOT leading to a decrease in the MOT fluorescence. The PA resonances, and hence formation of LiRb^* molecules, can thus be detected using this PA-induced trap loss spectrum. Trap loss in the Li MOT occurs solely due to LiRb^* PA resonances since Li_2^* PA resonances are weak/absent near 795 nm or 780 nm. Trap loss should also be observable in the Rb-MOT but the fluorescence from the Rb dark-MOT is weak and the spectrum is complicated by Rb_2^* PA resonances. To obtain the LiRb^* PA spectrum, we thus record the Li MOT fluorescence as the frequency of the PA laser is scanned. As an

additional check for LiRb* molecules, we have verified that the trap loss features in the Li fluorescence are present only when both Li and Rb atoms are simultaneously trapped.

4.2 Molecular potentials

Figure 4.1a shows the first few electronic states of the LiRb molecule for small internuclear separations (R). For the PA levels close to the atomic asymptotes, the internuclear separation is larger and the potential is determined mainly by the C_6 coefficients^{88,89,90} (Figure 4.1b). It is appropriate to use the Hund's case (a) notation for small R and Hund's case (c) notation for large R . The correlation between Hund's case (a) and case (c) labels is shown in Table 4.1 (see ref. 22 page 315 and refs. 95-97).

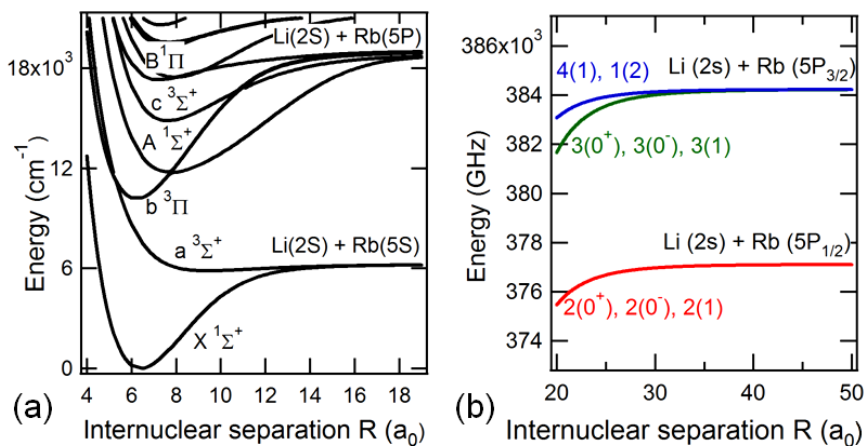


Figure 4.1. a) Theoretical potential energy curves of LiRb for small internuclear separations⁶⁰. (b) Theoretical potential energy curves at large internuclear separations determined solely by the C_6 coefficients⁸⁸. Only these curves are relevant to the presented PA measurements.

Table 4.1. Correlation between potentials at short and long range

Small R	Large R	Asymptote
$X^1\Sigma^+, a^3\Sigma^+$	$1(0^+), 1(0^-), 1(1)$	$\text{Li}(2s^2S_{1/2}) + \text{Rb}(5s^2S_{1/2})$
$A^1\Sigma^+, c^3\Sigma^+$	$2(0^+), 2(0^-), 2(1)$	$\text{Li}(2s^2S_{1/2}) + \text{Rb}(5p^2P_{1/2})$
$B^1\Pi, b^3\Pi$	$3(0^+), 3(0^-), 3(1), 4(1), 1(2)$	$\text{Li}(2s^2S_{1/2}) + \text{Rb}(5p^2P_{3/2})$

In Hund's case (a), both the molecular electronic orbital angular momentum \mathbf{L} ($= \mathbf{l}_1 + \mathbf{l}_2$) and the electronic spin \mathbf{S} ($= \mathbf{s}_1 + \mathbf{s}_2$) are strongly coupled to the internuclear axis (the subscripts denote the two atoms)^{22,43}. The spin-orbit coupling between \mathbf{S} and \mathbf{L} mediates the coupling of \mathbf{S} to the internuclear axis (this coupling vanishes for $\mathbf{L} = 0$ and the appropriate scheme is Hund's case (b)). The projections of \mathbf{L} and \mathbf{S} on the internuclear axis are Λ and Σ respectively, while $\Omega = \Lambda + \Sigma$ is the projection of the total electronic angular momentum. The electronic states are labeled as $^{2\Sigma+1}\Lambda^{+/-}$, where $\Lambda = \Sigma, \Pi, \Delta, \dots$ depending on $L_z = 0, 1, 2, \dots$ and the $-/+$ denotes whether or not the spatial electronic wave function changes sign upon reflection at any plane containing the internuclear axis. Hund's case (a) is generally used to label electronic states when the internuclear separation (R) is small.

Hund's case (c) is used at large internuclear separation where the spin-orbit interaction between \mathbf{L} and \mathbf{S} dominates over their individual coupling to the internuclear axis. In this case Ω is a good quantum number but Λ and Σ are not. The PA lines observed in this thesis are close to the dissociation limit and it is appropriate to use Hund's case (c) to label these PA lines. The states are labeled $n(\Omega^\sigma)$ ^{43,44,95,96,97}, where Ω is the projection of the total electronic angular momentum on the internuclear axis, $\sigma = -/+$ (only for $\Omega = 0$ states) depending on whether or not the electronic wave function changes sign upon reflection at any plane containing the internuclear axis, and n is a number denoting the n^{th} electronic state of a particular Ω^σ .

As shown in Figure 4.1b, there are three, almost identical, electronic states asymptotic to the Li ($2s \ ^2S_{1/2}$) + Rb ($5p \ ^2P_{1/2}$) asymptote. The potential energy curves of the three states, $2(0^+)$, $2(0^-)$ and $2(1)$, are almost identical since at such large internuclear

separations (R) the electronic potentials, $V(R) = -C_6/R^6$, are almost entirely determined by the C_6 coefficients which are very similar for the three electronic states^{88,89,90}. Experimentally, however, it is possible to determine three distinct, although similar, C_6 coefficients for these states. There are five other electronic states, $3(0^+)$, $3(0^-)$, $3(1)$, $4(1)$ and $1(2)$, converging to the Li ($2s \ ^2S_{1/2}$) + Rb ($5p \ ^2P_{3/2}$) asymptote (i.e. the Rb D_2 asymptote). It has been predicted^{88,89} that the $3(0^+)$, $3(0^-)$ and $3(1)$ have very similar C_6 coefficients, are almost indistinguishable and form a triad; while the $4(1)$ and $1(2)$ have very similar C_6 coefficients, are almost indistinguishable and form a diad. Only these five states are relevant for PA near the D_2 asymptote. For PA below the D_1 asymptote, the transition strengths of the $3(0^+)$, $3(0^-)$, $3(1)$, $4(1)$ and $1(2)$ states are expected to be very weak and hence only the $2(0^+)$, $2(0^-)$ and $2(1)$ states need to be considered for PA below the D_1 asymptote. We first consider the $2(0^+)$, $2(0^-)$ and $2(1)$ states in section 4.3 and then discuss the $3(0^+)$, $3(0^-)$, $3(1)$, $4(1)$ and $1(2)$ states in section 4.4.

4.3 Photoassociation below the Li ($2s \ ^2S_{1/2}$) + Rb ($5p \ ^2P_{1/2}$) asymptote

The experimentally observed LiRb* PA resonances below the Li ($2s \ ^2S_{1/2}$) + Rb ($5p \ ^2P_{1/2}$) asymptote are shown in Figure 4.2. The spectrum in Figure 4.2a is obtained by stitching together several short PA scans shown in Figures 4.2b-j. The detuning Δ_{PA} of the PA laser is measured with respect to the frequency ν_{res} ($= 377108.946$ GHz) of the Rb ($5s \ ^2S_{1/2}, F = 2$) \rightarrow Rb ($5p \ ^2P_{1/2}, F' = 2$) transition i.e. $\Delta_{PA} = \nu_{PA} - \nu_{res}$, where ν_{PA} is the frequency of the PA laser. The detuning Δ_{PA} is thus a measure of the binding energies (E_B) of the respective ro-vibrational levels. The spectrum is obtained by scanning the frequency of the PA laser at around 1.9 MHz/s and with a peak intensity ~ 100 W/cm².

The absolute accuracy in the measurement of PA line frequency is ~ 100 MHz, determined primarily by the accuracy (60 MHz) of the wavelength-meter used for these measurements. The relative accuracy of the frequency measurement and the frequency resolution are however much better. The full width at half maximum (FWHM) linewidth of the narrowest lines are found to be ~ 33 MHz, which is reasonable given the natural linewidth (~ 12 MHz) and the thermal broadening (~ 21 MHz) arising due the initial spread of collision energies at the temperature (1 mK) of a typical Li MOT.

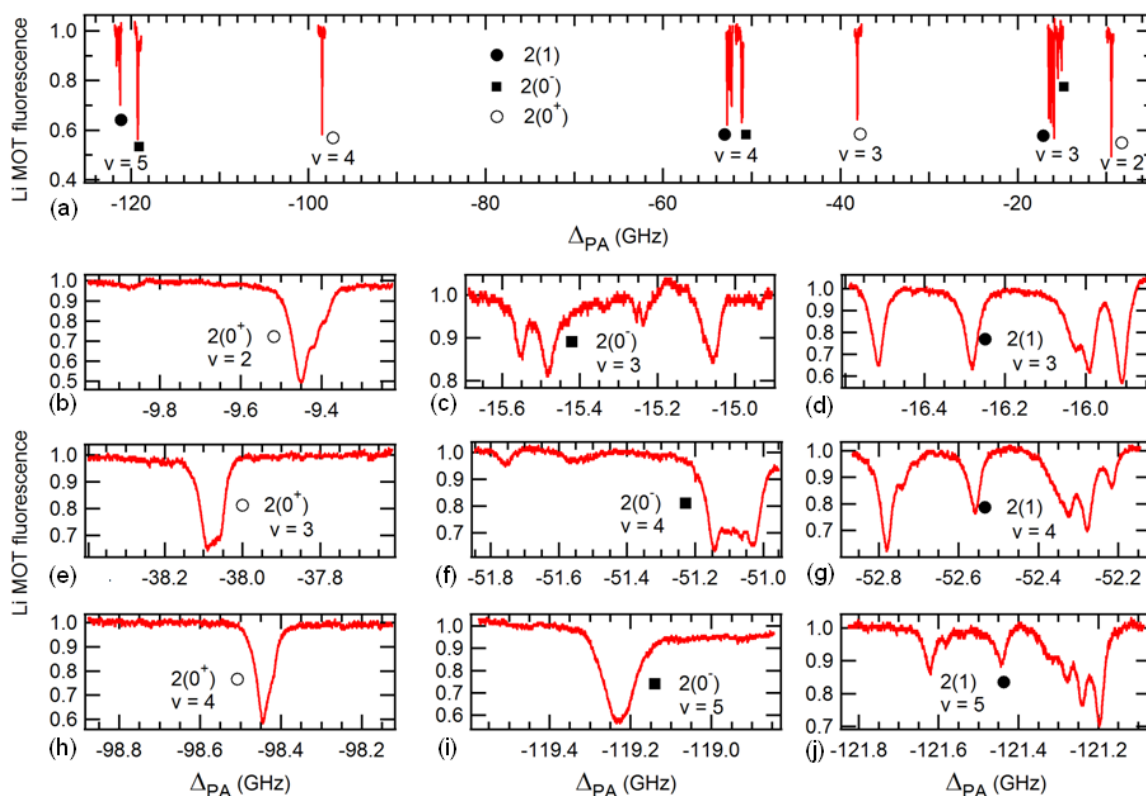


Figure 4.2. PA spectrum of LiRb* below the Li ($2s \ ^2S_{1/2}$) + Rb ($5p \ ^2P_{1/2}$) asymptote measured using trap loss spectroscopy. (a) Compilation of all strong PA lines. (b-j) Zoom-in view showing the internal structures of the PA lines. The electronic states and vibrational levels (measured from the dissociation limit) are also indicated.

4.3.1 Assignment of spectra below the Li ($2s\ ^2S_{1/2}$) + Rb ($5p\ ^2P_{1/2}$) asymptote

In order to assign the spectra, we group the observed PA lines based on their structure and assign them to one of the three potentials. For example, the $\Omega = 1$ state is expected to have hyperfine structure and we thus assign the lines with multiple structures to the $2(1)$ state^{43,96,97}. The $\Omega = 0$ states, on the other hand, are expected to have no hyperfine structure (in the first order). Note that the $2(0^-)$ state is found to have internal structure for the least bound levels but the structure decreases (and goes away) for more deeply bound levels. We believe that the structure in the loosely bound levels of the $2(0^-)$ state is due to mixing with the nearby $2(1)$ state which lies very close to the $2(0^-)$ state. For deeply bound levels, the $2(0^-)$ and $2(1)$ states are well-separated, the mixing become negligible and the $2(0^-)$ state has negligible internal structure as expected. The internal structure (which is attributed to the hyperfine structure) in the $2(1)$ state persists even for deeply bound levels, as expected. We distinguish between the $2(0^+)$ and the $2(0^-)$ states based on the fact that the $2(0^-)$ state is expected to lie closer to the $2(1)$ state⁹⁵, but also note that their assignment may need to be inter-changed when more spectroscopic data become available. We assign the vibrational level v (v is measured from the asymptote such that $v = 1$ is the least bound level) for each electronic state such that it is consistent with the LeRoy-Bernstein (LRB) formula⁹⁸ as discussed later. We note that we observe only one rotational (J) level for each vibrational level, which, as discussed below, is somewhat unexpected.

The angular momentum selection rules for the electric dipole allowed transitions are: $\Delta\Omega = 0, \pm 1$, $\Delta J = 0, \pm 1$, $0^+ \leftrightarrow 0^+$, $0^- \leftrightarrow 0^-$, $J \geq \Omega$, $\Delta J \neq 0$ if $\Omega = 0$ for both states and $J = 0 \rightarrow J = 0$ transitions are not allowed^{43,96,97}. There are three possible electronic potentials,

$1(0^+)$, $1(0^-)$ and $1(1)$, along which collisions between ground state Li and Rb atoms can occur. These collisions are primarily s -wave ($l = 0$) collisions since the centrifugal barrier for all higher partial waves ($l > 0$) is high enough that the ultracold atoms do not have sufficient kinetic energy to overcome the barrier and come close enough for PA to occur. For example, we estimate the height of the p -wave ($l = 1$) centrifugal barrier at $\sim 100 a_0$ to be ~ 1.9 mK using theoretical value of C_6 ($= 2500$ a.u.) for the Li ($2s \ ^2S_{1/2}$) + Rb ($5s \ ^2S_{1/2}$) asymptote⁸⁹. This barrier is higher than the typical temperature (~ 1 mK) of the MOT. Note that the observed PA levels have outer turning points R_{out} in the range $30 - 44.6 a_0$ (see below); so, in accordance with the Born-Oppenheimer approximation for the free-bound transition, the internuclear distance between the colliding atoms must also be in the same $30 - 44.6 a_0$ range for PA to occur. The p -wave centrifugal barrier at $\sim 100 a_0$ inhibits atoms from getting close enough where PA occurs, restricting collisions primarily to $l = 0$ (s -wave). Thus, in accordance with the angular momentum selection rules mentioned above, the photoassociation of colliding (s -wave) Li and Rb atoms can lead to the formation of LiRb* molecules in the following states: $\Omega = 0^+$ ($J = 0, 1, 2$), $\Omega = 0^-$ ($J = 0, 1, 2$) and $\Omega = 1$ ($J = 1, 2$). In light of the preceding discussion, it is expected that up to three rotational levels would be observed but we observe only one rotational level for each vibrational level. The absence of rotational structure is unexplained at present and makes our rotational assignment somewhat ambiguous. We assign $J = 1$ for all observed levels, against $J = 0$ or $J = 2$, taking into consideration the fact that there are at least twice as many allowed PA transitions from the $1(0^+)$, $1(0^-)$ and $1(1)$ collision channels that could lead to the formation of $J = 1$ molecules in the excited states. We have recently confirmed the assignment of $J = 1$ using Raman-type two-photon

photoassociation, the details of which are discussed in chapter 5. The assignments are reported in table 4.2.

Table 4.2. The values of $-\Delta_{PA}$ (in GHz) for which PA resonances are observed below the Li ($2s\ ^2S_{1/2}$) + Rb ($5p\ ^2P_{1/2}$) asymptote. Also included is the assignment of the electronic states and the vibrational quantum numbers ν (measured from dissociation limit). For vibrational levels with multiple internal structures, the frequency of line closest to the center of the spectrum is reported. We did not observe the next more deeply bound vibrational state probably due to weak Franck-Condon overlap with the scattering state. The least bound states (bound by less than 8 GHz) could not be observed because the PA laser, with frequency close to D_1 transition, strongly perturbed the operation of the Rb MOT.

State	$\nu = 2$	$\nu = 3$	$\nu = 4$	$\nu = 5$
2(0 ⁺)	9.45	38.08	98.44	
2(0 ⁻)		15.48	51.08	119.23
2(1)		16.28	52.56	121.44

4.3.2 C_6 coefficients for the Li ($2s\ ^2S_{1/2}$) + Rb ($5p\ ^2P_{1/2}$) asymptote

As stated earlier, the electronic potentials at such large internuclear separations (R) are almost entirely determined by the C_6 coefficients, which can be extracted using the LeRoy-Bernstein (LRB) formula⁹⁸:

$$D - E_\nu = A_6(\nu - \nu_D)^3 \quad (4.1)$$

where ν is the vibrational quantum number (measured from the dissociation limit), ν_D is vibrational quantum number at dissociation such that $0 < \nu_D < 1$, $-(D - E_\nu)$ is the (negative) binding energy (E_B), E_ν is the energy of the ν^{th} vibrational level, D is the dissociation energy and $A_6 = 16\sqrt{2}\pi^3\hbar^3/[B(2/3, 1/2)\mu^{3/2}C_6^{1/2}]$. Here μ (= 6.48 atomic mass unit) is the reduced mass of $^7\text{Li}^{85}\text{Rb}$ and B is the Beta function [$B(2/3, 1/2) = 2.5871$]. The experimentally measured quantity is Δ_{PA} which is related to the binding

energy according to the relation $(D - E_\nu) - E_{rot} = -h\Delta_{PA}$, where $E_{rot} = B_\nu[J(J+1) - \Omega^2]$ is the rotational energy. We initially ignore the rotational energy and plot $(-h\Delta_{PA})^{1/3} \approx (D - E_\nu)^{1/3}$ against ν and, from a fit to equation (4.1), derive the values of ν_D and A_6 (and hence C_6). The fits for different electronic states are shown in Figure 4.3.

In order to account for the rotational energy E_{rot} , the following procedure is used. The electronic potential is written in the form $V(R) = -C_6/R^6$, with the C_6 coefficients derived above. At the outer turning point R_{out} of the ν^{th} vibrational level $V(R_{out}) = -(D - E_\nu) \approx h\Delta_{PA}$, which implies that $R_{out} \approx (-C_6/h\Delta_{PA})^{1/6}$ (R_{out} lies in the range 30 – 44.6 a_0 depending on ν). The rotational constant is then approximated as $B_\nu \approx \hbar^2/2\mu R_{out}^2$ and these values lie in the range 140 – 310 MHz depending on ν . The value of E_{rot} is then calculated and the correction due to E_{rot} is taken into account by plotting $(-h\Delta_{PA} + E_{rot})^{1/3}$ against ν , and deriving a new set of the values of ν_D and A_6 (and hence C_6). We find that the new set of values of ν_D and C_6 are very close to the initial value and the values are reported in table 4.3. We also found that, the uncertainties (± 1) in the assignment of J , as mentioned above, does not affect the values of ν_D and C_6 extracted and they lie within the quoted uncertainties. Table 4.3 also includes a comparison of the experimentally determined C_6 coefficients and different theoretically calculated values. We find good agreement with the values reported in ref. 88 and reasonable agreement with ref. 89. The agreement with ref. 90 is not good because their calculations neglected the fine structure of atoms (that distinguishes the D_1 and D_2 asymptotes).

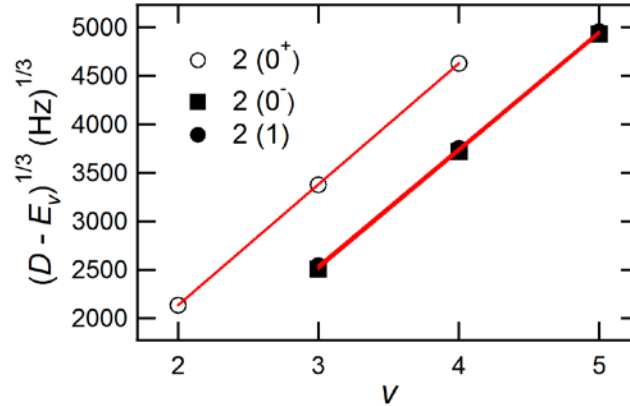


Figure 4.3. The fit of experimentally observed PA frequencies to the LRB formula as described in the text. Note that the data points for the $2(0^-)$ and $2(1)$ states lie almost on top of each other. Also note that the slopes of all the curves are similar indicating that the C_6 coefficients for all three electronic states are similar.

Table 4.3. The values of C_6 coefficients (in atomic units = Hartree/ $a_0^6 \approx 0.957342 \times 10^{-79} \text{ Jm}^6$) for the Li ($2s \ ^2S_{1/2}$) + Rb ($5p \ ^2P_{1/2}$) asymptote measured experimentally in this work, and a comparison with three different theoretical predictions. The superscripts and subscripts on the experimental values indicate the uncertainties that arise when J is changed by ± 1 . The experimentally determined values of ν_D are also included.

State	This work		Ref. 88	Ref. 89	Ref. 90
	C_6	ν_D	C_6	C_6	C_6
$2(0^+)$	11335^{+600}_{-300}	0.288	13900	16072	$^{1,3}\Sigma^+$:
$2(0^-)$	13470^{+540}_{-270}	0.927	13900	16071	26744
$2(1)$	13730^{+535}_{-135}	0.893	13900	16071	$^{1,3}\Pi$: 9431

4.4 Photoassociation below the Li ($2s \ ^2S_{1/2}$) + Rb ($5p \ ^2P_{3/2}$) asymptote

A part of the experimentally observed PA spectrum below the Li ($2s \ ^2S_{1/2}$) + Rb ($5p \ ^2P_{3/2}$) asymptote is shown in Figure 4.4. The detuning Δ_{PA} is measured with respect to the frequency ν_{res} ($= 384232.157 \text{ GHz}$) of the Rb ($5s \ ^2S_{1/2}, F = 2$) \rightarrow Rb ($5p \ ^2P_{3/2}, F' = 3$) transition, i.e. $\Delta_{PA} = \nu_{PA} - \nu_{res}$, where ν_{PA} is the frequency of the PA laser. The detuning

Δ_{PA} is thus a measure of the binding energy (E_B) of the respective vibrational levels. For the spectrum shown in Figure 4.4, the frequency of the PA laser was scanned slowly at 10 MHz/s and the average intensity of the PA beam was 70 W/cm². The full spectrum in Figure 4.4 was obtained by stitching together several short 4 GHz scans. Figures 4.5 and 4.6 show the zoom in on each observed PA peak so that the internal structure in the lines can be appreciated (these spectra were taken at different PA intensities and different scan speeds and hence the PA line strengths in different panels should not be directly compared).

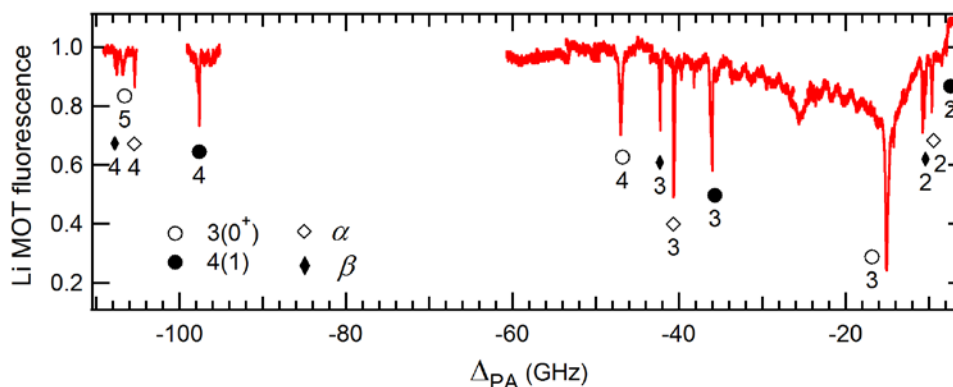


Figure 4.4. PA spectra of LiRb below the Li ($2s\ ^2S_{1/2}$) + Rb ($5p\ ^2P_{3/2}$) asymptote obtained using trap loss spectroscopy. The filled circles, open circles, open rhombus and filled rhombus indicate lines belonging to the $4(1)$, $3(0^+)$, α and β states, respectively, while the numbers indicate the vibrational level ν measured from the dissociation limit (see text for details).

4.4.1 Assignment of spectra below the Li ($2s\ ^2S_{1/2}$) + Rb ($5p\ ^2P_{3/2}$) asymptote

We assign the PA spectra below the Li ($2s\ ^2S_{1/2}$) + Rb ($5p\ ^2P_{3/2}$) asymptote using the same method discussed in section 4.3. We assign the relatively wide (~ 250 MHz) PA lines to $3(0^+)$, $J = 1$ since (i) the linewidth of $3(0^+)$ resonances are expected to be large because the $3(0^+)$ state, which correlates to the $b\ ^3\Pi - A\ ^1\Sigma^+$ complex at small internuclear

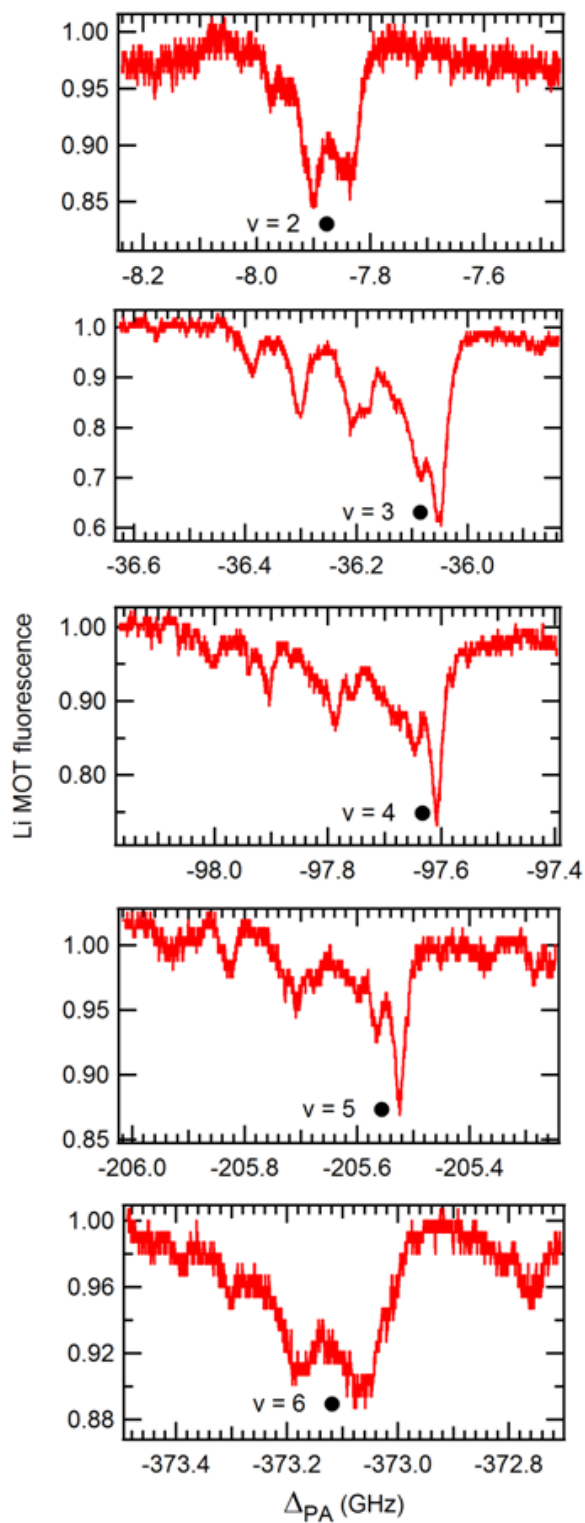


Figure 4.5. The PA spectra of all the 4(1) states observed in this thesis. The vibrational number ν (measured from dissociation) is also labeled.

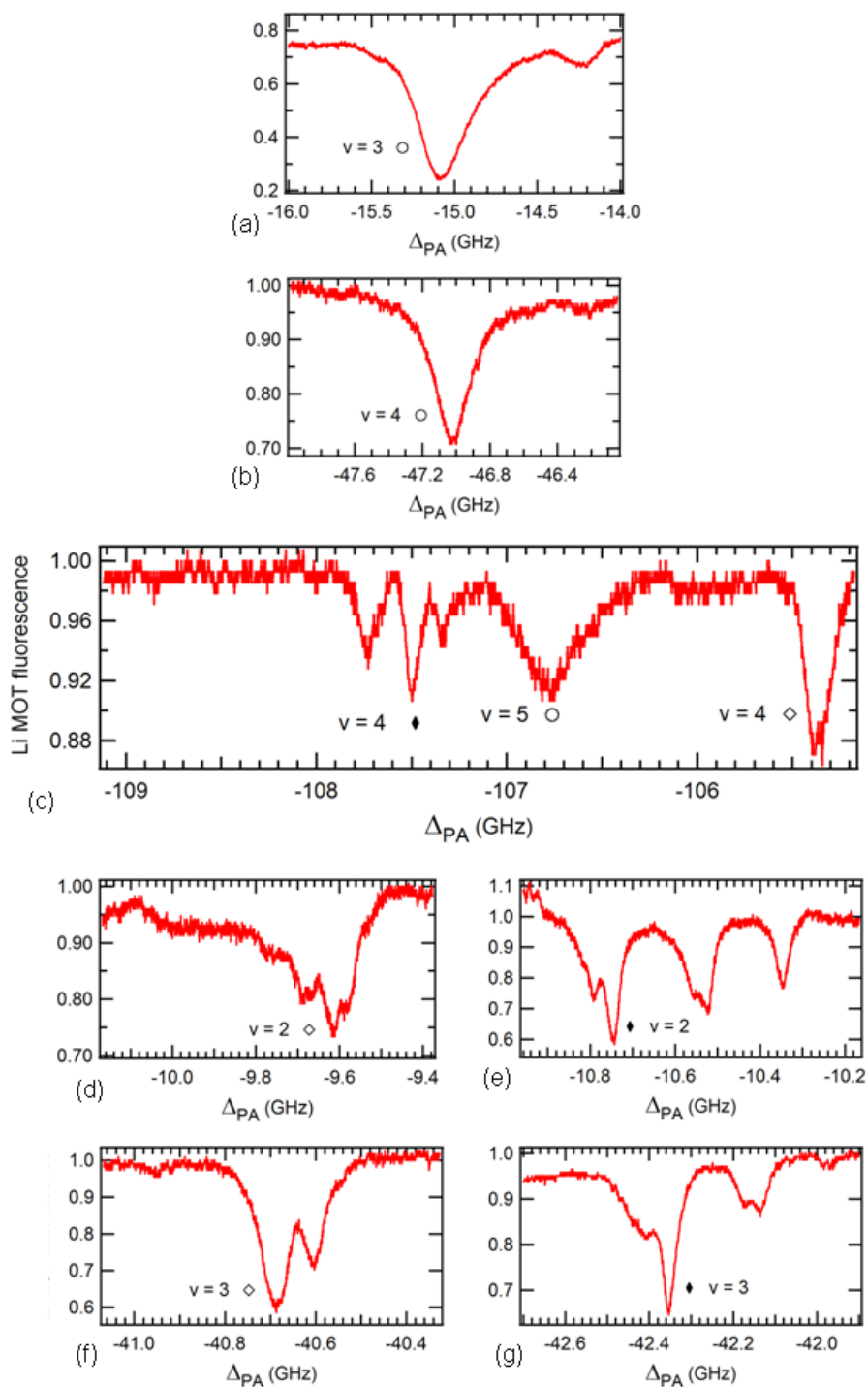


Figure 4.6. PA spectra for the $3(0^+)$ state (open circles), the α state (open rhombus) and β state (filled rhombus). In panel (a), the weaker peak ~ 800 MHz to right of the main peak arises from collision along the the Li ($2s\ ^2S_{1/2}$, $F=1$) + Rb ($5s\ ^2S_{1/2}$, $F=2$) channel due to imperfect hyperfine repumping in the Li MOT.

distances, could undergo predissociation⁹⁵ due to the avoided crossing⁶⁰ between the b $^3\Pi$ and A $^1\Sigma^+$ states, (ii) they are expected to have no hyperfine structure, and (iii) they fit the expected line positions of the triad potential quite well as discussed in details below. We assign the lines with multiple resolved hyperfine splitting to 4(1), $J = 1$ since (i) the hyperfine splitting is expected to be the largest for these lines⁹⁹ and (ii) they fit the diad potential quite well. There are some other PA lines which follow a LRB trend but we are unable to assign them accurately. We label them as α and β instead. The assignments are reported in Table 4.4.

Table 4.4. The values of $-\Delta_{PA}$ (in GHz) for which PA lines are observed below the Li ($2s$ $^2S_{1/2}$) + Rb ($5p$ $^2P_{3/2}$) asymptote. Also included are the assignments of the electronic states and the vibrational quantum numbers ν (measured from dissociation limit).

State	$\nu = 2$	$\nu = 3$	$\nu = 4$	$\nu = 5$	$\nu = 6$
4(1)	7.91	36.06	97.61	205.52	373.07
3(0^+)		15.08	47.03	106.76	
α	9.62	40.69	105.36		
β	10.75	42.36	107.50		

4.4.2 C_6 coefficients for the Li ($2s$ $^2S_{1/2}$) + Rb ($5p$ $^2P_{3/2}$) asymptote

The C_6 coefficients for Li ($2s$ $^2S_{1/2}$) + Rb ($5p$ $^2P_{3/2}$) asymptote are found using the LeRoy-Bernstein (LRB) formula as discussed in section 4.3. The fit to the LRB formula is shown in Figure 4.7 and the values of the C_6 coefficients for the Li ($2s$ $^2S_{1/2}$) + Rb ($5p$ $^2P_{3/2}$) asymptote are reported in Table 4.5. It is interesting to note that we find three states, α , β and 4(1), have similar and lower C_6 coefficients of ~ 10000 a.u.. This is contrary to theory^{88,89} where only two states, 4(1) and 1(2), have C_6 coefficients of ~ 10000 a.u. while three states, 3(0^+), 3(0^-) and 3(1), have C_6 coefficients of ~ 20000 a.u..

Note added just before the thesis was submitted: It was later realized, using a more rigorous calculation of the rotational constants, that the α and β lines could be due to the $J = 2$ and $J = 1$ levels of the $4(1)$ state, respectively. The values of C_6 coefficient and ν_D are determined to be 10190 a.u. and 0.244, respectively. This would also imply that the state labeled $4(1)$ in Figure 4.5 (and in the rest of the thesis) is actually the $1(2)$ state with $J = 2$. Most of the discussions in the thesis would be unaffected by this change.

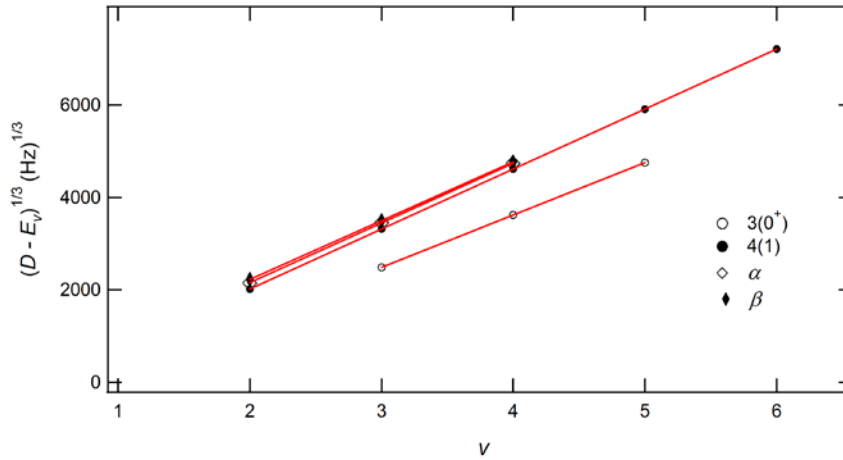


Figure 4.7. The fit to the LRB formula that is used to extract the C_6 coefficients from the experimentally measured PA line positions. The data points and fits for the states α , β and $4(1)$ lie almost on top of each other.

Table 4.5. The values of C_6 coefficients (in atomic units) for the Li ($2s\ ^2S_{1/2}$) + Rb ($5p\ ^2P_{3/2}$) asymptote measured experimentally in this work, and a comparison with three different theoretical predictions. The superscripts and subscripts on the experimental values indicate the uncertainties that arise when J is changed by ± 1 . The experimentally determined values of ν_D are also included.

State	This work		Ref. 88	Ref. 89	Ref. 90
	C_6	ν_D	C_6	C_6	C_6
4(1)	8910^{+340}_{-170}	0.444	9205	11308	$^{1,3}\Sigma^+$: 26744
3(0 ⁺)	20160^{+940}_{-470}	0.801	20670	24980	
α	9110^{+500}_{-250}	0.334	or 20670	or 24980	$^{1,3}\Pi$: 9431
β	10180^{+520}_{-260}	0.243			

4.5 Strength of photoassociation transitions

The strength S ($\propto I^{1/2} \langle b | \vec{d} \cdot \vec{e} | sc \rangle$) of PA transitions at a fixed PA laser intensity I is mainly driven by the Franck-Condon (FC) overlap⁴³, i.e. the overlap of the wave function of the excited electronic state $|b\rangle$ with that of the scattering state of two free atoms $|sc\rangle$. As shown schematically in Figure 4.8, the amplitude of the wave function of the scattering state increases rapidly at higher inter-nuclear separation. Similarly, the wave function for a bound state molecule has the largest amplitude near the outer turning point (R_{out}) of the excited state potential. Because of the rapid oscillatory behavior of the wave functions at small inter-nuclear distances, the FC overlap and hence the strength of PA is predominantly determined by the overlap near the last lobe of the excited state wave function i.e. near the outer turning point of the excited state potential. Clearly, good PA strength is expected for high lying vibrational levels of the excited state for which the outer turning points lie at large inter-nuclear separations.

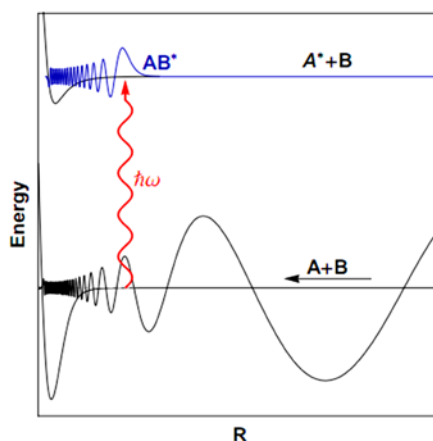


Figure 4.8. Schematic representation of the initial low-energy scattering radial wave function and the final bound vibrational wave function.

All the PA levels reported in this thesis have outer turning point at large inter-nuclear separation (R) for which the electronic potentials are determined primarily by the C_6 coefficients i.e. $V(R) = -C_6/R^6$. It was shown theoretically¹⁰⁰ that the free-bound FC overlap for these loosely bound states is proportional to $\mu^{9/4} (C_6)^{3/4}$, where μ is the reduced mass of the molecule. Among heteronuclear bi-alkali molecules, LiRb has relatively small values of μ and C_6 and thus the strength of PA transitions in LiRb is expected to be small compared to most other heteronuclear bi-alkali molecules (Figure 4.9). A later theoretical calculation¹⁰¹ reported that the PA rates of different heteronuclear bi-alkali molecules differ by a factor of ~ 5 and not by a factor of 100 or more as reported in ref. 100. The theoretically calculated PA rates of ref. 101 are shown in Figure 4.10. In our experiment, we find that the PA rate in LiRb is actually the highest among all reported values for heteronuclear bi-alkali molecules, suggesting that the full quantum mechanical numerical calculations of ref. 101 better describe the PA process.

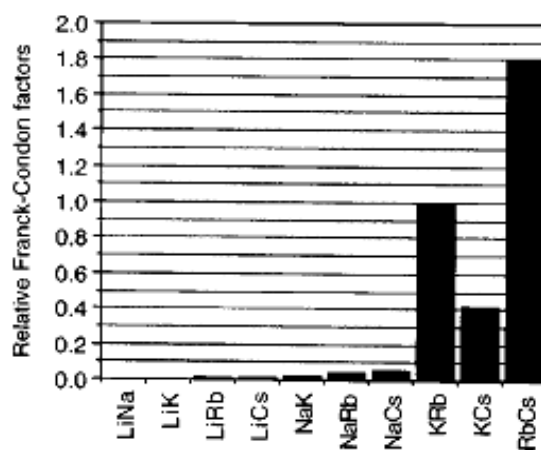


Figure 4.9. The relative values of Franck-Condon factors for heteronuclear photoassociation transitions at long range calculated based on reflection approximation. These calculations deviate significantly from experimental observations for LiRb. The figure is adapted from ref. 100.

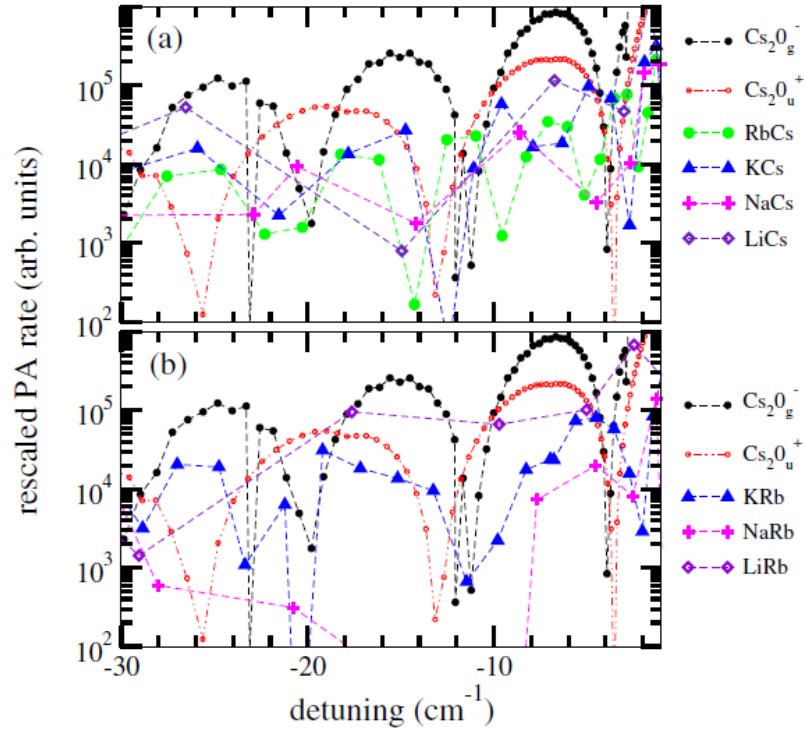


Figure 4.10. Rescaled PA rates (when atoms collide along the $X \ ^1\Sigma^+$ potential) for (a) Cs compounds and (b) Rb compounds, for the $X \ ^1\Sigma^+ \rightarrow 0^+$ ($A \ ^1\Sigma^+$) transition as a function of the detuning of the PA laser below the Li ($2s \ ^2S_{1/2}$) + Rb ($5p \ ^2P_{1/2}$) or analogous asymptotes. Single channel calculations and coupled channel calculations (with spin-orbit coupling included) resulted in similar PA rates. The figure is adapted from ref. 101.

4.6 Measurement of photoassociation rate in LiRb

We measure the photoassociation rate (\propto PA strength $S \times$ atomic density n) from the time evolution of the number of atoms in the Li MOT when the resonant PA beam is shone on the MOT. We focus our attention to the strongest PA line, the $\nu = 3$ level of the $3(0^+)$ state) at $\Delta_{PA} = -15.08$ GHz ($\nu_{PA} = 384217.07$ GHz) with respect to the Li ($2s \ ^2S_{1/2}$) + Rb ($5p \ ^2P_{3/2}$) asymptote, for which we observe 70% losses in the Li MOT. In Figure 4.11 we show the time evolution of the number of atoms in the Li MOT when the resonant PA beam, with different average intensities (some of which saturate the transition, see below),

is turned on at $t = 0$. From the initial slope of the curve, we determine that 3.5×10^7 Li atoms are lost per second. This implies a LiRb* production rate (P_{LiRb}) of $3.5 \times 10^7 \text{ s}^{-1}$, which is among the highest observed for heteronuclear bi-alkali molecules. When comparing the PA rates of different species, it is often more instructive to compare the PA rate per atom. For LiRb, the maximum value we observe is 0.35 s^{-1} per atom. This can be compared with the experimentally measured value of $\sim 0.38 \text{ s}^{-1}$ per atom for RbCs (below the Rb ($5s \ ^2S_{1/2}$) + Cs ($6p \ ^2P_{1/2}$) asymptote) and 0.07 s^{-1} per atom for LiK (below the Li ($2s \ ^2S_{1/2}$) + K ($4p \ ^2P_{3/2}$) asymptote). The observed PA rate for LiRb is comparable to RbCs which is contrary to the prediction of ref. 100 (Figure 4.9). We also note that the PA rates for strongest lines of the 4(1) or the unassigned states of LiRb are comparable (within a factor of 2) to that of the $\nu = 3$ level of the $3(0^+)$ state, as is evident from the relative intensity of the PA lines in Figure 4.4.

We also measured the PA rate for the strongest line below the Li ($2s \ ^2S_{1/2}$) + Rb ($5p \ ^2P_{1/2}$) asymptote, the $\nu = 3$ level of the $2(0^+)$ state. We found $P_{LiRb} \sim 10^7 \text{ s}^{-1}$ and the corresponding value per atom to be $\sim 0.2 \text{ s}^{-1}$ per atoms (due lower PA laser intensity available at the time of the experiment, the transition was not completely saturated). We see that the PA rate is again comparable to RbCs. In ref. 101, the authors calculated the relative PA rates for several molecules below the $^2S_{1/2} + ^2P_{1/2}$ asymptotes. According to ref. 101, the PA rates for LiRb and RbCs are expected to be comparable which is in decent, but not perfect, agreement with experiments. We believe that calculations with experimentally determined potentials may improve the agreement between theory and experiments.

We calculate the PA rate coefficient K_{PA} which, for a small Li MOT immersed in a larger Rb MOT, is simply given by: $K_{PA} = P_{LiRb}/(n_{Rb}N_{Li})$. For the measurement of K_{PA} , we thus intentionally load a much smaller Li MOT inside a large Rb MOT (such that the Li MOT is completely immersed in the Rb MOT). Using the values of P_{LiRb} , N_{Li} and n_{Rb} , we then calculate the PA rate coefficient K_{PA} for the strongest PA lines near the D_1 and D_2 asymptotes. The maximum value that we obtain is $K_{PA} = 1.3 \times 10^{-10} \text{ cm}^3/\text{s}$ for the $v = 3$ level of the $3(0^+)$ state. The value of K_{PA} is accurate to within 50%, the major uncertainty coming from the determination of n_{Rb} (note that the uncertainties in the measurement of N_{Li} cancel out). We also observe the saturation of P_{LiRb} , and hence K_{PA} , for PA laser intensities exceeding $60 \text{ W}/\text{cm}^2$ (Figure 4.11). For this level, we quote a saturated PA rate coefficient K_{PA} of $1.3(7) \times 10^{-10} \text{ cm}^3/\text{s}$.

This value can be compared to the predicted theoretical value at the unitarity limit where the scattering matrix element becomes unity^{43,103,104}:

$$K_{PA,unitarity} = \pi v_{rel}/k^2 = \hbar^2 \sqrt{2\pi/\mu^3 k_B T} = 2.1 \times 10^{-10} \text{ cm}^3/\text{s},$$

where $v_{rel} = \sqrt{8k_B T/\pi\mu}$ is average relative velocity of the atoms, $k = \sqrt{2\mu k_B T/\hbar^2}$, μ is the reduced mass and $T = 1 \text{ mK}$ is the temperature of the Li atoms. Given the uncertainty in the values of n_{Rb} and T , we consider that the agreement between experiment and theory is excellent. We note that we performed a similar analysis for PA of $^{85}\text{Rb}_2$ we measured and found good agreement with theory¹⁰³ and with previous experimental reports.

This is the first time that unitarity limited saturation of K_{PA} has been observed for heteronuclear polar molecules. This has important implications, for example, in the observation of atom-molecule oscillations and in coherent control (which often requires

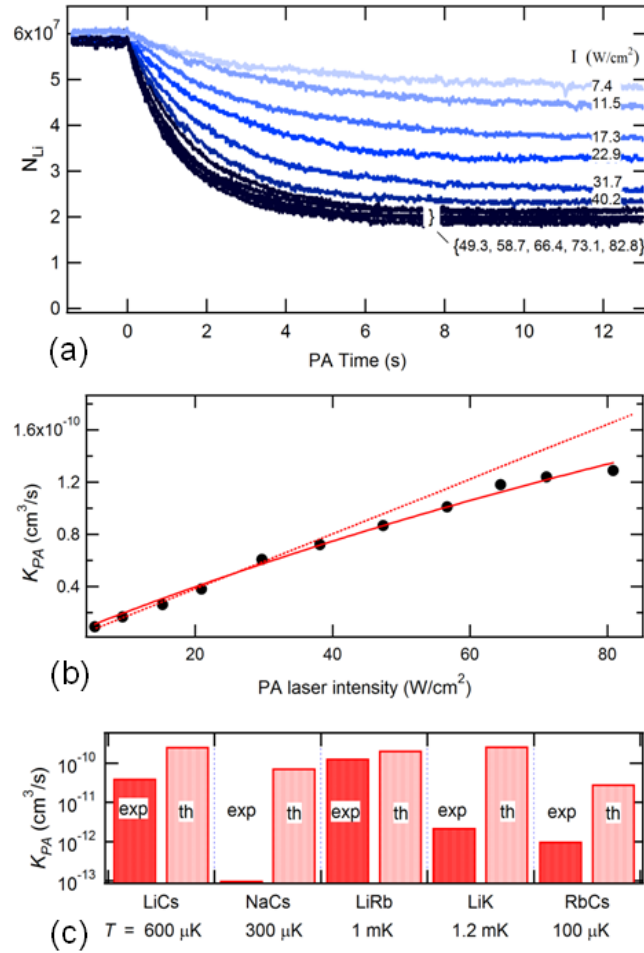


Figure 4.11. (a) The evolution of the atom number N_{Li} in the Li MOT when the on resonance PA light ($\nu_{PA} = 384217.07$ GHz, for the $v = 3$ level of the $3(0^+)$ state) is turned on at $t = 0$. The $LiRb^*$ production rate (P_{LiRb}) is estimated from the slope near $t = 0$. The saturation of P_{LiRb} is clearly visible for intensities (I) beyond $60 W/cm^2$. (b) The PA rate coefficient (K_{PA}) as a function of the average PA laser intensity. The rate starts to saturate beyond $60 W/cm^2$. The dotted line is a linear fit of K_{PA} in the low-intensity regime with a slope $2 \times 10^{-12} (cm^3/s)/(W/cm^2)$. The solid line is a fit of K_{PA} to the equation¹⁰² $K_{PA} = 4K_{PA,max} / (1 + I_{sat} / I)$ with $K_{PA,max} = 1.6(\pm 0.5) \times 10^{-10} cm^3/s$ and $I_{sat} = 300 \pm 100 W/cm^2$. (c) Comparison of PA rate coefficient K_{PA} of different polar molecules. The left (dark color, exp) bars denote the maximum experimentally observed values of K_{PA} while the right (light color, th) bars denote the theoretical values at the unitarity limit at the temperatures indicated. Even at a relatively high temperature, the K_{PA} for LiRb is the highest and is close to the theoretical prediction of the unitarity limit.

understanding the strongly driven regime). In Figure 4.11c we plot the maximum observed K_{PA} values for different polar molecules along with the theoretical values at the unitarity limit. It is seen that the experimentally observed K_{PA} value for LiRb is higher than all species so far and approaches the unitarity limit. We note that K_{PA} can be further increased by lowering T . It is also seen that for most other species the experimental maximum values differ substantially from the values at the unitarity limit. Moreover, the measured K_{PA} values for LiCs¹⁰⁵ and NaCs¹⁰⁶ have large error bars and are only accurate within a factor of 10. The error bars are large in those measurements because the measurements were performed using Resonance Enhanced Multi-Photon Ionization (REMPI) for which it is difficult to calibrate the ionization, ion collection and detection efficiencies. No PA-induced trap loss could be observed in LiCs and NaCs, possibly indicating that the PA rates are much lower than LiRb. PA induced trap loss was observed in RbCs¹⁰⁷ and LiK⁹⁶ but the PA rate coefficients were significantly lower. In this regard, LiRb is a welcome exception with very high PA rate and the observation of PA-induced trap loss allows relatively precise determination of the PA rate coefficient K_{PA} .

4.7 Prediction of ground state molecule formation

We observe a very high LiRb* molecule production rate (P_{LiRb}) of $3.5 \times 10^7 \text{ s}^{-1}$ for the $v = 3$ level of the $3(0^+)$ state, while the rates for the strongest PA lines in other electronic states are comparable (within a factor of two). Assuming that a small fraction of the LiRb* molecules would spontaneously decay to electronic ground state LiRb molecules, this amounts to a substantial production rate of LiRb molecules in the electronic ground

state. For example, the observed $v = 6$ level of the $4(1)$ state has outer turning point R_{out} at $\sim 23.2 a_0$ and from theory^{59,60} the inner turning point R_{in} is $\sim 5.7 a_0$. A vertically downward transition at R_{in} would create $X^1\Sigma^+$ ($v'' \sim 5$) molecules which also have $R_{in} \sim 5.7 a_0$ (v'' and v' denote vibrational quantum numbers measured from the bottom of the ground and excited state potentials respectively). The actual branching ratio can be measured using REMPI and, in fact, from our previous spectroscopy work⁵⁷, we find that the $B^1\Pi$ ($v' = 13$) state is a promising intermediate state for the detection of LiRb molecules produced in the $X^1\Sigma^+$ ($v'' \sim 5$) state. Efforts in this direction have already started in our laboratory. In the rest of this section, we argue that LiRb molecules in the $X^1\Sigma^+$ ($v'' = 0$) state can be efficiently formed by photoassociating to the levels of the $4(1)$ state observed in this thesis. We further argue that one may not gain anything in terms of ground state molecule formation rate by photoassociating to more deeply bound levels, unless there is resonant coupling or mixing between different electronic states.

The efficient production of ground $X^1\Sigma^+$ ($v'' = 0$) state molecules requires the following properties of the photo-associated state in the electronically excited potential: (i) the outer turning point should be at large inter-nuclear separation and (ii) the inner turning point should be at the same inter-nuclear distance as the equilibrium inter-nuclear distance R_{eq} ($= 6.55 a_0$) of the $X^1\Sigma^+$ ($v'' = 0$) state. Unfortunately, in LiRb these two requirements are not simultaneously fulfilled by any level, although there are numerous excited electronic states which satisfy one of these requirements. As an example, two states which fulfill the second requirement quite well are: (a) $v' \sim 15$ level of the $C^1\Sigma^+$ state and (b) $v' = 2$ and $v' = 3$ levels of the $B^1\Pi$ state, as discussed in section 2.5.

However, the strength of the PA transition to these levels are quite low, decreasing the efficiency with which LiRb molecules in the $X^1\Sigma^+(v''=0)$ state can be created.

In order to find the most efficient pathway for the creation of ground state molecules it is instructive to compare the product (η) of the following two quantities: (i) the strength of the PA transition, which is determined by the free-bound FC overlap between the wave function of the scattering state and the wave function of the PA level, and (ii) the strength of spontaneous emission from the PA level to different vibrational levels of the ground state, which is determined by the bound-bound FC overlap (Figures 4.12 and 4.13).

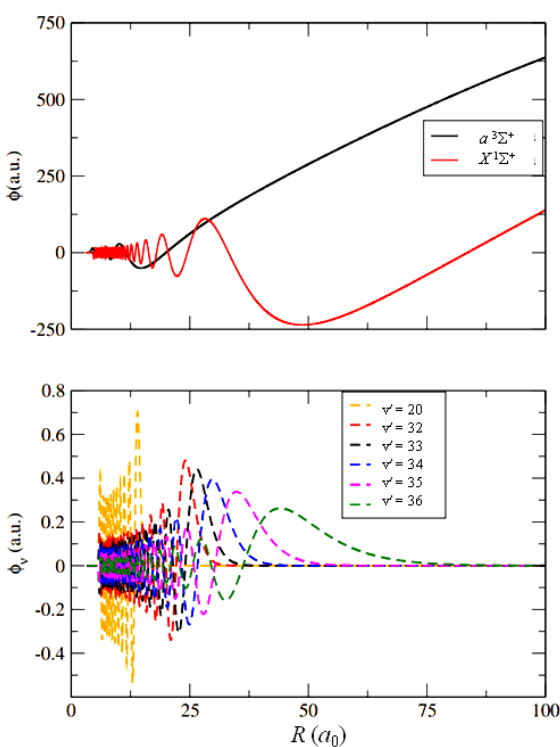


Figure 4.12. Top panel: The wave function of the scattering state. The red line is for scattering along the $X^1\Sigma^+$ potential and the black line is for scattering along the $a^3\Sigma^+$ potential. Bottom panel: The wave function for different vibrational levels (v') of the $B^1\Pi$ state. All level shown in this figure, except $v' = 20$, have been observed experimentally using PA. Calculation and figure courtesy: Jesús Pérez-Ríos.

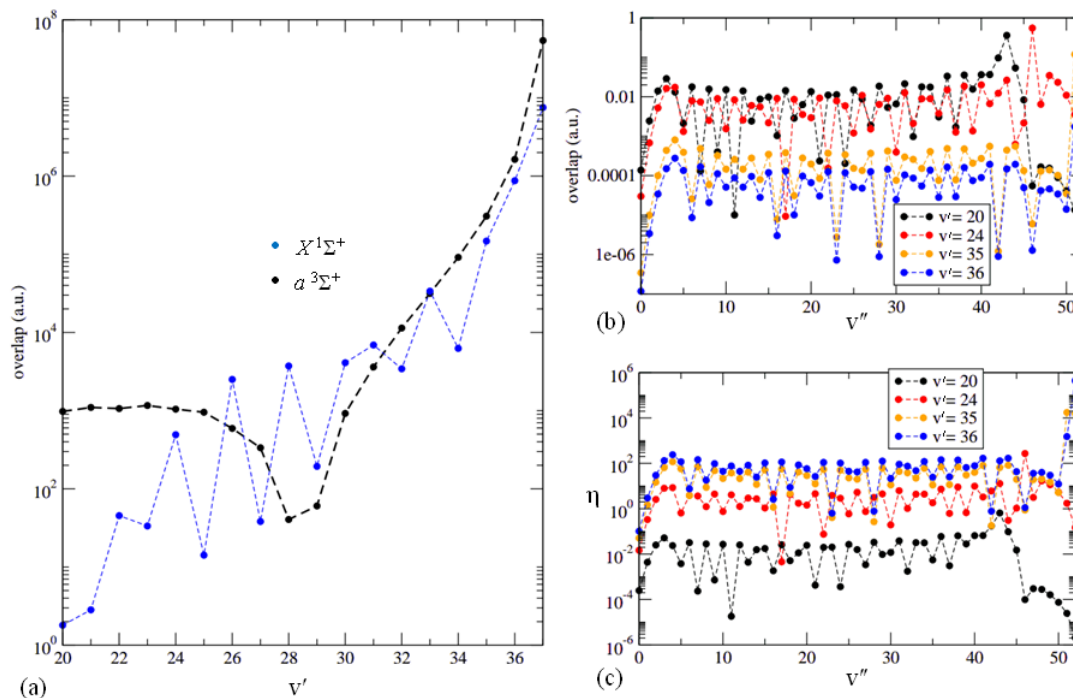


Figure 4.13. (a) The free-bound FC overlap between the scattering state (scattering along the $X^1\Sigma^+$ and the $a^3\Sigma^+$ potentials) and the different vibrational levels (v') of the $B^1\Pi$ state. (b) Bound-bound FC overlap between different vibrational levels (v') of the $B^1\Pi$ state and the different vibrational levels (v'') of the $X^1\Sigma^+$ state (plotted along the abscissa). We note that the calculation is in qualitative agreement with our LIF data for $v' = 20$. (c) The plot of molecule production efficiency η in different vibrational levels (v'') of the $X^1\Sigma^+$ state for PA to a few different vibrational levels (v') of the $B^1\Pi$ state, assuming that atoms collide along the $X^1\Sigma^+$ potential. Calculation and figure courtesy: Jesús Pérez-Ríos.

In Figure 4.13c we plot the product η for PA to the $v' = 20, 24, 35$ and 36 levels of the $B^1\Pi$ state which corresponds to the $v = 18, 14, 3$ and 2 levels (counted from the asymptote) of the $4(1)$ state at large internuclear separations (note that $v = 3$ is the strongest experimentally observed PA line of the $4(1)$ state which corresponds to the $v' = 35$ of the $B^1\Pi$ state). The numbers along the abscissa of Figure 4.13c denote the vibrational levels v'' of the $X^1\Sigma^+$ state, while along the axis we plot the values of η which is a measure of the efficiency with which molecules are produced in the respective v''

levels. It is seen that the value of η is higher for loosely bound PA levels. This indicates that photoassociating to a loosely bound level followed by spontaneous emission leads to higher rate of formation of ground $X^1\Sigma^+$ state molecules. However, very few molecules are produced in the $v'' = 0$ level of the $X^1\Sigma^+$ state.

In order to roughly estimate the ground state molecule formation rate let's choose PA to $v = 3$ level of the $4(1)$ state. For this line, we experimentally determined the excited state LiRb* formation rate to be $\sim 2 \times 10^7 \text{ s}^{-1}$. Some of these LiRb* molecules would dissociate to form free Li and Rb atoms but some spontaneously emit a photon to form LiRb molecules in the ground $X^1\Sigma^+$ state (indeed, we have observed these electronic ground state molecules using REMPI). Assuming that 20% of the LiRb* molecules spontaneously emit to form molecules in different v'' levels of the ground $X^1\Sigma^+$ state, we estimate that $\sim 4 \times 10^6 \text{ s}^{-1}$ ground state molecules are formed (this assumption leads to the largest uncertainty in the estimate). Among these, around 45% would populate the $v'' = 52$ level and around 0.35% would populate the $v'' = 4$ levels (estimated from FC overlaps), leading to formation of $\sim 1.8 \times 10^6$ and $\sim 1.4 \times 10^4$ molecules per second in the $v'' = 52$ and $v'' = 4$ levels respectively.

The molecules in $v'' = 4$ level can be transferred to $v'' = 0$ level by exciting the molecules in the $v'' = 4$ level to the $v' = 2$ of the $B^1\Pi$ state (Figure 4.14a). Around 25% of the molecules in the $v' = 2$ of the $B^1\Pi$ state would decay to $v'' = 0$ level of the $X^1\Sigma^+$ state (see section 2.5), producing $\sim 3.5 \times 10^3$ molecules per second in the $v'' = 0$ level of the $X^1\Sigma^+$ state. The estimate is made assuming that only $\sim 5 \times 10^7$ Li/Rb atoms are trapped in the MOT. It is relatively easy to increase the number of trapped atoms in the MOT by a factor of ten (we have done this in our apparatus too). This would increase the ground X

$^1\Sigma^+$ ($v'' = 0$) state molecule formation rate to $3.5 \times 10^4 \text{ s}^{-1}$, which is extremely promising for future experiments.

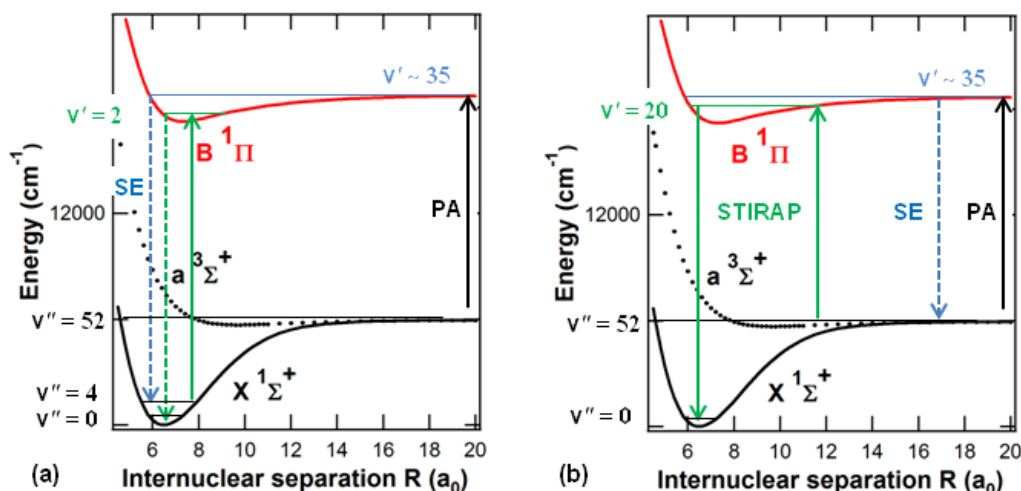


Figure 4.14. The schemes that can be used to transfer LiRb molecules to the X ¹Σ⁺ ($v'' = 0$) state. (a) Scheme involving PA followed by spontaneous emission (SE) only. (b) Scheme involving PA followed by SE, followed by STIRAP. See text for details.

The overall efficiency is much higher if the LiRb molecules are transferred to the X ¹Σ⁺ ($v'' = 0$) state by more sophisticated techniques like STIRAP^{108,109}. It is especially impressive if the 1.8×10^6 molecules produced per second in the $v'' = 52$ level are transferred to the $v'' = 0$ level of the X ¹Σ⁺ state (Figure 4.14b). Preliminary theoretical estimates indicate that this is certainly feasible (with the $v' = 20$ level of the B ¹Π state being used as the intermediate state for the state transfer). Even if the STIRAP efficiency is relatively low (~50%), we expect that $\sim 10^6$ molecules produced per second in the $v'' = 0$ level of the X ¹Σ⁺ state which is unprecedented among bi-alkali molecules.

I would like to note that the scheme can also be used with PA below the Li ($2s^2S_{1/2}$) + Rb ($5p^2P_{1/2}$) asymptote. The benefit of using PA below this asymptote is that these

lines do not undergo predissociation and it is thus expected that more ground state molecules are formed by spontaneous emission. As explained in the next chapter, we have observed using 2-photon PA that these excited state molecules have good FC overlap with ground state molecules. As an example, we observed that the $\nu = 4$ level of the $2(0^+)$ state has good overlap with the $\nu'' = 51$ level of the $X^1\Sigma^+$ state. Thus, a large fraction of the molecules photoassociated to the $\nu = 4$ level of the $2(0^+)$ state would spontaneously decay to the $\nu'' = 51$ level of the $X^1\Sigma^+$ state. These molecules can be transferred to the $\nu'' = 0$ level of the $X^1\Sigma^+$ state via STIRAP (with the $\nu' = 20$ level of the $B^1\Pi$ state as the intermediate state for the state transfer).

CHAPTER 5. TWO-PHOTON PHOTOASSOCIATION

In this chapter, I will discuss some results on Raman-type 2-photon photoassociation which provide very useful spectroscopic information on the least bound states of the $X^1\Sigma^+$ and the $a^3\Sigma^+$ potentials. Such experiments have been performed previously on homonuclear bi-alkali molecules^{110,111} but, to the best of our knowledge, have not been performed on heteronuclear bi-alkali molecules.

5.1 Two-photon photoassociation scheme

The scheme used for Raman-type 2-photon PA is shown in Figure 5.1. The experiment is performed in the dual-species MOT apparatus for simultaneous cooling and trapping of ^7Li and ^{85}Rb described in Chapter 3. The PA laser, with frequency ν_{PA} , is tuned to a PA transition corresponding to a the bound vibrational level (ν') below the $\text{Li}(2s^2S_{1/2}) + \text{Rb}(5p^2P_{1/2})$ asymptote of the LiRb^* molecule (* indicates electronically excited state). As described in Chapter 4, this leads to trap loss and a reduction in the number of atoms trapped in the MOTs. The frequency ν_R of a second laser, called the Raman laser, is scanned across a bound-bound transition between the vibrational level (ν') of the LiRb^* molecule and the vibrational level (ν'') of the ground-state LiRb molecule. When the frequency ν_R of the Raman laser is resonant with the bound-bound transition, it induces strong coupling between the two levels and causes shifts and splitting in their energies, a

phenomenon commonly known as the Autler-Townes splitting. Due to the shift in the energy of the ν' level of the LiRb^* molecule, the PA laser is no longer resonant with the free-bound transition and the atom loss due to PA is suppressed resulting in an increase of the MOT fluorescence which is detected using a photodiode. The frequency difference $\Delta\nu (= \nu_R - \nu_{PA})$ between the Raman and the PA laser is a measure of the binding energy (E_B) of the ν'' level of the electronic ground-state LiRb molecule.

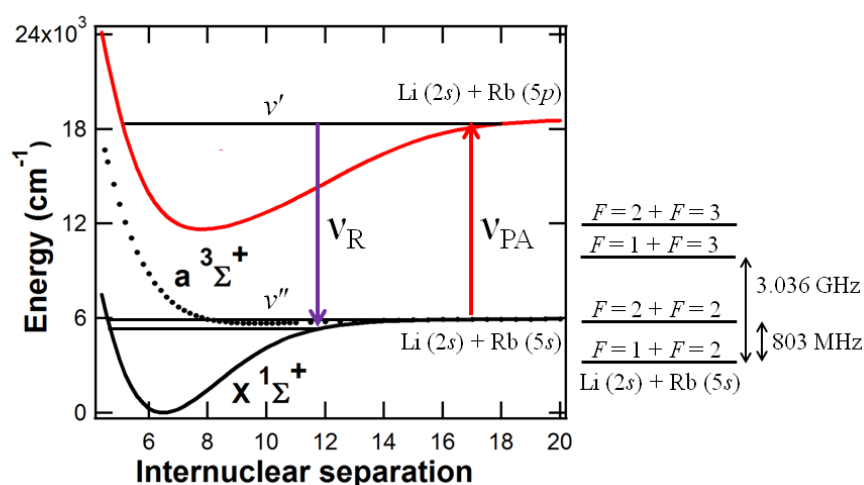


Figure 5.1. Scheme used for Raman-type 2-photon PA. The frequency ν_{PA} of the PA laser is held fixed at a free-bound PA transition which induces atom losses. The frequency ν_R of the Raman laser is scanned across a bound-bound transition. When the frequency ν_R is resonant with a bound-bound transition, the PA-induced atom losses are suppressed and an increase in MOT fluorescence is seen.

The strength of electronic transitions in molecules is determined to a large extent by the Franck-Condon overlap between the wave functions of the two levels involved. The strength of free-bound PA transition is the highest for the least bound vibrational levels (ν') of the LiRb^* molecule which have outer turning points at large internuclear separations. If such a loosely bound ν' level is used in the Raman-type 2-photon PA

scheme, then the bound-bound transition is the strongest when the ground state v'' level also has outer turning point at large internuclear separation. This makes Raman-type 2-photon PA a very useful and attractive scheme for the observation of the least bound vibrational levels of the $X^1\Sigma^+$ and $a^3\Sigma^+$ state which are difficult to observe in traditional laser spectroscopy on hot vapor phase molecules (Chapter 2).

5.2 Experiments and Results

We use a homemade external cavity diode laser (ECDL) as our PA laser. The output optical power is ~ 120 mW and the beam is collimated to a diameter of ~ 1 mm (the beam shape is asymmetric, so it is difficult to quote the intensity accurately). The ECDL is locked to a Fabry-Perot cavity which keeps the frequency of the ECDL stable within ± 5 MHz. When the frequency of the ECDL is tuned to a PA resonance, it reduces the Li MOT atom number. In Figure 5.2a we show the 1-photon PA spectrum of the $v' = 4$ level of the 2(1) state when the PA laser is scanned in the absence of the Raman laser (in this chapter, v' denotes the vibrational level of LiRb* measured from the dissociation limit). Note that this spectrum was taken with a Ti:Sapphire laser with higher optical power and hence the PA-induced loss is higher (Figure 5.2a is the same as figure 4.2g.) For the Raman-type 2-photon PA, the frequency of the PA laser is fixed at the center of the PA peak inducing $\sim 20\%$ reduction in the atom number (as inferred from the Li MOT fluorescence). Our Raman laser is a Ti:sapphire laser with a maximum output power ~ 400 mW and a beam diameter of ~ 1 mm. It co-propagates along the PA laser albeit with orthogonal linear polarization. The frequency of the Raman laser is scanned in order to obtain the Raman-type 2-photon PA spectra. In Figure 5.2b, we plot the fluorescence of

the Li MOT as a function of $\Delta\nu (= \nu_R - \nu_{PA})$. An increase in the Li MOT fluorescence is seen whenever the Raman laser is resonant with a bound-bound transition. The observed 2-photon PA resonances are labeled with Greek alphabets since complete assignments of the peaks have not been performed yet. The decrease in fluorescence at $\Delta\nu \sim \pm 3$ GHz (ground state hyperfine splitting of ^{85}Rb) is an artifact and is not related to LiRb molecules. It occurs because the PA and the Raman laser together transfer, via a Raman transition, the trapped Rb atoms from the lower $F = 2$ hyperfine level to the upper $F = 3$ hyperfine level of the $5s \ ^2S_{1/2}$ state. This disrupts the operation of the dark MOT by putting the Rb atoms in the cycling $5s \ ^2S_{1/2} (F = 3) \rightarrow 5p \ ^2P_{3/2} (F' = 4)$ transition i.e. essentially turns it to a bright MOT (or nearly so). We have seen in a previous study (Chapter 3) that a bright Rb MOT leads to severe losses in the Li MOT atom number due to light assisted interspecies collisions, explaining the origin of these features. The decrease in fluorescence at $\Delta\nu \sim 0, 0.2, 0.5$ and 1.7 GHz is due to 1-photon PA transitions induced by the Raman laser.

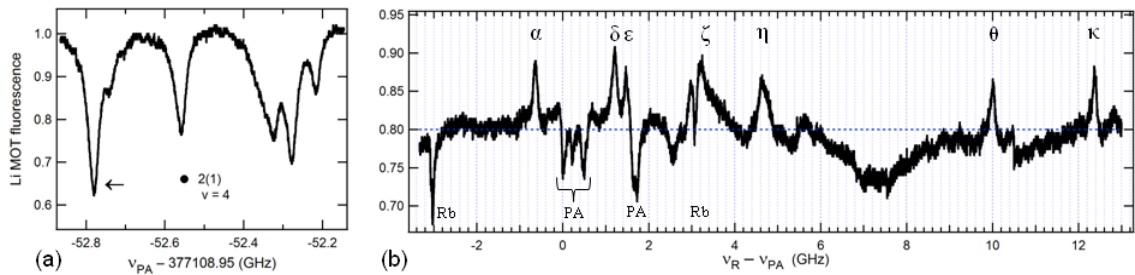


Figure 5.2. (a) 1-photon PA spectrum below the Li ($2s \ ^2S_{1/2}$) + Rb ($5p \ ^2P_{1/2}$) asymptote (this figure is the same as figure 4.2g). The frequency of the ECDL is locked to the PA resonance indicated by the arrow. (b) 2-photon PA spectra when the frequency of the Raman laser is scanned, with the ECDL locked to the PA line indicated by the arrow in (a).

We now discuss preliminary assignments for some of the observed resonances based on comparison with theoretical calculations noting that these assignments may need to be changed in future. In the Raman-type 2-photon PA spectra, only the rotational levels $N'' = 0$ and $N'' = 2$ are visible, where N'' is the nuclear rotational quantum number for the bound ground state molecule. This is because of the selection rule $\Delta N = (N'' - N_{sc}) = 0, \pm 2$ for such 2-photon transitions, where $N_{sc} = 0$ is nuclear rotational quantum number for the scattering state ($N_{sc} = 0$ is justified because only s-wave scattering is possible at the temperature of the MOT¹¹²). Also note that the $X^1\Sigma^+$ and the $a^3\Sigma^+$ potentials have four hyperfine components each. Near the dissociation threshold, these correspond to the Li ($2s, F = 1$) + Rb ($5s, F = 2$), Li ($2s, F = 2$) + Rb ($5s, F = 2$), Li ($2s, F = 1$) + Rb ($5s, F = 3$) and Li ($2s, F = 2$) + Rb ($5s, F = 3$) channels. The differences in the energy of these channels correspond to the atomic hyperfine splitting, as shown in Figure 5.1. In our experiment the free Li and Rb atoms collide mainly along the Li ($2s, F = 2$) + Rb ($5s, F = 2$) channel and let us first assume that the bound $X^1\Sigma^+$ and the $a^3\Sigma^+$ states observed in 2-photon PA also belong to the same hyperfine channel (in a later discussion we relax this assumption). In order to assign the observed spectra, we compare the observed line positions with those calculated using the potential energy curves⁵⁵ for the $X^1\Sigma^+$ and $a^3\Sigma^+$ states. The $X^1\Sigma^+$ state is expected to have 53 vibrational states ($v'' = 0-52$); the binding energies of $X^1\Sigma^+$ ($v'' = 52, N'' = 0$) and $X^1\Sigma^+$ ($v'' = 51, N'' = 0$) levels being 0.42 GHz and 13.93 GHz respectively. The binding energy of the $X^1\Sigma^+$ ($v'' = 51, N'' = 2$) is expected to be 11.56 GHz i.e. the $N'' = 0$ and the $N'' = 2$ levels of the $v'' = 51$ level are expected to be separated by 2.37 GHz. The lines labeled θ and κ are separated by 2.40 GHz and their line positions are also very close to those expected from the

calculation. We thus assign the lines θ and κ to the $X^1\Sigma^+$ ($v'' = 51, N'' = 2$) and $X^1\Sigma^+$ ($v'' = 51, N'' = 0$) levels respectively. The $a^3\Sigma^+$ state is expected to have 15 vibrational states ($v'' = 0-14$); the binding energies of $a^3\Sigma^+$ ($v'' = 14, N'' = 0$) and $a^3\Sigma^+$ ($v'' = 13, N'' = 0$) levels being 3.93 GHz and 33 GHz respectively. The binding energy of the $a^3\Sigma^+$ ($v'' = 14, N'' = 2$) is expected to be 2.35 GHz i.e. the $N'' = 0$ and the $N'' = 2$ levels of the $v'' = 14$ level are expected to be separated by 1.58 GHz. The lines labeled ζ and η are separated by ~ 1.55 GHz (although there is some experimental uncertainty in the measurement of ζ) and their line positions are also close to those expected from the calculation. We thus assign the lines ζ and η to the $a^3\Sigma^+$ ($v'' = 14, N'' = 2$) and $a^3\Sigma^+$ ($v'' = 14, N'' = 0$) levels, respectively.

We repeated the 2-photon PA measurements for different 1-photon PA transitions. This was done because of the following reasons: (i) to verify that the 2-photon resonances, or at least some of them depending on the selection rules and Franck-Condon (FC) overlap (see points *iii* and *iv*), can be reproduced for other 1-photon PA transitions, (ii) to verify that the Raman laser couples the photoassociated level to the ground electronic state and not to a more highly excited electronic state (in case of the latter, the 2-photon resonances would not be observed at the same frequencies on choosing a different PA transition), (iii) there are two electronic ground states, the spin singlet $X^1\Sigma^+$ state and the spin triplet $a^3\Sigma^+$ state, which, in absence of singlet-triplet mixing, can couple only to singlet and triplet PA levels respectively. Thus, in order to observe both the $X^1\Sigma^+$ and the $a^3\Sigma^+$ states, different PA levels need to be chosen (in reality, some singlet-triplet mixing does exist making this selection rule somewhat relaxed), and (iv) different PA levels have outer turning points at different internuclear separations ($\sim 30 -$

45 a_0 for the PA levels considered here) and the FC overlap with the vibrational levels of the ground electronic state will be different for different PA lines. It is expected that more deeply bound PA levels will have better FC overlap with more deeply bound levels of the ground state. This limits the number of ground state levels that can be observed for a particular PA level. The most deeply bound ground state level we observed has a binding energy of 12.4 GHz. Using the theoretically value for the C_6 coefficient for the ground state, we estimate that the outer turning point of this level is $\sim 33 a_0$, consistent with the expectation based on the outer turning point ($\sim 30 a_0$) of the most deeply bound PA level used in the study.

Table 5.1. List of the 2-photon PA resonances observed and the values of $\Delta\nu$. The left most column contains the PA level that was used for the Raman-type 2-photon PA scheme while the observed resonances are in the subsequent columns. The frequencies are in GHz.

PA level	α	β	γ	δ	ε	ζ	η	θ	κ
$2(0^+), v' = 2,$ $\Delta_{PA} = -9.45$	-0.63	-0.31	0.96		1.51	3.1			
$2(1), v' = 3,$ $\Delta_{PA} = -15.93$		-0.31	0.98		1.53	3.1		10.00	
$2(0^+), v' = 3,$ $\Delta_{PA} = -38.08$	-0.59	-0.30	1.01		1.60			10.01	
$2(0^-), v' = 4,$ $\Delta_{PA} = -51.08$		-0.31				3.23		10.04	
$2(1), v' = 4,$ $\Delta_{PA} = -52.81$	-0.64			1.26	1.52	3.2	4.56	10.01	12.40
$2(0^+), v' = 4,$ $\Delta_{PA} = -98.44$		-0.33						10.04	12.44

In table 5.1 we list all the PA levels for which Raman-type 2-photon PA studies were performed along with the corresponding 2-photon resonances observed. We have been conservative in listing only levels which are significantly above the noise due to

background fluctuations and which are easily reproduced in different scans. Also note that the frequency of peak ζ cannot be accurately measured because the shape of the peak is complicated by the presence of the Li loss feature (due to excited Rb atoms) in the same spectral region.

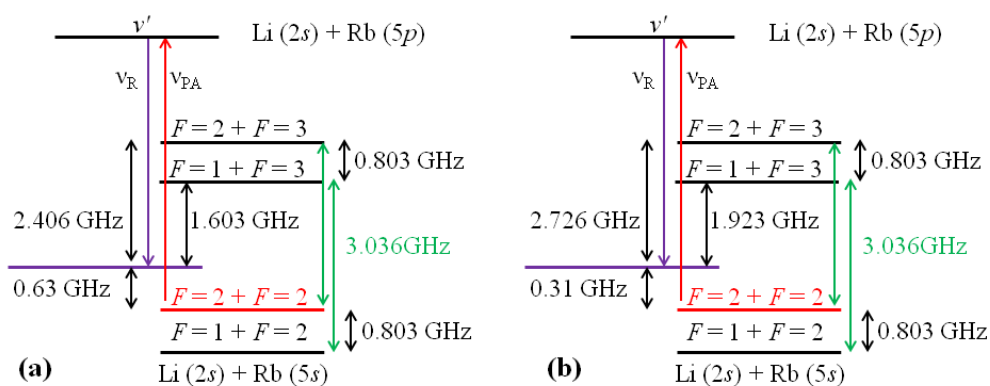


Figure 5.3. Schematic representation of the hyperfine manifolds in the scattering state and in the loosely bound levels of the $X^1\Sigma^+$ and the $a^3\Sigma^+$ states (see text for details).

It is interesting to note that there are two lines, α and β , which are located at negative $\Delta\nu$. These may arise due to bound states in hyperfine manifolds other than the $\text{Li}(2s, F=2) + \text{Rb}(5s, F=2)$ manifold of the $X^1\Sigma^+$ and the $a^3\Sigma^+$ states considered so far. As mentioned before, near the dissociation threshold the hyperfine manifolds are $\text{Li}(2s, F=1) + \text{Rb}(5s, F=2)$, $\text{Li}(2s, F=2) + \text{Rb}(5s, F=2)$, $\text{Li}(2s, F=1) + \text{Rb}(5s, F=3)$ and $\text{Li}(2s, F=2) + \text{Rb}(5s, F=3)$. The PA laser couples the free Li and Rb atoms, colliding mainly along the $\text{Li}(2s, F=2) + \text{Rb}(5s, F=2)$ channel, to one of the hyperfine components of the electronically excited molecular state (for this discussion, it is not necessary to know the assignment for the hyperfine level of electronically excited molecular state). The Raman laser can couple the electronically excited molecular state to

any of the hyperfine components of the $X^1\Sigma^+$ and the $a^3\Sigma^+$ states. For example, the line α at $\Delta\nu = -0.63$ GHz could be a level with binding energy of 1.6 GHz corresponding to the Li ($2s, F = 1$) + Rb ($5s, F = 3$) hyperfine component of the ground state potentials (Figure 5.3a). It could also be a level with binding energy of 2.41 GHz corresponding to a Li ($2s, F = 2$) + Rb ($5s, F = 3$) hyperfine component (Figure 5.3a). Similarly, the line β at $\Delta\nu = -0.31$ GHz could be a level with binding energy of 1.92 GHz or 2.73 GHz corresponding to the Li ($2s, F = 1$) + Rb ($5s, F = 3$) or the Li ($2s, F = 2$) + Rb ($5s, F = 3$) hyperfine components, respectively (Figure 5.3b). The arguments also apply to lines at positive $\Delta\nu$. For example, the line γ at $\Delta\nu = 0.98$ GHz could a level with a binding energy of 0.18 GHz corresponding to the Li ($2s, F = 1$) + Rb ($5s, F = 2$) hyperfine component. The line ε at $\Delta\nu = 1.53$ GHz could a level with a binding energy of 0.73 GHz corresponding to the Li ($2s, F = 1$) + Rb ($5s, F = 2$) hyperfine component. Complete assignments of the lines require considerable theoretical input and, to this end, we are collaborating with Dr. Jesús Pérez-Ríos and Prof. Chris H. Greene.

CHAPTER 6. FUTURE DIRECTIONS

In this chapter, I will first report the production (using PA) and detection (using REMPI) of ultracold LiRb molecules in the electronic ground state. I will then discuss some pathways, different from the ones already discussed in section 4.7, for creating ultracold LiRb molecules in the ground $X^1\Sigma^+$ ($v'' = 0$) state. Finally, I will discuss some proof-of-principle experiments on coherent control that can be performed in the apparatus.

6.1 Production and detection of LiRb molecules in the electronic ground state

The PA experiments described so far have relied on the trap-loss detection scheme. An alternative scheme is to detect the PA resonances by Resonance Enhanced Multi-Photon Ionization (REMPI) of the LiRb molecules formed by PA. All the electronic states observed using trap loss spectroscopy, except the $3(0^+)$ state, have also been detected using REMPI (it is possible that the $3(0^+)$ state could not be detected using REMPI because the LiRb* molecules formed in this state undergo predissociation). LiRb molecules in the electronic ground state (although in high vibrational levels) are produced by PA followed by spontaneous emission. These LiRb molecules are ionized to form LiRb⁺ ions, via a two photon process, with a Nd:YAG-pumped pulsed dye laser (pulse width 10 ns) operating in the 560-585 nm range. The LiRb⁺ ions are extracted using electric field plates and detected using the time of flight (TOF) mass spectrometer (MS) described in chapter 3. Ions of different species (Rb⁺, LiRb⁺, Li⁺ etc.) are differentiated

based on their time of flights T (T is proportional to \sqrt{m} , where m is the mass of the ion). In general, it is difficult to resolve species with similar masses (like Rb^+ and LiRb^+). However, our TOF MS allows us to easily differentiate between Rb^+ and LiRb^+ ions (Figure 6.1) and it is seen that the relation $T_{\text{LiRb}^+}/T_{\text{Rb}^+} = 1.04 = \sqrt{m_{\text{LiRb}^+}/m_{\text{Rb}^+}}$ is also well satisfied. The detection of LiRb^+ ions also confirms that LiRb molecules in the electronic ground state are indeed being created by PA followed by spontaneous emission. More details about REMPI can be found in the theses of Adeel Altaf and John Lorenz.

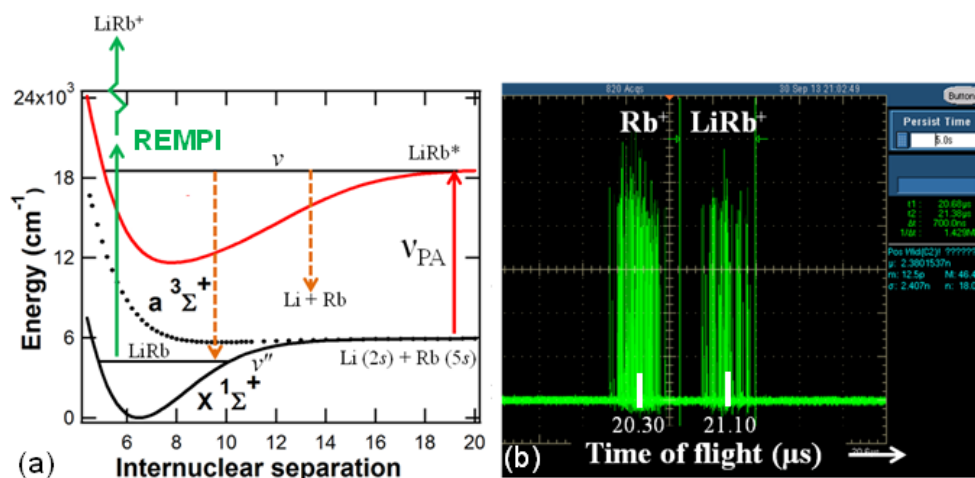


Figure 6.1. (a) The REMPI scheme used to detect ultracold LiRb molecules produced in the electronic ground state. (b) An oscilloscope trace of the TOF spectrum. The spectrum is obtained with ~ 100 individual REMPI pulses. The Rb^+ ions arrive at the detector (MCP) earlier than the LiRb^+ ions. The arrival windows of the Rb^+ and LiRb^+ ions are well separated and hence Rb^+ and LiRb^+ ions can be easily distinguished.

6.2 Alternate schemes for producing ground state LiRb molecules

As discussed in section 4.7, the efficiency with which ground state molecules can be produced depends on the quantity η . Other than the schemes discussed in section 4.7,

there are two additional schemes which may lead to efficient formation of ground state LiRb molecules.

I will first discuss a scheme involving the $v' \sim 15$ levels of the $C^1\Sigma^+$ state which dissociates along the Li ($2p$) + Rb ($5s$) asymptote. From the theoretical potential energy curve⁵⁹, it is estimated that (i) this state has the inner turning point at $\sim 6.5 a_0$ which is approximately equal to the equilibrium inter-nuclear distance $R_{\text{eq}} (= 6.55 a_0)$ of the $X^1\Sigma^+$ ($v'' = 0$) state, and (ii) the energy of the state lies close to the Li ($2s^2S_{1/2}$) + Rb ($5p^2P_{3/2}$) asymptote at 18744.4 cm^{-1} measured from the bottom of the $X^1\Sigma^+$ state (Note that the Li($2s^2S_{1/2}$) + Rb($5p^2P_{1/2}$) asymptote is located at 18506.8 cm^{-1} and that the vibrational index $v' \sim 15$ for the $C^1\Sigma^+$ state is not very accurate because detailed spectroscopic information about $C^1\Sigma^+$ state is not yet available). The photo-association strength to the $C^1\Sigma^+$ ($v' \sim 15$) states is expected to be weak because, being a deeply bound level, the outer turning point is at small inter-nuclear distance ($\sim 10.5 a_0$). However, the situation changes when there is substantial mixing between different electronic states. The $v' \sim 15$ level of the $C^1\Sigma^+$ state lies in a region where there are densely packed rovibrational levels of the $B^1\Pi$ and $b^3\Pi$ states which dissociate along the Li($2^2S_{1/2}$) + Rb($5^2P_{3/2}$) asymptote. These levels of the $B^1\Pi$ and $b^3\Pi$ states have outer turning points at large internuclear separations ($> 30 a_0$) and the PA transitions to these levels are strong. There is a finite probability that a very high vibrational level of the $B^1\Pi$ state lies very close to the $C^1\Sigma^+$ ($v' \sim 15$) level, giving rise to resonant coupling¹¹³ between the two levels. For such resonantly coupled states, the wave function inherits the properties of both the parent states. This hybrid wave function has large amplitude $\sim 6.5 a_0$ inherited from the inner turning point of the $C^1\Sigma^+$ ($v' \sim 15$) level, and also has large amplitude at high inter-

nuclear separation inherited from the $B^1\Pi$ state. PA strength to this resonantly coupled state is enhanced by the large amplitude of the hybrid wave function at large inter-nuclear separation. In absence of spectroscopic studies of the $C^1\Sigma^+$ state, it is difficult to predict whether such resonant coupling exists but if it does, then such states are extremely good states for creating $X^1\Sigma^+$ ($v'' = 0$) state molecules. It is worthwhile to explore PA to such states with a Ti:Sapphire laser with its wavelength tuned close to 780 nm. The $X^1\Sigma^+$ ($v'' = 0$) state molecules, if formed, can be detected using REMPI with a pulsed dye laser tuned around 575 nm (using the $B^1\Pi$ ($v' = 3$) level as the intermediate state).

The second possible scheme is based on photo-association to the $v' = 2$ levels of the $B^1\Pi$ state. Molecules in the $v' = 2$ levels of the $B^1\Pi$ state also decay to the $X^1\Sigma^+$ ($v'' = 0$, $J'' = 0$) state with a very high probability ($\sim 25\%$) as discussed in section 2.5. The PA strength is generally low for such deeply bound levels with outer turning point at a relatively small inter-nuclear separation of $\sim 8.45 a_0$ (obtained from RKR potential). However, in LiCs, which has very similar potential energy curves as LiRb, strong PA lines were seen for such deeply bound levels⁶¹. Although the exact reason for this is unknown, a plausible cause is the increase in the PA efficiency due to wave function mixing between the $X^1\Sigma^+$ and $a^3\Sigma^+$ states near the inner turning point of the $a^3\Sigma^+$ state¹⁰⁵. The presence of such singlet-triplet mixing in case of LiRb is indicated by the LIF lines decaying to the $a^3\Sigma^+$ state from the $B^1\Pi$ ($v' = 20$) level. Whether the singlet-triplet mixing is in the $B^1\Pi$ ($v' = 20$) level or between the $X^1\Sigma^+$ and $a^3\Sigma^+$ states is questionable. The latter seems to be the case because the line positions of the $B^1\Pi$ ($v' = 20$) levels, as measured using FES, did not show signs of any perturbations. For LiRb, the inner turning point of the $a^3\Sigma^+$ state ($\sim 8 a_0$) lines up quite well with the outer turning point of the $B^1\Pi$

($v' = 2$) level $\sim 8.45 a_0$ and a strong PA transition is expected in presence of mixing between the $X^1\Sigma^+$ and $a^3\Sigma^+$ states. It is thus worthwhile to explore PA to the $B^1\Pi$ ($v' = 2$) level with a laser near 864.42(3) nm and detect the $X^1\Sigma^+$ ($v'' = 0$) state molecules using REMPI.

6.3 First set of experiments on coherent control

Although it is most interesting, from a quantum computing point of view discussed in chapter 1, to perform coherent control experiments on the $X^1\Sigma^+$ ($v'' = 0, J'' = 0$) state molecules, it is also worthwhile to demonstrate such schemes with molecules in other levels which are more easily produced. In this section, I will focus mainly on experiments that can be done with the LiRb molecules in the $X^1\Sigma^+$ ($v'' = 51, J'' = 0$) state which has a (experimentally measured) binding energy of ~ 12.4 GHz, a rotational constant $B'' \sim 400$ MHz and is easily produced by spontaneous emission from the PA levels already observed in this thesis. In addition, this state is expected to have a lifetime on the order of ms (based on lifetime of other molecules such as LiCs) which is sufficient for most experiments on coherent control and quantum computing. Being singlet states they are not affected much by stray magnetic fields and suffer much lower decoherence than triplet states.

As a proof of concept of coherent control, rotational superposition between $J'' = 0$ and $J'' = 1$ states of $v'' = 51$ level could be performed in a scheme similar to section 1.3. This is based on the idea of interfering optical transitions in a Raman scheme. The upward leg of the Raman transition (Figure 6.2) is a two-photon transition ($\omega = 192105.2$ GHz, $\lambda = 1560.564$ nm) coupling the $X^1\Sigma^+$ ($v'' = 51, J'' = 0$) state to the $v' = 3, J' = 2$ level

of the 4(1) state (v' measured from dissociation). The downward leg of the Raman transition is a one photon transition ($2\omega - 2B'' = 384209.6$ GHz, $\lambda = 780.284$ nm) which couples the excited $v' = 3, J' = 2$ level of the 4(1) state to the $X^1\Sigma^+$ ($v'' = 51, J'' = 1$). To maintain coherence, the light for the one photon transition ($\lambda = 780.284$ nm) has to be obtained by frequency doubling the $\lambda = 1560.564$ nm light for the two-photon transition, followed by phase modulating it at a frequency $2B''$ ($= 800$ MHz, much lower than 12.94 GHz for $v'' = 0$) using an electro-optic-modulator (EOM). The lower frequency sideband of the frequency doubled light drives the downward leg of the Raman transition (although the carrier frequency is resonant with the $J' = 2 \rightarrow J'' = 0$ transition, this transition is dipole forbidden). This scheme creates a rotational superposition between $J'' = 0$ and $J'' = 1$ states of $v'' = 51$ level.

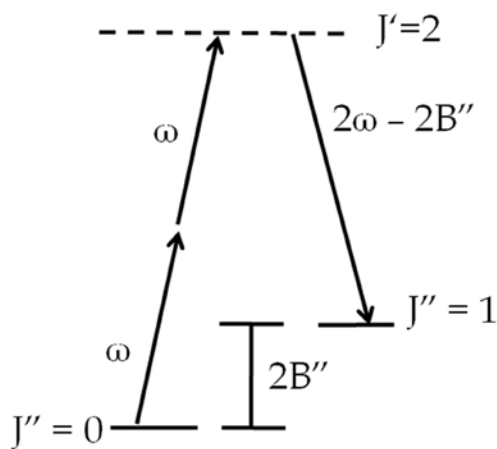


Figure 6.2. Two-color Raman scheme for creating rotational superposition of $J'' = 0$ and $J'' = 1$ levels in the $X^1\Sigma^+$ ($v'' = 51$) state.

The superposition states evolve at a rate of 800 MHz, corresponding to the difference in the energy of the $J'' = 0$ and $J'' = 1$ states of the $v'' = 51$ level. The time period of evolution is 1.25 ns ($1/800$ MHz). This evolution can be detected using multi photon

ionization with a laser pulse whose temporal width is much lower than 1.25 ns. We can use an intense mode locked sub-ps Ti:Sapphire laser for the purpose. There is one such laser in the lab, the repetition rate of the pulses is ~ 80 MHz (~ 12.5 ns) and the duration of each pulse is ~ 0.15 ps, much lower than the evolution period of 1.25 ns. The repetition rate can be tuned by varying the Free Spectral Range (FSR) of the laser cavity and can be adjusted such that consecutive pulses hit the molecules at the same point of their evolution cycle (the arrival time of the pulses can be varied using an adjustable optical delay line in the path of the mode locked laser pulse). For example, if the FSR is tuned to 80.00 MHz (= 12.50 ns) then two consecutive pulses will hit the molecules exactly at the same point of their evolution after $12.50 \text{ ns} / 1.25 \text{ ns} = 10$ evolutions. The Li^+ and Rb^+ ions created by the pulsed laser can be detected using the MCP + phosphor screen detector assembly already installed in the apparatus to image such ions. The technique is similar to a velocity map imaging detector. Li^+ and Rb^+ ions will form rings of different diameters on the phosphor screen and any asymmetry in the images will be a signature of rotational superposition states. We also note that all the lasers and optical components required for the experiment are available in our laboratory.

LIST OF REFERENCES

LIST OF REFERENCES

1. Wineland, D. J., Drullinger, R. E. & Walls, F. L. Radiation-Pressure Cooling of Bound Resonant Absorbers. *Phys. Rev. Lett.* **40**, 1639–1642 (1978).
2. Krens, R. V. Cold controlled chemistry. *Phys. Chem. Chem. Phys.* **10**, 4079–4092 (2008).
3. Krens, R. V., Stwalley, W. C. & Friedrich, B. *COLD MOLECULES: Theory, Experiment, Applications*. (CRC Press, Taylor & Francis Group, 2009).
4. Carr, L. D., DeMille, D., Krens, R. V & Ye, J. Cold and ultracold molecules: science, technology and applications. *New J. Phys.* **11**, 055049 (2009).
5. Sandars, P. G. H. Measurability of the Proton Electric Dipole Moment. *Phys. Rev. Lett.* **19**, 1396 (1967).
6. Hudson, E. R., Lewandowski, H. J., Sawyer, B. C. & Ye, J. Cold Molecule Spectroscopy for Constraining the Evolution of the Fine Structure Constant. *Phys. Rev. Lett.* **96**, 143004 (2006).
7. Kozlov, M. G. & Labzowsky, L. N. Parity violation effects in diatomics. *J. Phys. B At. Mol. Opt. Phys.* **28**, 1933–1961 (1995).
8. Ni, K.-K. *et al.* A high phase-space-density gas of polar molecules. *Science* **322**, 231–235 (2008).
9. Ni, K.-K. *et al.* Dipolar collisions of polar molecules in the quantum regime. *Nature* **464**, 1324–1328 (2010).
10. Ospelkaus, S. *et al.* Quantum-State Controlled Chemical Reactions of Ultracold Potassium-Rubidium Molecules. *Science* **327**, 853–857 (2010).
11. De Miranda, M. H. G. *et al.* Controlling the quantum stereodynamics of ultracold bimolecular reactions. *Nature Phys.* **7**, 502–507 (2011).
12. Büchler, H. P., Micheli, A. & Zoller, P. Three-body interactions with cold polar molecules. *Nature Phys.* **3**, 726–731 (2007).

13. Baranov, M. A., Dalmonte, M., Pupillo, G. & Zoller, P. Condensed matter theory of dipolar quantum gases. *Chem. Rev.* **112**, 5012–5061 (2012).
14. DeMille, D. Quantum Computation with Trapped Polar Molecules. *Phys. Rev. Lett.* **88**, 067901 (2002).
15. Yelin, S., Kirby, K. & Côté, R. Schemes for robust quantum computation with polar molecules. *Phys. Rev. A* **74**, 050301 (2006).
16. Shapiro, M. & Brumer, P. W. *Principles of the quantum control of molecular processes*. (Wiley-Interscience, 2003).
17. Vrakking, M. J. J. & Stolte, S. Coherent control of molecular orientation. *Chem. Phys. Lett.* **271**, 209–215 (1997).
18. Chen, C., Yin, Y. & Elliott, D. Interference between optical transitions. *Phys. Rev. Lett.* **64**, 507–510 (1990).
19. Yin, Y., Chen, C. & Elliott, D. S. Asymmetric photoelectron angular distributions from interfering photoionization processes. *Phys. Rev. Lett.* **69**, 2353–2356 (1992).
20. Yin, Y.-Y., Elliott, D. S., Shehadeh, R. & Grant, E. R. Two-pathway coherent control of photoelectron angular distributions in molecular NO. *Chem. Phys. Lett.* **241**, 591–596 (1995).
21. Metcalf, H. J. & Straten, P. van der. *Laser cooling and trapping*. (Springer, 2001).
22. Herzberg, G. *Molecular Spectra and Molecular Structure I: Spectra of Diatomic Molecules*. (D. Van Nostrand Company, Inc., 1961).
23. Rosa, M. D. Laser-cooling molecules: Concept , candidates, and supporting hyperfine-resolved measurements of rotational lines in the A-X(0,0) band of CaH. *Eur. Phys. J. D* **31**, 395–402 (2004).
24. Shuman, E. S., Barry, J. F., Glenn, D. R. & DeMille, D. Radiative Force from Optical Cycling on a Diatomic Molecule. *Phys. Rev. Lett.* **103**, 223001 (2009).
25. Shuman, E. S., Barry, J. F. & DeMille, D. Laser cooling of a diatomic molecule. *Nature* **467**, 820–823 (2010).
26. Weinstein, J. D., DeCarvalho, R., Guillet, T., Friedrich, B. & Doyle, J. M. Magnetic trapping of calcium monohydride molecules at millikelvin temperatures. *Nature* **395**, 148–150 (1998).

27. Bethlem, H., Berden, G. & Meijer, G. Decelerating Neutral Dipolar Molecules. *Phys. Rev. Lett.* **83**, 1558–1561 (1999).
28. Elioff, M. S., Valentini, J. J. & Chandler, D. W. Subkelvin cooling NO molecules via “billiard-like” collisions with argon. *Science* **302**, 1940–1943 (2003).
29. Rangwala, S., Junglen, T., Rieger, T., Pinkse, P. & Rempe, G. Continuous source of translationally cold dipolar molecules. *Phys. Rev. A* **67**, 043406 (2003).
30. Rieger, T., Junglen, T., Rangwala, S., Pinkse, P. & Rempe, G. Continuous Loading of an Electrostatic Trap for Polar Molecules. *Phys. Rev. Lett.* **95**, 173002 (2005).
31. Fulton, R., Bishop, A. I., Shneider, M. N. & Barker, P. F. Controlling the motion of cold molecules with deep periodic optical potentials. *Nature Phys.* **2**, 465–468 (2006).
32. Narevicius, E. *et al.* Stopping Supersonic Beams with a Series of Pulsed Electromagnetic Coils: An Atomic Coilgun. *Phys. Rev. Lett.* **100**, 093003 (2008).
33. Narevicius, E. & Raizen, M. G. Toward Cold Chemistry with Magnetically Decelerated Supersonic Beams. *Chem. Rev.* **112**, 4879–4889 (2012).
34. Van Buuren, L. *et al.* Electrostatic Extraction of Cold Molecules from a Cryogenic Reservoir. *Phys. Rev. Lett.* **102**, 033001 (2009).
35. Stuhl, B. K. *et al.* Evaporative cooling of the dipolar hydroxyl radical. *Nature* **492**, 396–400 (2012).
36. Domokos, P. & Ritsch, H. Collective Cooling and Self-Organization of Atoms in a Cavity. *Phys. Rev. Lett.* **89**, 253003 (2002).
37. Morigi, G., Pinkse, P., Kowalewski, M. & de Vivie-Riedle, R. Cavity Cooling of Internal Molecular Motion. *Phys. Rev. Lett.* **99**, 073001 (2007).
38. Lev, B. *et al.* Prospects for the cavity-assisted laser cooling of molecules. *Phys. Rev. A* **77**, 023402 (2008).
39. Stuhl, B. K., Sawyer, B. C., Wang, D. & Ye, J. Magneto-optical Trap for Polar Molecules. *Phys. Rev. Lett.* **101**, 243002 (2008).
40. Van Veldhoven, J., Bethlem, H. & Meijer, G. ac Electric Trap for Ground-State Molecules. *Phys. Rev. Lett.* **94**, 083001 (2005).
41. Sawyer, B. *et al.* Magneto-electrostatic Trapping of Ground State OH Molecules. *Phys. Rev. Lett.* **98**, 253002 (2007).

42. Thorsheim, H. R., Weiner, J. & Julienne, P. S. Laser-Induced Photoassociation of Ultracold Sodium Atoms. *Phys. Rev. Lett.* **58**, 2420–2423 (1987).
43. Jones, K., Tiesinga, E., Lett, P. D. & Julienne, P. S. Ultracold photoassociation spectroscopy: Long-range molecules and atomic scattering. *Rev. Mod. Phys.* **78**, 483–535 (2006).
44. Ulmanis, J., Deiglmayr, J., Repp, M., Wester, R. & Weidemüller, M. Ultracold Molecules Formed by Photoassociation: Heteronuclear Dimers, Inelastic Collisions, and Interactions with Ultrashort Laser Pulses. *Chem. Rev.* **112**, 4890–4927 (2012).
45. Aymar, M. & Dulieu, O. Calculation of accurate permanent dipole moments of the lowest $1,3\Sigma^+$ states of heteronuclear alkali dimers using extended basis sets. *J. Chem. Phys.* **122**, 204302 (2005).
46. Żuchowski, P. S. & Hutson, J. M. Reactions of ultracold alkali-metal dimers. *Phys. Rev. A* **81**, 060703 (2010).
47. Chotia, A. *et al.* Long-Lived Dipolar Molecules and Feshbach Molecules in a 3D Optical Lattice. *Phys. Rev. Lett.* **108**, 080405 (2012).
48. Mermin, N. D. *Quantum Computer Science: An Introduction*. (Cambridge University Press, 2007).
49. Nielsen, M. A. & Chuang, I. L. *Quantum Computation and Quantum Information*. (Cambridge University Press, 2004).
50. Bellac, M. Le. *A Short Introduction to Quantum Information and Quantum Computation*. (Cambridge University Press, 2006).
51. Deh, B., Marzok, C., Zimmermann, C. & Courteille, P. Feshbach resonances in mixtures of ultracold ${}^6\text{Li}$ and ${}^{87}\text{Rb}$ gases. *Phys. Rev. A* **77**, 010701 (2008).
52. Li, Z., Singh, S., Tscherbil, T. & Madison, K. Feshbach resonances in ultracold ${}^{85}\text{Rb}$ - ${}^{87}\text{Rb}$ and ${}^6\text{Li}$ - ${}^{87}\text{Rb}$ mixtures. *Phys. Rev. A* **78**, 022710 (2008).
53. Marzok, C. *et al.* Feshbach resonances in an ultracold ${}^7\text{Li}$ and ${}^{87}\text{Rb}$ mixture. *Phys. Rev. A* **79**, 012717 (2009).
54. Deh, B. *et al.* Giant Feshbach resonances in ${}^6\text{Li}$ - ${}^{85}\text{Rb}$ mixtures. *Phys. Rev. A* **82**, 020701 (2010).

55. Ivanova, M., Stein, A., Pashov, A., Knöckel, H. & Tiemann, E. The X $^1\Sigma^+$ state of LiRb studied by Fourier-transform spectroscopy. *J. Chem. Phys.* **134**, 024321 (2011).
56. Ivanova, M., Stein, A., Pashov, A., Knöckel, H. & Tiemann, E. The B $^1\Pi$ and D $^1\Pi$ states of LiRb. *J. Chem. Phys.* **138**, 094315 (2013).
57. Dutta, S., Altaf, A., Elliott, D. S. & Chen, Y. P. Laser spectroscopy of the X $^1\Sigma^+$ and B $^1\Pi$ states of the LiRb molecule. *Chem. Phys. Lett.* **511**, 7–11 (2011).
58. Igel-Mann, G., Wedig, U., Fuentealba, P. & Stoll, H. Ground-state properties of alkali dimers XY (X, Y=Li to Cs). *J. Chem. Phys.* **84**, 5007–5012 (1986).
59. Korek, M. *et al.* Theoretical study of the electronic structure of the LiRb and NaRb molecules. *Chem. Phys.* **256**, 1–6 (2000).
60. Korek, M., Younes, G. & AL-Shawa, S. Theoretical calculation of the electronic structure of the molecule LiRb including the spin–orbit interaction. *J. Mol. Struct. THEOCHEM* **899**, 25–31 (2009).
61. Deiglmayr, J. *et al.* Formation of Ultracold Polar Molecules in the Rovibrational Ground State. *Phys. Rev. Lett.* **101**, 133004 (2008).
62. Deiglmayr, J. Structure, formation, and interactions of ultracold polar molecules. Doctoral thesis, Albert-Ludwig University of Freiburg (2009). Available at: http://www.freidok.uni-freiburg.de/volltexte/7169/pdf/Dissertation_JohannesDeiglmayr_FreiDok.pdf
63. Bednarska, V., Jackowska, I., Jastrzebski, W. & Kowalczyk, P. A three-section heat-pipe oven for heteronuclear alkali molecules. *Meas. Sci. Technol.* **7**, 1291–1293 (1996).
64. Brown, J. M. *et al.* The Labeling of Parity Doublet Levels in Linear Molecules. *J. Mol. Spectrosc.* **55**, 500–503 (1975).
65. Bednarska, V., Ekers, A., Kowalczyk, P. & Jastrzębski, W. Doppler-free spectroscopy of KLi. *J. Chem. Phys.* **106**, 6332–6337 (1997).
66. Pellegrini, P., Gacesa, M. & Côté, R. Giant Formation Rates of Ultracold Molecules via Feshbach-Optimized Photoassociation. *Phys. Rev. Lett.* **101**, 053201 (2008).
67. Kuznetsova, E., Gacesa, M., Pellegrini, P., Yelin, S. F. & Côté, R. Efficient formation of ground-state ultracold molecules via STIRAP from the continuum at a Feshbach resonance. *New J. Phys.* **11**, 055028 (2009).

68. Li, X., Menzel-Jones, C. & Shapiro, M. Spectroscopic Phase and the Extraction of Excited-State Potentials from Fluorescence Data. *J. Phys. Chem. Lett.* **1**, 3172–3176 (2010).
69. Li, X., Menzel-Jones, C., Avisar, D. & Shapiro, M. Solving the spectroscopic phase: imaging excited wave packets and extracting excited state potentials from fluorescence data. *Phys. Chem. Chem. Phys.* **12**, 15760–15765 (2010).
70. Dutta, S., Altaf, A., Lorenz, J., Elliott, D. S. & Chen, Y. P. Interspecies collision-induced losses in a dual species ^7Li - ^{85}Rb magneto-optical trap. Manuscript submitted (2013). Preprint available at: <http://arxiv.org/abs/1306.5196>
71. Dutta, S., Elliott, D. S. & Chen, Y. P. Mode-hop-free tuning over 135 GHz of external cavity diode lasers without antireflection coating. *Appl. Phys. B* **106**, 629–633 (2012).
72. Serwane, F. The setup of a Magneto Optical Trap for the preparation of a mesoscopic degenerate Fermi gas. Diploma thesis, University of Heidelberg (2007). Available at: <http://www.lithium6.de/files/diplomarbeit-friedhelm.pdf>
73. Wang, D. *et al.* The photoassociative spectroscopy, photoassociative molecule formation, and trapping of ultracold ^{39}K - ^{85}Rb . *Eur. Phys. J. D* **31**, 165–177 (2004).
74. Wiley, W. C. & McLaren, I. H. Time-of-Flight Mass Spectrometer with Improved Resolution. *Rev. Sci. Instrum.* **26**, 1150–1157 (1955).
75. Kraft, S. D. *et al.* A high-resolution time-of-flight mass spectrometer for the detection of ultracold molecules. *Appl. Phys. B* **89**, 453–457 (2007).
76. Eppink, A. T. J. B. & Parker, D. H. Velocity map imaging of ions and electrons using electrostatic lenses: Application in photoelectron and photofragment ion imaging of molecular oxygen. *Rev. Sci. Instrum.* **68**, 3477–3484 (1997).
77. Gensemer, S., Sanchez-Villicana, V., Tan, K., Grove, T. & Gould, P. Trap-loss collisions of ^{85}Rb and ^{87}Rb : Dependence on trap parameters. *Phys. Rev. A* **56**, 4055–4063 (1997).
78. Smith, D. A. Single-Impulse Magnetic Focusing of Launched Cold Atoms. Doctoral thesis, Durham University (2005). Available at: http://etheses.dur.ac.uk/2756/1/2756_833.pdf?UkUDh:CyT
79. Mancini, M. W., Caires, A. R. L., Telles, G. D., Bagnato, V. S. & Marcassa, L. G. Trap loss rate for heteronuclear cold collisions in two species magneto-optical trap. *Eur. Phys. J. D* **30**, 105–116 (2004).

80. Townsend, C. G. *et al.* Phase-space density in the magneto-optical trap. *Phys. Rev. A* **52**, 1423–1440 (1995).
81. Walker, T., Sesko, D. & Wieman, C. Collective Behavior of Optically Trapped Neutral Atoms. *Phys. Rev. Lett.* **64**, 408–412 (1990).
82. Weiner, J. & Julienne, P. S. Experiments and theory in cold and ultracold collisions. *Rev. Mod. Phys.* **71**, 1–85 (1999).
83. Schlöder, U., Engler, H., Schunemann, U., Grimm, R. & Weidemüller, M. Cold inelastic collisions between lithium and cesium in a two-species magneto-optical trap. *Eur. Phys. J. D* **7**, 331–340 (1999).
84. Ritchie, N. M., Abraham, E. R. I. & Hulet, R. G. Trap Loss Collisions of ^7Li : The Role of Trap Depth. *Laser Phys.* **4**, 1066–1075 (1994).
85. Ritchie, N. W. M. *et al.* Trap-loss collisions of ultracold lithium atoms. *Phys. Rev. A* **51**, 890–893 (1995).
86. Schunemann, U., Engler, H., Zielonkowski, M., Weidemüller, M. & Grimm, R. Magneto-optic trapping of lithium using semiconductor lasers. *Opt. Comm.* **158**, 263–272 (1998).
87. Haw, M. *et al.* Magneto-optical trap loading rate dependence on trap depth and vapor density. *J. Opt. Soc. Am. B* **29**, 475–483 (2012).
88. Movre, M. & Beuc, R. van der Waals interaction in excited alkali-metal dimers. *Phys. Rev. A* **31**, 2957–2967 (1985).
89. Bussery, B., Achkar, Y. & Aubert-Frécon, M. Long-range molecular states dissociating to the three or four lowest asymptotes for the ten heteronuclear diatomic alkali molecules. *Chem. Phys.* **116**, 319–338 (1987).
90. Marinescu, M. & Sadeghpour, H. Long-range potentials for two-species alkali-metal atoms. *Phys. Rev. A* **59**, 390–404 (1999).
91. Wallace, C. D. *et al.* Measurements of temperature and spring constant in a magneto-optical trap. *J. Opt. Soc. Am. B* **11**, 703–711 (1994).
92. Ladouceur, K. *et al.* Compact laser cooling apparatus for simultaneous cooling of lithium and rubidium. *J. Opt. Soc. Am. B* **26**, 210–217 (2009).
93. Ketterle, W., Davis, K. B., Joffe, M. A., Martin, A. & Pritchard, D. E. High Densities of Cold Atoms in a Dark Spontaneous-Force Optical Trap. *Phys. Rev. Lett.* **70**, 2253–2256 (1993).

94. Townsend, C. G. *et al.* High-density trapping of cesium atoms in a dark magneto-optical trap. *Phys. Rev. A* **53**, 1702–1714 (1996).
95. Stwalley, W. C., Bellos, M., Carollo, R., Banerjee, J. & Bermudez, M. Shortcuts for understanding rovibronic spectroscopy of ultracold alkali metal diatomic molecules. *Mol. Phys.* **110**, 1739–1755 (2012).
96. Ridinger, a. *et al.* Photoassociative creation of ultracold heteronuclear ${}^6\text{Li}{}^{40}\text{K}^*$ molecules. *EPL (Europhysics Lett.)* **96**, 33001 (2011).
97. Ridinger, A. Towards quantum degenerate Fermi mixtures: Photoassociation of weakly bound ${}^6\text{Li}{}^{40}\text{K}$ molecules. Doctoral thesis, University of Paris (2011). Available at: http://tel.archives-ouvertes.fr/docs/00/61/32/11/PDF/Thesis_Armin_RIDINGER.pdf
98. LeRoy, R. J. & Bernstein, R. B. Dissociation Energy and Long-Range Potential of Diatomic Molecules from Vibrational Spacings of Higher Levels. *J. Chem. Phys.* **52**, 3869–3879 (1970).
99. Grochola, a *et al.* Photoassociation spectroscopy of the B ${}^1\Pi$ state of LiCs. *J. Chem. Phys.* **131**, 054304 (2009).
100. Wang, H. & Stwalley, W. C. Ultracold photoassociative spectroscopy of heteronuclear alkali-metal diatomic molecules. *J. Chem. Phys.* **108**, 5767–5771 (1998).
101. Azizi, S., Aymar, M. & Dulieu, O. Prospects for the formation of ultracold ground state polar molecules from mixed alkali atom pairs. *Eur. Phys. J. D* **31**, 195–203 (2004).
102. Schlöder, U., Silber, C., Deuschle, T. & Zimmermann, C. Saturation in heteronuclear photoassociation of ${}^6\text{Li}{}^7\text{Li}$. *Phys. Rev. A* **66**, 061403 (2002).
103. Bohn, J. & Julienne, P. Semianalytic theory of laser-assisted resonant cold collisions. *Phys. Rev. A* **60**, 414–425 (1999).
104. Pellegrini, P. & Côté, R. Probing the unitarity limit at low laser intensities. *New J. Phys.* **11**, 055047 (2009).
105. Deiglmayr, J. *et al.* Influence of a Feshbach resonance on the photoassociation of LiCs. *New J. Phys.* **11**, 055034 (2009).
106. Haimberger, C., Kleinert, J., Dulieu, O. & Bigelow, N. P. Processes in the formation of ultracold NaCs. *J. Phys. B At. Mol. Opt. Phys.* **39**, S957–S963 (2006).

107. Kerman, A., Sage, J., Sainis, S., Bergeman, T. & DeMille, D. Production of Ultracold, Polar RbCs* Molecules via Photoassociation. *Phys. Rev. Lett.* **92**, 033004 (2004).
108. Aikawa, K. *et al.* Coherent Transfer of Photoassociated Molecules into the Rovibrational Ground State. *Phys. Rev. Lett.* **105**, 203001 (2010).
109. Aikawa, K. All-optical selective formation of ultracold molecules in the rovibrational ground state. Doctoral thesis, University of Tokto (2011). At: http://ultracold.t.u-tokyo.ac.jp/inouyeLAB/publications/2011_Aikawa_PhD.pdf
110. Abraham, E. R. I., McAlexander, W. I., Sackett, C. A. & Hulet, R. G. Spectroscopic Determination of the s -Wave Scattering Length of Lithium. *Phys. Rev. Lett.* **74**, 1315–1318 (1995).
111. Schlöder, U., Deuschle, T., Silber, C. & Zimmermann, C. Autler-Townes splitting in two-color photoassociation of ^6Li . *Phys. Rev. A* **68**, 051403 (2003).
112. Dutta, S., Lorenz, J., Altaf, A., Elliott, D. S. & Chen, Y. P. Photoassociation of ultracold LiRb* molecules : observation of high efficiency and unitarity-limited rate saturation. Manuscript submitted (2013).
113. Stwalley, W. C. *et al.* Resonant coupling in the heteronuclear alkali dimers for direct photoassociative formation of X(0,0) ultracold molecules. *J. Phys. Chem. A* **114**, 81–86 (2010).

APPENDICES

Appendix A List of observed transitions using FES

The material in this appendix is published as the supplementary information of *Chem. Phys. Lett.* 511, 7–11 (2011).

In Figure A.1, the transition frequencies of all Q branch transitions in ${}^7\text{Li}{}^{85}\text{Rb}$ observed in this study is plotted against $J(J+1)$. All the transitions in ${}^7\text{Li}{}^{85}\text{Rb}$ observed using Fluorescence Emission Spectroscopy (FES) is listed in Table A.1.

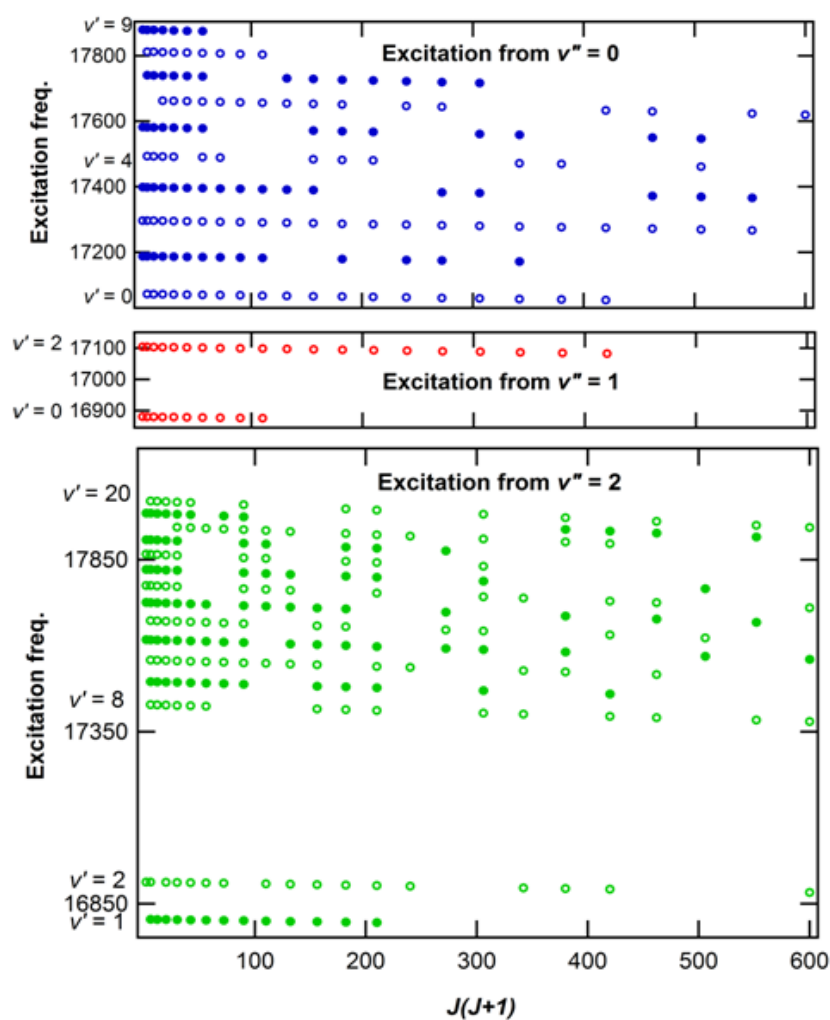


Figure A.1. The transition frequencies of all Q branch transitions observed in this study plotted against $J(J+1)$. For clarity, even and odd v' levels are denoted by open circles (\circ) and filled circles (\bullet) respectively.

Table A.1. All the transitions in ${}^7\text{Li}^{85}\text{Rb}$ observed using Fluorescence Emission Spectroscopy (FES). The average accuracy of the line positions is 0.02 cm^{-1} . ν'' and ν' are the vibrational quantum numbers of the $X\ ^1\Sigma^+$ and $B\ ^1\Pi$ states respectively. J'' and J' are the rotational quantum numbers of the $X\ ^1\Sigma^+$ and $B\ ^1\Pi$ states respectively.

#	ν''	J''	ν'	J'	Frequency (cm^{-1})	#	ν''	J''	ν'	J'	Frequency (cm^{-1})
1	0	2	0	2	17072.63	350	2	14	18	14	17922.70
2	0	3	0	3	17072.36	351	2	15	18	15	17919.02
3	0	4	0	4	17072.01	352	2	17	18	17	17910.90
4	0	5	0	5	17071.58	353	2	19	18	19	17901.80
5	0	6	0	6	17071.05	354	2	20	18	20	17896.86
6	0	7	0	7	17070.41	355	2	1	19	1	17985.92
7	0	8	0	8	17069.71	356	2	2	19	2	17985.40
8	0	9	0	9	17068.90	357	2	3	19	3	17984.65
9	0	10	0	10	17067.99	358	2	4	19	4	17983.64
10	0	11	0	11	17067.03	359	2	5	19	5	17982.41
11	0	12	0	12	17065.98	360	2	6	19	6	17980.89
12	0	13	0	13	17064.82	361	2	8	19	8	17977.10
13	0	14	0	14	17063.57	362	2	9	19	9	17974.83
14	0	15	0	15	17062.23	363	2	19	19	19	17938.22
15	0	16	0	16	17060.81	364	2	20	19	20	17933.16
16	0	17	0	17	17059.29	365	2	21	19	21	17927.73
17	0	18	0	18	17057.69	366	2	23	19	23	17916.39
18	0	19	0	19	17056.00	367	2	25	19	25	17903.92
19	0	20	0	20	17054.17	368	2	27	19	27	17890.43
20	0	1	1	1	17188.24	369	2	28	19	28	17883.27
21	0	2	1	2	17188.07	370	2	2	20	2	18021.08
22	0	3	1	3	17187.77	371	2	3	20	3	18020.30
23	0	4	1	4	17187.39	372	2	4	20	4	18019.26
24	0	5	1	5	17186.89	373	2	5	20	5	18017.96
25	0	6	1	6	17186.29	374	2	6	20	6	18016.42
26	0	7	1	7	17185.62	375	2	9	20	9	18010.21
27	0	8	1	8	17184.85	376	2	13	20	13	17998.30
28	0	9	1	9	17183.96	377	2	14	20	14	17994.67
29	0	10	1	10	17182.99	378	2	17	20	17	17982.22
30	0	13	1	13	17179.47	379	2	19	20	19	17972.58
31	0	15	1	15	17176.64	380	2	21	20	21	17961.90
32	0	16	1	16	17175.08	381	2	23	20	23	17950.16
33	0	18	1	18	17171.66	382	2	24	20	24	17943.91
34	0	1	2	1	17296.88	383	0	3	0	4	17073.73
35	0	2	2	2	17296.67	384	0	4	0	5	17073.73
36	0	3	2	3	17296.37	385	0	5	0	6	17073.62

37	0	4	2	4	17295.92		386	0	6	0	7	17073.41
38	0	5	2	5	17295.38		387	0	7	0	8	17073.15
39	0	6	2	6	17294.76		388	0	8	0	9	17072.80
40	0	7	2	7	17294.01		389	0	9	0	10	17072.36
41	0	8	2	8	17293.14		390	0	10	0	11	17071.78
42	0	9	2	9	17292.18		391	0	11	0	12	17071.14
43	0	10	2	10	17291.14		392	0	12	0	13	17070.41
44	0	11	2	11	17289.96		393	0	13	0	14	17069.59
45	0	12	2	12	17288.69		394	0	14	0	15	17068.66
46	0	13	2	13	17287.28		395	0	15	0	16	17067.67
47	0	14	2	14	17285.79		396	0	16	0	17	17066.59
48	0	15	2	15	17284.19		397	0	17	0	18	17065.40
49	0	16	2	16	17282.47		398	0	18	0	19	17064.12
50	0	17	2	17	17280.65		399	0	19	0	20	17062.78
51	0	18	2	18	17278.71		400	0	20	0	21	17061.32
52	0	19	2	19	17276.68		401	0	21	0	22	17059.78
53	0	20	2	20	17274.53		402	0	22	0	23	17058.15
54	0	21	2	21	17272.26		403	0	23	0	24	17056.41
55	0	22	2	22	17269.90		404	0	24	0	25	17054.57
56	0	23	2	23	17267.40		405	0	25	0	26	17052.65
57	0	1	3	1	17398.66		406	0	5	0	4	17069.86
58	0	2	3	2	17398.45		407	0	6	0	5	17068.98
59	0	3	3	3	17398.08		408	0	7	0	6	17068.02
60	0	4	3	4	17397.63		409	0	8	0	7	17066.96
61	0	5	3	5	17397.05		410	0	9	0	8	17065.81
62	0	6	3	6	17396.36		411	0	10	0	9	17064.58
63	0	7	3	7	17395.54		412	0	11	0	10	17063.27
64	0	8	3	8	17394.60		413	0	12	0	11	17061.85
65	0	9	3	9	17393.54		414	0	13	0	12	17060.36
66	0	10	3	10	17392.39		415	0	14	0	13	17058.76
67	0	11	3	11	17391.09		416	0	15	0	14	17057.10
68	0	12	3	12	17389.67		417	0	16	0	15	17055.33
69	0	16	3	16	17382.90		418	0	17	0	16	17053.47
70	0	17	3	17	17380.91		419	0	18	0	17	17051.55
71	0	21	3	21	17371.73		420	0	19	0	18	17049.48
72	0	22	3	22	17369.13		421	0	23	0	22	17040.45
73	0	23	3	23	17366.42		422	0	27	0	26	17029.94
74	0	2	4	2	17493.37		423	1	5	0	6	16880.69
75	0	3	4	3	17492.98		424	1	6	0	7	16880.53
76	0	4	4	4	17492.49		425	1	7	0	8	16880.26
77	0	5	4	5	17491.83		426	1	8	0	9	16879.92
78	0	7	4	7	17490.19		427	1	9	0	10	16879.49
79	0	8	4	8	17489.15		428	1	10	0	11	16878.98
80	0	12	4	12	17483.83		429	1	11	0	12	16878.36

81	0	13	4	13	17482.18	430	1	12	0	13	16877.68
82	0	14	4	14	17480.38	431	1	14	0	15	16876.04
83	0	18	4	18	17471.95	432	1	15	0	16	16875.07
84	0	19	4	19	17469.54	433	1	16	0	17	16874.02
85	0	22	4	22	17461.42	434	1	17	0	18	16872.88
86	0	1	5	1	17581.99	435	1	7	0	6	16875.13
87	0	2	5	2	17581.71	436	1	8	0	7	16874.11
88	0	3	5	3	17581.31	437	1	9	0	8	16872.97
89	0	4	5	4	17580.75	438	1	10	0	9	16871.80
90	0	5	5	5	17580.07	439	1	11	0	10	16870.49
91	0	6	5	6	17579.23	440	1	12	0	11	16869.12
92	0	7	5	7	17578.28	441	1	13	0	12	16867.66
93	0	12	5	12	17571.39	442	1	16	0	15	16862.77
94	0	13	5	13	17569.60	443	1	17	0	16	16860.96
95	0	14	5	14	17567.67	444	1	18	0	17	16859.06
96	0	17	5	17	17561.02	445	1	19	0	18	16857.10
97	0	18	5	18	17558.52	446	2	13	0	14	16686.44
98	0	21	5	21	17550.17	447	2	14	0	15	16685.63
99	0	22	5	22	17547.12	448	2	15	0	16	16684.71
100	0	4	6	4	17662.91	449	2	16	0	17	16683.71
101	0	5	6	5	17662.20	450	2	17	0	18	16682.63
102	0	6	6	6	17661.29	451	2	18	0	19	16681.46
103	0	7	6	7	17660.26	452	2	19	0	20	16680.21
104	0	8	6	8	17659.08	453	2	20	0	21	16678.90
105	0	9	6	9	17657.74	454	2	21	0	22	16677.48
106	0	10	6	10	17656.24	455	2	22	0	23	16675.98
107	0	11	6	11	17654.62	456	2	23	0	24	16674.39
108	0	12	6	12	17652.84	457	2	24	0	25	16672.70
109	0	13	6	13	17650.91	458	2	7	0	6	16684.49
110	0	15	6	15	17646.61	459	2	8	0	7	16683.49
111	0	16	6	16	17644.22	460	2	9	0	8	16682.38
112	0	20	6	20	17633.14	461	2	10	0	9	16681.21
113	0	21	6	21	17629.97	462	2	11	0	10	16679.96
114	0	23	6	23	17623.23	463	2	12	0	11	16678.65
115	0	24	6	24	17619.59	464	2	13	0	12	16677.23
116	0	2	7	2	17740.59	465	2	14	0	13	16675.70
117	0	3	7	3	17740.12	466	2	15	0	14	16674.14
118	0	4	7	4	17739.49	467	2	16	0	15	16672.45
119	0	5	7	5	17738.71	468	0	7	1	8	17189.13
120	0	6	7	6	17737.76	469	0	8	1	9	17188.57
121	0	7	7	7	17736.63	470	0	9	1	10	17187.92
122	0	11	7	11	17730.62	471	0	10	1	11	17187.21
123	0	12	7	12	17728.71	472	0	11	1	12	17186.41
124	0	13	7	13	17726.63	473	0	12	1	13	17185.56

125	0	14	7	14	17724.40	474	0	13	1	14	17184.61
126	0	15	7	15	17722.01	475	0	14	1	15	17183.52
127	0	16	7	16	17719.44	476	0	15	1	16	17182.37
128	0	17	7	17	17716.74	477	0	17	1	18	17179.77
129	0	2	8	2	17812.17	478	0	18	1	19	17178.34
130	0	3	8	3	17811.66	479	0	19	1	20	17176.79
131	0	4	8	4	17810.96	480	0	20	1	21	17175.18
132	0	5	8	5	17810.14	481	0	21	1	22	17173.43
133	0	6	8	6	17809.12	482	0	22	1	23	17171.60
134	0	7	8	7	17807.95	483	0	24	1	25	17167.60
135	0	8	8	8	17806.62	484	0	25	1	26	17165.47
136	0	9	8	9	17805.10	485	0	26	1	27	17163.23
137	0	10	8	10	17803.38	486	0	9	1	8	17181.81
138	0	1	9	1	17879.49	487	0	10	1	9	17180.36
139	0	2	9	2	17879.14	488	0	11	1	10	17178.85
140	0	3	9	3	17878.60	489	0	12	1	11	17177.29
141	0	4	9	4	17877.89	490	0	16	1	15	17170.18
142	0	5	9	5	17877.00	491	0	17	1	16	17168.18
143	0	6	9	6	17875.91	492	0	21	1	20	17159.19
144	0	7	9	7	17874.70	493	0	22	1	21	17156.69
145	1	1	0	1	16879.86	494	0	26	1	25	17145.75
146	1	2	0	2	16879.69	495	2	8	1	9	16805.09
147	1	3	0	3	16879.43	496	2	9	1	10	16804.46
148	1	4	0	4	16879.09	497	2	10	1	11	16803.84
149	1	5	0	5	16878.66	498	2	11	1	12	16803.11
150	1	6	0	6	16878.15	499	2	12	1	13	16802.32
151	1	7	0	7	16877.52	500	2	13	1	14	16801.44
152	1	8	0	8	16876.84	501	2	14	1	15	16800.48
153	1	9	0	9	16876.07	502	2	15	1	16	16799.41
154	1	10	0	10	16875.22	503	2	16	1	17	16798.28
155	1	1	2	1	17103.93	504	2	17	1	18	16797.04
156	1	2	2	2	17103.71	505	2	18	1	19	16795.71
157	1	3	2	3	17103.43	506	2	7	1	6	16800.93
158	1	4	2	4	17102.99	507	2	8	1	7	16799.66
159	1	5	2	5	17102.47	508	2	9	1	8	16798.37
160	1	6	2	6	17101.85	509	2	10	1	9	16797.01
161	1	7	2	7	17101.15	510	2	11	1	10	16795.57
162	1	8	2	8	17100.30	511	2	12	1	11	16794.08
163	1	9	2	9	17099.40	512	1	5	1	6	16997.12
164	1	10	2	10	17098.37	513	1	6	1	7	16996.72
165	1	11	2	11	17097.21	514	1	7	1	8	16996.22
166	1	12	2	12	17095.96	515	1	8	1	9	16995.68
167	1	13	2	13	17094.61	516	1	9	1	10	16995.08
168	1	14	2	14	17093.16	517	1	10	1	11	16994.40

169	1	15	2	15	17091.61	518	1	11	1	12	16993.65
170	1	16	2	16	17089.93	519	1	12	1	13	16992.82
171	1	17	2	17	17088.16	520	1	13	1	14	16991.89
172	1	18	2	18	17086.28	521	1	14	1	15	16990.88
173	1	19	2	19	17084.30	522	1	15	1	16	16989.77
174	1	20	2	20	17082.21	523	1	16	1	17	16988.57
175	2	2	1	2	16804.35	524	1	17	1	18	16987.27
176	2	3	1	3	16804.10	525	1	9	1	8	16988.98
177	2	4	1	4	16803.73	526	1	10	1	9	16987.53
178	2	5	1	5	16803.28	527	1	11	1	10	16986.09
179	2	6	1	6	16802.71	528	1	12	1	11	16984.56
180	2	7	1	7	16802.09	529	1	13	1	12	16982.95
181	2	8	1	8	16801.36	530	1	14	1	13	16981.24
182	2	9	1	9	16800.54	531	1	15	1	14	16979.51
183	2	10	1	10	16799.61	532	1	16	1	15	16977.64
184	2	11	1	11	16798.62	533	1	17	1	16	16975.68
185	2	12	1	12	16797.52	534	0	4	2	5	17297.54
186	2	13	1	13	16796.31	535	0	5	2	6	17297.33
187	2	14	1	14	16795.07	536	0	6	2	7	17297.03
188	2	1	2	1	16913.22	537	0	7	2	8	17296.58
189	2	2	2	2	16913.02	538	0	8	2	9	17296.04
190	2	4	2	4	16912.32	539	0	9	2	10	17295.41
191	2	5	2	5	16911.82	540	0	10	2	11	17294.61
192	2	6	2	6	16911.21	541	0	11	2	12	17293.68
193	2	7	2	7	16910.51	542	0	12	2	13	17292.63
194	2	8	2	8	16909.70	543	0	13	2	14	17291.44
195	2	10	2	10	16907.79	544	0	14	2	15	17290.09
196	2	11	2	11	16906.69	545	0	15	2	16	17288.30
197	2	12	2	12	16905.48	546	0	16	2	17	17288.54
198	2	13	2	13	16904.16	547	0	17	2	18	17286.92
199	2	14	2	14	16902.76	548	0	18	2	19	17285.25
200	2	15	2	15	16901.24	549	0	19	2	20	17283.49
201	2	18	2	18	16896.09	550	0	20	2	21	17281.60
202	2	19	2	19	16894.16	551	0	21	2	22	17279.63
203	2	20	2	20	16892.13	552	0	22	2	23	17277.57
204	2	2	8	2	17428.50	553	0	23	2	24	17275.39
205	2	3	8	3	17428.01	554	0	24	2	25	17273.13
206	2	4	8	4	17427.34	555	0	6	2	5	17292.81
207	2	5	8	5	17426.52	556	0	7	2	6	17291.73
208	2	6	8	6	17425.55	557	0	8	2	7	17290.54
209	2	7	8	7	17424.43	558	0	9	2	8	17289.25
210	2	12	8	12	17416.26	559	0	10	2	9	17287.85
211	2	13	8	13	17414.14	560	0	11	2	10	17286.34
212	2	14	8	14	17411.87	561	0	12	2	11	17284.68

213	2	17	8	17	17404.02	562	0	13	2	12	17282.92
214	2	18	8	18	17401.05	563	0	14	2	13	17281.04
215	2	20	8	20	17394.66	564	0	15	2	14	17278.95
216	2	21	8	21	17391.21	565	0	16	2	15	17276.68
217	2	23	8	23	17383.81	566	0	17	2	16	17274.11
218	2	24	8	24	17379.82	567	0	18	2	17	17273.45
219	2	2	9	2	17495.46	568	0	19	2	18	17271.01
220	2	3	9	3	17494.91	569	0	20	2	19	17268.47
221	2	4	9	4	17494.23	570	0	21	2	20	17265.85
222	2	5	9	5	17493.37	571	0	22	2	21	17263.14
223	2	6	9	6	17492.37	572	0	23	2	22	17260.32
224	2	7	9	7	17491.14	573	0	24	2	23	17257.42
225	2	8	9	8	17489.76	574	0	25	2	24	17254.38
226	2	9	9	9	17488.22	575	0	26	2	25	17251.25
227	2	12	9	12	17482.49	576	1	3	2	4	17104.69
228	2	13	9	13	17480.29	577	1	4	2	5	17104.60
229	2	14	9	14	17477.84	578	1	5	2	6	17104.43
230	2	17	9	17	17469.54	579	1	6	2	7	17104.13
231	2	20	9	20	17459.63	580	1	7	2	8	17103.69
232	2	2	10	2	17558.28	581	1	8	2	9	17103.17
233	2	3	10	3	17557.74	582	1	9	2	10	17102.55
234	2	4	10	4	17557.01	583	1	10	2	11	17101.79
235	2	5	10	5	17556.09	584	1	11	2	12	17100.95
236	2	6	10	6	17555.01	585	1	12	2	13	17099.92
237	2	7	10	7	17553.71	586	1	13	2	14	17098.75
238	2	8	10	8	17552.30	587	1	14	2	15	17097.47
239	2	9	10	9	17550.63	588	1	15	2	16	17095.68
240	2	10	10	10	17548.82	589	1	16	2	17	17095.95
241	2	11	10	11	17546.82	590	1	17	2	18	17094.40
242	2	12	10	12	17544.63	591	1	18	2	19	17092.80
243	2	14	10	14	17539.74	592	1	19	2	20	17091.08
244	2	15	10	15	17536.97	593	1	20	2	21	17089.29
245	2	18	10	18	17527.65	594	1	21	2	22	17087.38
246	2	19	10	19	17524.18	595	1	22	2	23	17085.38
247	2	21	10	21	17516.66	596	1	23	2	24	17083.28
248	2	1	11	1	17617.73	597	1	6	2	5	17099.89
249	2	2	11	2	17617.33	598	1	7	2	6	17098.84
250	2	3	11	3	17616.77	599	1	8	2	7	17097.70
251	2	4	11	4	17616.02	600	1	9	2	8	17096.41
252	2	5	11	5	17615.06	601	1	10	2	9	17095.05
253	2	6	11	6	17613.91	602	1	11	2	10	17093.57
254	2	7	11	7	17612.58	603	1	12	2	11	17091.96
255	2	8	11	8	17611.03	604	1	13	2	12	17090.24
256	2	9	11	9	17609.32	605	1	14	2	13	17088.38

257	2	11	11	11	17605.32	606	1	15	2	14	17086.34
258	2	12	11	12	17603.03	607	2	3	2	4	16914.00
259	2	13	11	13	17600.54	608	2	4	2	5	16913.93
260	2	14	11	14	17597.86	609	2	5	2	6	16913.74
261	2	16	11	16	17591.94	610	2	6	2	7	16913.46
262	2	17	11	17	17588.66	611	2	8	2	9	16912.57
263	2	19	11	19	17581.55	612	2	9	2	10	16911.97
264	2	22	11	22	17569.41	613	2	10	2	11	16911.25
265	2	24	11	24	17560.34	614	2	11	2	12	16910.40
266	2	2	12	2	17672.97	615	2	12	2	13	16909.44
267	2	3	12	3	17672.37	616	2	13	2	14	16908.30
268	2	4	12	4	17671.56	617	2	16	2	17	16905.65
269	2	5	12	5	17670.56	618	2	17	2	18	16904.16
270	2	6	12	6	17669.37	619	2	18	2	19	16902.59
271	2	7	12	7	17667.97	620	2	19	2	20	16900.94
272	2	8	12	8	17666.38	621	2	22	2	23	16895.44
273	2	9	12	9	17664.54	622	2	23	2	24	16893.40
274	2	12	12	12	17657.99	623	2	24	2	25	16891.26
275	2	13	12	13	17655.40	624	2	27	2	28	16884.23
276	2	16	12	16	17646.39	625	2	28	2	29	16881.66
277	2	17	12	17	17642.97	626	2	4	2	3	16911.01
278	2	20	12	20	17631.52	627	2	5	2	4	16910.18
279	2	22	12	22	17622.85	628	2	8	2	7	16907.08
280	2	1	13	1	17725.81	629	2	10	2	9	16904.49
281	2	2	13	2	17725.41	630	2	11	2	10	16903.04
282	2	3	13	3	17724.78	631	2	12	2	11	16901.47
283	2	4	13	4	17723.96	632	2	15	2	14	16895.99
284	2	5	13	5	17722.92	633	2	16	2	15	16893.80
285	2	6	13	6	17721.67	634	2	17	2	16	16891.35
286	2	7	13	7	17720.22	635	2	18	2	17	16890.82
287	2	9	13	9	17716.69	636	2	21	2	20	16883.58
288	2	10	13	10	17714.60	637	0	5	3	6	17398.96
289	2	11	13	11	17712.31	638	0	6	3	7	17398.57
290	2	12	13	12	17709.83	639	0	8	3	9	17397.39
291	2	13	13	13	17707.11	640	0	9	3	10	17396.69
292	2	16	13	16	17697.74	641	0	10	3	11	17395.84
293	2	19	13	19	17686.44	642	0	11	3	12	17394.87
294	2	21	13	21	17677.84	643	0	12	3	13	17393.79
295	2	23	13	23	17668.38	644	0	13	3	14	17392.58
296	2	1	14	1	17775.34	645	0	14	3	15	17391.24
297	2	2	14	2	17774.93	646	0	15	3	16	17389.79
298	2	3	14	3	17774.27	647	0	16	3	17	17388.24
299	2	4	14	4	17773.42	648	0	17	3	18	17386.56
300	2	5	14	5	17772.31	649	0	18	3	19	17384.73

301	2	9	14	9	17765.84	650	0	19	3	20	17382.79
302	2	10	14	10	17763.69	651	0	27	3	28	17362.47
303	2	11	14	11	17761.31	652	0	28	3	29	17359.06
304	2	14	14	14	17752.88	653	0	31	3	32	17350.69
305	2	17	14	17	17742.48	654	0	32	3	33	17347.08
306	2	18	14	18	17738.55	655	0	33	3	34	17343.38
307	2	20	14	20	17730.07	656	0	34	3	35	17339.53
308	2	21	14	21	17725.53	657	0	36	3	37	17331.53
309	2	24	14	24	17710.43	658	0	37	3	38	17327.33
310	2	1	15	1	17822.14	659	0	39	3	40	17318.54
311	2	2	15	2	17821.72	660	0	42	3	43	17304.27
312	2	3	15	3	17821.06	661	0	9	3	8	17390.70
313	2	4	15	4	17820.17	662	0	10	3	9	17389.22
314	2	5	15	5	17819.05	663	0	11	3	10	17387.65
315	2	9	15	9	17812.33	664	0	12	3	11	17385.92
316	2	10	15	10	17810.07	665	0	13	3	12	17384.08
317	2	11	15	11	17807.63	666	0	14	3	13	17382.15
318	2	13	15	13	17802.02	667	0	15	3	14	17380.08
319	2	14	15	14	17798.88	668	0	16	3	15	17377.89
320	2	17	15	17	17788.12	669	0	17	3	16	17375.59
321	2	22	15	22	17765.52	670	0	18	3	17	17373.18
322	2	1	16	1	17866.27	671	0	19	3	18	17370.61
323	2	2	16	2	17865.79	672	0	22	3	21	17362.26
324	2	3	16	3	17865.09	673	0	23	3	22	17359.21
325	2	4	16	4	17864.19	674	0	24	3	23	17356.05
326	2	5	16	5	17863.04	675	0	26	3	25	17349.36
327	2	9	16	9	17856.09	676	0	27	3	26	17345.78
328	2	10	16	10	17853.80	677	0	28	3	27	17342.05
329	2	13	16	13	17845.51	678	0	29	3	28	17338.05
330	2	14	16	14	17842.26	679	0	30	3	29	17333.82
331	2	17	16	17	17831.16	680	0	34	3	33	17318.51
332	2	1	17	1	17908.42	681	0	35	3	34	17313.95
333	2	2	17	2	17907.96	682	0	37	3	36	17304.48
334	2	3	17	3	17907.23	683	0	4	4	5	17494.02
335	2	4	17	4	17906.28	684	0	5	4	6	17493.68
336	2	5	17	5	17905.09	685	0	6	4	7	17493.22
337	2	9	17	9	17897.95	686	0	7	4	8	17492.64
338	2	10	17	10	17895.56	687	0	8	4	9	17491.92
339	2	13	17	13	17886.98	688	0	9	4	10	17491.08
340	2	14	17	14	17883.64	689	0	10	4	11	17490.13
341	2	16	17	16	17876.23	690	0	11	4	12	17489.03
342	2	5	18	5	17944.78	691	0	3	5	4	17582.48
343	2	6	18	6	17943.31	692	0	4	5	5	17582.23
344	2	7	18	7	17941.59	693	0	5	5	6	17581.86

345	2	8	18	8	17939.63		694	0	6	5	7	17581.32
346	2	9	18	9	17937.42		695	0	7	5	8	17580.64
347	2	10	18	10	17934.97		696	0	8	5	9	17579.82
348	2	11	18	11	17932.28		697	0	9	5	10	17578.89
349	2	13	18	13	17926.14		698	0	10	5	11	17577.81

Appendix B External cavity diode lasers

The material in this appendix is adapted from *Appl. Phys. B* 106, 629–633 (2012).

Mode-hop-free tuning over 135 GHz of external cavity diode lasers without anti-reflection coating

Sourav Dutta,¹ D. S. Elliott,^{1,2} and Yong P. Chen^{1,2}

¹*Department of Physics, Purdue University, West Lafayette, IN 47907, USA*

²*School of Electrical and Computer Engineering, Purdue University, West Lafayette, IN 47907, USA*

Abstract: We report an external cavity diode laser (ECDL), using a diode whose front facet is not anti-reflection (AR) coated, that has a mode-hop-free (MHF) tuning range greater than 135 GHz. We achieved this using a short external cavity and by simultaneously tuning the internal and external modes of the laser. We find that the precise location of the pivot point of the grating in our laser is less critical than commonly believed. The general applicability of the method, combined with the compact portable mechanical and electronic design, makes it well suited for both research and industrial applications.

1. Introduction

Single-mode, narrow band, continuous-wave (cw) lasers exhibiting wide and continuous wavelength tunability are of considerable interest for a variety of applications including high resolution spectroscopy [1], cooling and trapping [2], as well as sensing [3]. Semiconductor lasers are often used because their lasing wavelength can be easily tuned by changing either the injection current or the chip temperature. Distributed Bragg reflector (DBR) and distributed feedback (DFB) lasers provide large tuning range along with narrow linewidth and excellent power and frequency stability. However, DBR/DFB lasers are relatively expensive and available only at a few selected wavelengths. Fabry-Perot (FP) diode lasers, on the other hand, are cheap and available in a variety of wavelengths, but their tunability can be limited. The performance of a FP diode laser can be significantly improved by placing it within an external cavity employing a diffraction grating,

either in a Littrow [4,5] or a Littman [6] configuration. This arrangement substantially reduces the linewidth of the output beam, and allows coarse wavelength tuning; in the case of the Littrow configuration, through rotation of the grating.

Several groups have addressed the issue of increasing the mode-hop-free (MHF) tuning range of single-mode Littrow-type lasers. It has been proposed [7,8] that MHF tuning range can be enhanced by rotating the grating about an optimal pivot point, located precisely at the intersection of the grating plane and plane of the diode's rear facet (Fig. 1). Several works [9,10] discussed the sensitivity of the behavior of the laser on the precise location of this pivot point, while other works [11-13] focused on tuning the internal and external cavity lengths in the proper proportion. The maximum MHF tuning range reported for ECDLs without electronic feedback [14] or elaborate schemes involving acousto-optic modulators [15] is 110 GHz [10], achieved with AR coated diodes. For non-AR coated diodes, the maximum MHF tuning range reported is 90 GHz [11].

In this article, we report a simple, single-mode, narrow band, cw Littrow-type ECDL with a 137 GHz MHF tuning range using an “off the shelf” laser diode without AR coating. This, to the best of our knowledge, is the largest MHF tuning range among ECDLs using diodes with or without AR coating. Our observations lead us to conclude that the short external cavity length, in concert with careful scaling of the variations of the internal and external cavity lengths, are critical to achieving

large MHF tuning range, while the precise location of the pivot point of the grating is less important.

In the next section, we review the principle behind continuous MHF tuning. This is followed by the details of the mechanical design of our ECDL and the method we use to maximize the MHF tuning range. Measurements of the tuning range, including applications in spectroscopy, are then presented, followed by the conclusion.

2. Principle

The key factors that determine the frequency of the active mode of an ECDL have been discussed in a number of previous works; see for example [5,10,12]. In short, an ECDL tends to lase at the frequency with the greatest gain and lowest loss. The free running laser (FRL) has a broad gain profile (typical width ~ 10 nm). The internal cavity modes of the laser diode are typically spaced by around 100 GHz and the internal mode that experiences maximum gain determines the emission wavelength of the FRL. When the FRL is placed in an external cavity, the internal and external cavities are optically coupled. Frequencies of coupled cavities depend on the optical length of the two individual cavities and the reflectivity of the surfaces in a complex way [16]. In a simpler approximation, one can assume that the wavelength of the ECDL is determined by the external cavity mode positioned most closely to the center of the internal cavity mode.

For a Littrow-type ECDL, the wavelength λ that the grating feeds back to the diode chip is determined by the equation:

$$2a \sin \theta = \lambda \quad (1)$$

where θ is the angle of incidence (see Fig. 1) and a is the line spacing of the grating. The angular width $\Delta\theta_g$ of the beam diffracted from the grating can be shown to be $\Delta\theta_g = \lambda / (N a \cos \theta)$, where N is the number of grating lines illuminated by the laser beam [17]. Using representative parameters for our ECDL, where we have a grating with $a^{-1} = 1800$ lines/mm, a beam size of ~ 3 mm (thus N is about 5400), $\lambda = 780$ nm and $\theta \sim 44.6^\circ$, we find that $\Delta\theta_g$ is ~ 0.37 mrad. From Eq. (1), the grating rotation $\Delta\theta_{max}$ required for a scan of $\Delta\nu_{max}$ is found to be: $\Delta\theta_{max} = \Delta\nu_{max} \lambda^2 / (2ca \cos \theta)$, which for our 780 nm ECDL with $\Delta\nu_{max} \sim 140$ GHz yields $\Delta\theta_{max} \sim 0.36$ mrad. Since $\Delta\theta_{max}$ is comparable to $\Delta\theta_g$ (in fact $\Delta\theta_{max} / \Delta\theta_g \sim 1$ and is independent of θ), the precision of the rotation angle (and hence the pivot point of the grating) is not very critical for our range of tuning.

Another key factor that determines the frequency of the ECDL is the length L_e (~ 15 mm for our ECDLs) of the external cavity. The resonant external cavity mode is given by the equation:

$$m \lambda / 2 = L_e \quad (2)$$

where m is an integer. The transmission peaks of the external cavity are spaced by the cavity free spectral range (FSR) of ~ 10 GHz, much closer than those of the internal cavity.

To obtain a broad continuous MHF tuning range, the frequency supported by all the above factors must tune synchronously. As is commonly done [10-13], we tune the gain profile of the diode and the internal cavity mode frequency by varying the injection current I_{LD} . The amount by which the frequency changes with a change in the injection current is quantified through a parameter $\beta = \Delta\nu / \Delta I_{LD}$, and can easily be determined experimentally for a free running diode. The external mode frequency is tuned by varying the voltage applied to a piezoelectric transducer (PZT) that controls the grating position [10,13]. The variation of the external mode frequency is characterized by a parameter $\alpha = \Delta\nu / \Delta V_{PZT}$, which we determine experimentally, as described in the following section.

To summarize, the wavelength of the ECDL at a fixed temperature is determined by the injection current I_{LD} , the grating angle θ and the length L_e of the external cavity. To obtain MHF tuning, the shift ($\Delta\nu = \beta \Delta I_{LD}$) of the internal mode frequency caused by the change in I_{LD} must be equal to the frequency shift ($\Delta\nu = \alpha \Delta V_{PZT}$) caused by the change in cavity length L_e and, to a lesser degree, the grating angle θ .

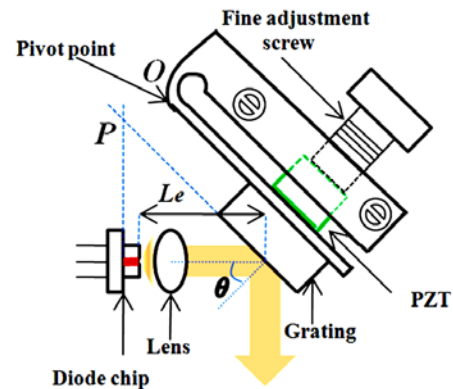


Fig. 1. Schematic of the mechanical setup of the ECDLs. The pivot point O of the grating is close to, but not precisely at, the optimal pivot point P . L_e is measured along the beam axis from the front facet of the diode chip to the grating.

3. Experimental design

We use commercial single-mode diode lasers without an AR coating in all our ECDLs. We have used many different diodes (Sanyo DL7140-201S, Hitachi HL7851G, Arima Lasers ADL-78901TL and Lasermate LD-808-100A) and all of them have scanned more than 120 GHz without mode hops. The lengths of the diode chips are less than 1 mm. The physical assembly of our design is similar to that described in Ref. 5 with some modifications. The beam is collimated with a lens (Thorlabs LT230P-B) and is directed onto a holographic diffraction grating with 1800 lines/mm (Thorlabs GH13-18V). The homemade grating mount has a lever arm that rotates about the pivot point O (Fig. 1). A piezoelectric actuator (Thorlabs AE0505D08F) is clamped between the lever arm and the fine-pitched adjustment screw that provides the horizontal adjustment by rotating the grating (in the plane of the figure). The vertical, out of the plane, adjustment is provided by another fine-pitched screw attached to the base (not shown in the figure). The whole base is temperature stabilized with a thermoelectric cooler. The injection current is supplied by a commercial laser diode driver (Thorlabs LDC 205C) and the temperature is controlled by a temperature controller (Thorlabs TED200C). The manufacturer and part numbers are mentioned only for the completeness of the description and not for endorsement.

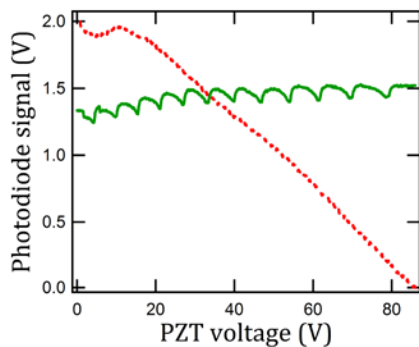


Fig. 2. Solid line (green): Power variation (measured with a photodiode) of an 808 nm ECDL on scanning the PZT with a linear ramp of 86V at a fixed value of injection current, resulting in multiple mode-hops. Dotted line (red): Power variation during a MHF scan of 121 GHz obtained with simultaneously varying the injection current and the PZT voltage.

In order to maximize the MHF tuning range of the ECDL, we must first determine $\beta = \Delta\nu / \Delta I_{LD}$ for our free-running diodes, and $\alpha = \Delta\nu / \Delta V_{PZT}$.

For the former, we vary the injection current I_{LD} in small steps and record the frequency ν on a wavelength-meter (Bristol Instruments 621A, resolution ~ 60 MHz). The measured values of β are within the range -1.4 GHz/mA to -2.4 GHz/mA for each of the different diodes we tested, and we estimate the measurement accuracy to be 0.1 GHz/mA. β varies as a function of I_{LD} . To determine α , we mount the diode in the external cavity, and measure the output power of the laser as a function of V_{PZT} . We show an example of this measurement in Fig. 2. Changing the external cavity length L_e by varying V_{PZT} , while holding the injection current fixed, tunes the external cavity mode frequency across the peak of the internal cavity mode. The output power is maximized when the external and internal mode frequencies are the same, but decreases as the mismatch increases. Mode hops occur when the shift in the external mode frequency exceeds half the FSR of the external cavity. At this point, the adjacent external mode has moved closer to the peak of the internal mode, and the laser oscillation hops to this new mode. In the green curve (solid line) of Fig. 2, these mode hops are seen at each of the minima, which are spaced by one free spectral range (FSR) of approximately 10 GHz. The corresponding change in V_{PZT} yields $\alpha \sim 1.5$ GHz/V near the center of this figure. The voltage spacing between peaks varies with V_{PZT} due to the nonlinear behavior of the PZT. The 12 mode hops recorded for the scan of 86 V, together with the 10 GHz FSR of the ECDL, suggests that a maximum scan range of $\Delta\nu_{max} \sim 120$ GHz ($= 12 \times \text{FSR}$) should be possible for this example. Indeed, concurrent scanning of I_{LD} and V_{PZT} yields the red curve (dotted line) in Fig. 2. The absence of peaks and valleys in this data is characteristic MHF tuning of the output frequency. This is confirmed by the smooth variation of the output frequency of the laser as measured with an optical wavelength meter. The nonlinear behavior of the output power when V_{PZT} is less than 15 V may be due to the variation of α and β over the long frequency scan and coupled cavity effects of the internal and external cavities. We have used this procedure to obtain MHF scan of over 120 GHz for all the diodes that we used, and up to 137 GHz for one of the diodes as discussed in the next section.

4. Experimental results

In this section, we present our results for one of our ECDLs with a 780 nm laser diode from Arima Lasers (ADL-78901TL). The design for this

ECDL is based on Fig. 1. The output beam is elliptical in shape, and remains collimated without noticeable divergence up to 2 meters. We use a Fabry-Perot interferometer of moderate finesse to place an upper bound on the laser linewidth of ~ 2 MHz. We determined the average value of β to be -1.7 GHz/mA (β varies between -1.4 GHz/mA and -1.9 GHz/mA as a function of I_{LD} .) α is determined to be 1.5 GHz/V, using a measurement similar to that shown in Fig. 2. The optimal scaling between the injection current and the PZT voltage is then estimated to be $\Delta I_{LD} / \Delta V_{PZT} = \alpha / \beta \approx -0.88$ mA/V. We optimize this value empirically by determining the MHF tuning range at a variety of different values, and find the optimal value to be $\Delta I_{LD} / \Delta V_{PZT} = -0.93$ mA/V. We show the frequency scan of the ECDL, measured using a wavelength meter, in Fig. 3 as the solid (red) curve. The dotted (green) curve shows the power variation of the ECDL. The longest frequency scan without mode hops was 137 GHz, accomplished with a 90 V ramp applied to the PZT and an injection current ramp from 124 mA to 40 mA. The experimentally optimized value of $\Delta I_{LD} / \Delta V_{PZT}$ is generally within 10% of the estimated value.

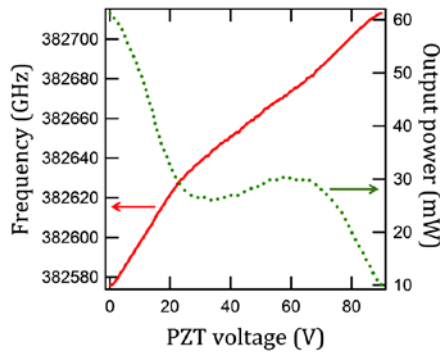


Fig. 3. Mode-hop-free scan of 137 GHz (from 382576 to 382713 GHz). The solid (red) curve shows the frequency (axis on the left) while the dotted (green) curve shows the output power (axis on the right), both plotted against the PZT voltage. The nonlinear dependence of the frequency and the output power on the PZT voltage may be due to the nonlinear dependence of the PZT displacement on V_{PZT} , coupled cavity effects of the internal and external cavities, and the variation of α and β over the long frequency scan.

In Fig. 4 we show the laser power transmitted through a Rubidium cell (containing both ^{85}Rb and ^{87}Rb) and through an Iodine cell (heated to 300°C) during another MHF scan of 135 GHz. The scan is obtained with $\Delta I_{LD} / \Delta V_{PZT} = -0.91$ mA/V. The four D_2 absorption lines of Rubidium, two from

^{85}Rb ($5s\ ^2S_{1/2}, F=3 \rightarrow 5p\ ^2P_{3/2}$ and $5s\ ^2S_{1/2}, F=2 \rightarrow 5p\ ^2P_{3/2}$) and two from ^{87}Rb ($5s\ ^2S_{1/2}, F=2 \rightarrow 5p\ ^2P_{3/2}$ and $5s\ ^2S_{1/2}, F=1 \rightarrow 5p\ ^2P_{3/2}$), are clearly visible. The numerous absorption features in the Iodine transmission spectrum arise from different rovibrational transitions of I_2 . We have verified that the frequencies of each of these Rb and I_2 absorption lines agree to within 1 GHz of the published line positions [18,19]. We also obtained a 129 GHz MHF tuning range around 781.6 nm (Fig. 5) using the same value of $\Delta I_{LD} / \Delta V_{PZT}$. The frequencies of these iodine absorption lines also match those found in Ref [19]. This is encouraging because it should be possible to patch together series of $100+$ GHz scans by manually rotating the grating without readjusting the current ramp. Figs. 4 and 5 demonstrate the great potential of these ECDLs in spectroscopy where long single-mode frequency scans are desirable.

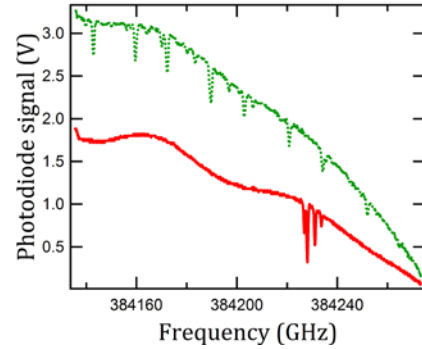


Fig. 4. Mode-hop-free scan of 135 GHz around 780.2 nm. Solid line (red): Laser transmission through a Rubidium vapor cell for a scan from 384137 to 384272 GHz. Dotted line (green): Transmission through an Iodine cell (heated to 300°C).

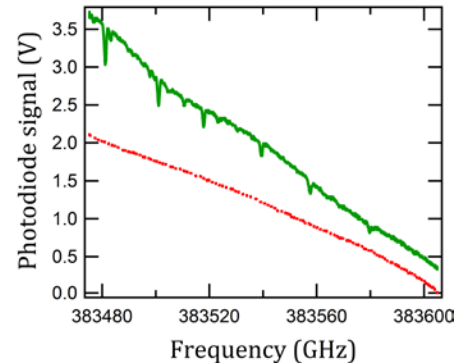


Fig. 5. Mode-hop-free scan of 129 GHz over a different frequency range (around 781.6 nm), with the same value of $\Delta I_{LD} / \Delta V_{PZT}$ as used for Fig. 4. Solid line (green): Laser transmission through an Iodine cell (heated to 300°C). Dotted line (red): Transmission through a Rubidium vapor cell.

Finally, to understand which factors are more important than others for MHF tuning, we made another ECDL for which the pivot point is closer to the optimum location but observed no improvement in the tuning range. We then increased the external cavity length to $L_e = 18$ mm. This change also implies that the pivot point was farther from the optimal position. Although the tuning range decreased, we were able to achieve over 100 GHz of MHF tuning. We attribute the decrease in MHF tuning to the increase in the length L_e of the external cavity, and the corresponding decrease in FSR. As discussed in the previous section, the relatively wide spectral width (due to finite angular width $\Delta\theta_g$) of the grating feedback makes the position of the pivot point less critical. The finite spectral width of the grating feedback was not considered in the analysis in Refs. 7-9, which predict that sub-millimeter accuracy is required for 100 GHz MHF scan.

5. Conclusion and outlook

In conclusion, we have demonstrated a simple method to obtain large MHF tuning of a laser diode without AR-coating. We were able to achieve 137 GHz mode-hop-free tuning around 783.5 nm. This, to the best of our knowledge, is the widest MHF tuning of a simple cavity diode with or without an AR-coating. We found that, during the scan, it is extremely important that the frequency of the internal mode (tuned by the injection current) scans synchronously with the mode of the external cavity (tuned by a PZT that controls the external cavity length). It is easier to satisfy this condition for a shorter external cavity because a large FSR reduces the possibility of competing external cavity modes. The smallest external cavity we tried is around 15 mm; a smaller cavity is expected to result in an even higher MHF tuning. However, the tuning range may be limited by the injection current: we had to tune the current almost across the entire accessible range to obtain the 137 GHz scan. The tuning range is expected to increase for AR-coated diodes (where the internal cavity tends to be less important [20]). In addition a PZT with higher displacement is expected to increase the tuning range.

21.

Acknowledgments

This work is partially supported by the National Science Foundation (grant number CCF0829918). SD acknowledges Adeel Altaf and Dionysios Antypas for helpful discussions.

References

1. C. E. Wieman, L. Hollberg, *Rev. Sci. Instrum.* **62**, 1 (1991)
2. E. A. Cornell, C. E. Wieman, *Rev. Mod. Phys.* **74**, 875 (2002)
3. J. Shao, L. Lathdavong, P. Thavixay, O. Axner, *J. Opt. Soc. Am. B* **24**, 2294 (2007)
4. M. W. Fleming, A. Mooradian, *IEEE J. Quantum Electron.* **QE-17**, 44 (1981)
5. L. Ricci, M. Weidemüller, T. Esslinger, A. Hemmerich, C. Zimmermann, V. Vuletic, W. König, T. W. Hänsch, *Opt. Commun.* **117**, 541 (1995)
6. K. Liu, M. G. Littman, *Opt. Lett.* **6**, 117 (1980)
7. M. de Labachellerie, G. Passedat, *Appl. Opt.* **32**, 269 (1993); Erratum: M. de Labachellerie, H. Sasada, G. Passedat, *Appl. Opt.* **33**, 3817 (1994)
8. L. Nilse, H. J. Davies, C. S. Adams, *Appl. Opt.* **38**, 548 (1999)
9. T. Hof, D. Fick, H. J. Jänsch, *Opt. Commun.* **124**, 283 (1996)
10. J. Hult, I. S. Burns, C. F. Kaminski, *Appl. Opt.* **44**, 3675 (2005)
11. V. P. Gerginov, Y. V. Dancheva, M. A. Taslakov, S. S. Cartaleva, *Opt. Commun.* **149**, 162 (1998)
12. T. Führer, T. Walther, *Opt. Lett.* **33**, 372 (2008)
13. C. Petridis, I. D. Lindsay, D. J. M. Stothard, M. Ebrahimzadeh, *Rev. Sci. Instrum.*, **72**, 3811 (2001)
14. T. Führer, D. Stang, T. Walther, *Opt. Express* **17**, 4991 (2009)
15. A. Bösel, K-D. Salewski, T. Kinder, *Opt. Lett.* **32**, 1956 (2007)
16. R. J. Lang, A. Yariv, *Phys. Rev. A* **34**, 2038 (1986)
17. R. S. Longhurst: *Geometrical and Physical Optics* (Longman, UK, 1973), pp. 261–305
18. Daniel Steck: Alkali D Line Data (<http://steck.us/alkalidata/>)
19. S. Gerstenkorn, J. Verges, J. Chevillard: Atlas du Spectre d'Absorption de la Molecule d'Iode, Laboratoire Aimé Cotton (<http://www.lac.u-psud.fr/Iode-11-000-14-000-cm-1>)
20. L. Hildebrandt, R. Knispel, S. Stry, J. R. Sacher, F. Schael, *Appl. Opt.* **42**, 2110 (2003)

VITA

VITA

Sourav Dutta was born in West Bengal, India. He attended the Presidency College, Kolkata for his Bachelor of Science degree and received the same from the University of Calcutta in 2005. He then joined the S. N. Bose National Centre for Basic Sciences and received his Masters of Science degree from the West Bengal University of Technology in 2007. In Fall 2007, he joined Purdue University as a graduate student. His research interests include laser cooling and trapping of atoms, ultracold molecule formation and high resolution laser spectroscopy.